Dynamic Security Region Assessment

Oluic, Marina

DOI
10.4233/uuid:0bca20cc-98b8-49a0-b9af-94656f73ebd5

Publication date
2019

Document Version
Final published version

Citation (APA)
Oluic, M. (2019). *Dynamic Security Region Assessment*. [Dissertation (TU Delft), Delft University of Technology, KTH Royal Institute of Technology, Comillas Pontifical University].
https://doi.org/10.4233/uuid:0bca20cc-98b8-49a0-b9af-94656f73ebd5

DOCTORAL THESIS

STOCKHOLM, SWEDEN 2019

Dynamic Security Region Assessment

Marina Oluić

Dynamic Security Region Assessment

Marina Oluić

Thesis supervisors:

Prof. Mehrdad Ghandhari	KTH Royal Institute of Technology
Dr. Bertil Berggren	ABB Corporate Research

Members of the Examination Committee:

Prof. Lina Bertling Tjernberg	KTH Royal Institute of Technology, Sweden
Assoc. Prof. Enrique Lobato Miguélez	Comillas Pontifical University, Spain
Assoc. Prof. Marjan Popov	Delft University of Technology, the Netherlands
Prof. Olof Samuelsson	Lund University, Sweden
Dr. Katherine Elkington	Svenska Kraftnät (Swedish National Grid), Sweden

TRITA-EECS-AVL-2019:31

ISBN 978-91-7873-149-7

Printed by: US-AB

Dynamic Security Region Assessment

Dissertation

for the purpose of obtaining the degree of doctor
at Delft University of Technology
by the authority of the Rector Magnificus prof.dr.ir. T.H.J.J. van der Hagen
Chair of the Board for Doctorates
to be defended publicly on
Wednesday 12 June 2019 at 10:00 o'clock

by

Marina OLUIĆ

Electrical Power Engineer

M.Sc. in Electrical and Computer Engineering
Faculty of Technical Sciences (FTN), Serbia
born in Ruma, Serbia

This dissertation has been approved by the promotors.

Composition of the doctoral committee:

Chairman	KTH Royal Institute of Technology, Sweden
Prof. dr. M. Ghandhari	KTH Royal Institute of Technology, Sweden, promotor
Prof. dr. ir. P. M. Herder	Delft University of Technology, the Netherlands, promotor

Independent members:

Prof. Lina Bertling Tjernberg	KTH Royal Institute of Technology, Sweden
Assoc. Prof. Enrique Lobato Miguélez	Comillas Pontifical University, Spain
Assoc. Prof. Marjan Popov	Delft University of Technology, the Netherlands
Prof. Olof Samuelsson	Lund University, Sweden
Dr. Katherine Elkington	Svenska Kraftnät (Swedish National Grid), Sweden

The doctoral research has been carried out in the context of an agreement on joint doctoral supervision between Comillas Pontifical University, Madrid, Spain, KTH Royal Institute of Technology, Stockholm, Sweden and Delft University of Technology, the Netherlands.

Keywords: parametrization, power system transient stability, security boundary, short-term voltage instability, Voltage Impasse Region (VIR)

ISBN: 978-91-7873-149-7

Printed by: US-AB

SETS Joint Doctorate

The Erasmus Mundus Joint Doctorate in ***Sustainable Energy Technologies and Strategies***, SETS Joint Doctorate, is an international programme run by six institutions in cooperation:

- Comillas Pontifical University, Madrid, Spain
- Delft University of Technology, Delft, the Netherlands
- KTH Royal Institute of Technology, Stockholm, Sweden
- Florence School of Regulation, Florence, Italy
- Johns Hopkins University, Baltimore, USA
- University Paris-Sud 11, Paris, France

The Doctoral Degrees issued upon completion of the programme are issued by Comillas Pontifical University, Delft University of Technology, and KTH Royal Institute of Technology.

The Degree Certificates are giving reference to the joint programme. The doctoral candidates are jointly supervised, and must pass a joint examination procedure set up by the three institutions issuing the degrees.

This thesis is a part of the examination for the doctoral degree. The invested degrees are official in Spain, the Netherlands and Sweden respectively.

SETS Joint Doctorate was awarded the Erasmus Mundus **excellence label** by the European Commission in year 2010, and the European Commission's **Education, Audiovisual and Culture Executive Agency**, EACEA, has supported the funding of this programme.

The EACEA is not to be held responsible for contents of the thesis.

Abstract in English Language

Author: Marina Oluić
Division of Electric Power and Energy Systems (EPE)
Affiliation: KTH Royal Institute of Technology
Title: Dynamic Security Region Assessment
Language: English
Keywords: parametrization, power system transient stability, security boundary, short-term voltage instability, Voltage Impasse Region (VIR)

Among a wide variety of topics that are covered by Dynamic Security Assessment (DSA), maintaining synchronous operation and acceptable voltage profiles stand out. These two stability categories are mostly jeopardized in the seconds after a large contingency occurs. Therefore, this thesis tackles the two aspects of large disturbance stability of power systems in the short-term time scale.

The classical DSA methods deal with the short-term loss of synchronism by analyzing one operating point and one contingency at a time. However, a small change in operating point may turn a stable system unstable. The first part of the thesis overcomes this gap by proposing the idea of parametrizing the stability boundary. The newly introduced method constructs the parametrized security boundaries in polynomial forms based on a reduced amount of Time Domain Simulation (TDS) data. Such a method retains the positive traits of TDS while being able to estimate a measure of stability even for those points that do not belong to the "training" set. The polynomial coefficients are further improved via SIME parametrization that has a physical meaning. Finally, when being subject to a constraint by the means of Quadratic Programming (QP), SIME parametrization also becomes competitive with direct methods in the sense of conservativeness.

Nevertheless, if TDS fails, any TDS-based DSA approach is useless. Most often, the dynamics of the non-linear power system is described by the set of Differential Algebraic Equations (DAE). TDS can face problems when the DAE model experiences singularity due to the loss of voltage causality. This thesis introduces Voltage Impasse Region (VIR) as the state-space area where the voltage causality is lost due to the non-linear modeling of static loads. The entrance of a dynamic trajectory to a VIR was shown to be accompanied by non-convergence issues in TDS and significant voltage drops. Appropriate Voltage Collapse Indicators (VCIs) are also derived for each load model of interest. The thesis concluded that VIR is a structural problem of the DAE model that should always be accounted for when the short-term stability is assessed.

Sammanfattning (Summary in Swedish)

Författare: Marina Oluić
Affiliering: Kungliga Tekniska Högskolan
Titel: Uppskattning av Dynamisk Säkerhetsregion
Språk: Engelska
Nyckelord: parametrisering, spänningsimpassregion (VIR), spänningsinstabilitet, säkerhetsgräns, transient stabilitet i kraftsystem

Bland många olika ämnen som omfattas av dynamisk säkerhetsbedömning (DSA) utmärker sig säkerställandet av synkron drift och acceptabla spänningsprofiler. Dessa två stabilitetskategorier äventyras typiskt i storleksordningen sekunder efter en stor händelse. Därför behandlar den här avhandlingen dessa två aspekter av korttidsstabilitet vid stora störningar i kraftsystemet.

De klassiska DSA-metoderna hanterar transient stabilitetsanalys genom att analysera en driftspunkt och en störning åt gången. Ändras driftpunkten något kan emellertid slutsatsen om stabilitet ändras. Den första delen av avhandlingen överkommer detta genom att introducera iden om att parametrisera stabilitetsgränsen. Den nyligen introducerade metoden konstruerar de parametriserade säkerhetsgränserna i form av polynom baserat på en reducerad mängd data från tidsdomänsimuleringar (TDS). Sådana metoder behåller de positiva egenskaperna hos TDS samtidigt som man kan uppskatta ett stabilitetsmått även för de punkter som inte hör till “tränings" -setet. Polynomkoefficienterna förbättras ytterligare via SIME parametrisering som har en fysisk betydelse. Slutligen, när SIME-parametriseringen utsätts för en kvadratisk optimering (QP) med begränsningar, så blir resultatet också konkurrenskraftigt med direkta metoder i bemärkelsen att resultatet är konservativt.

Ändå, om TDS misslyckas, så är det TDS-baserade DSA-tillvägagångssättet värdelöst. Oftast beskrivs dynamiken hos det icke-linjära kraftsystemet av en uppsättning av differentialalgebraiska ekvationer (DAE). TDS får problem när DAE-modellen blir singulär på grund av förlusten av spännings-orsakssamband. Denna avhandling introducerar spänningsimpassregionen (VIR) som tillståndsområdet där spännings-orsakssamband försvinner på grund av den icke-linjära modelleringen av statiska belastningarna. En trajektoria som träffar en VIR visades vara åtföljd av icke-konvergensproblem i TDS och signifikanta spänningsfall. Lämpliga spänningskollapsindikatorerna (VCIs) har också härletts för varje belastningsmodell av intresse. Avhandlingen konstaterade att VIR är ett strukturellt problem som följer av DAE-modellen som alltid bör redovisas när den transienta stabiliteten bedöms.

Abstract/summary in Dutch language

Auteur: Marina Oluić
Institutt: KTH Royal Institute of Technology
Titel: Beoordeling van Dynamische Veiligheidsregio's
Taal: Engels
Trefwoorden: kortstondige spanningsinstabiliteit, parametrisering, spanningsimpasse-regio (VIR), tijdelijke stabiliteit van het energiesysteem, veiligheidsgrens

Onder een breed scala aan onderwerpen die worden gedekt door dynamische veiligheidsbeoordeling (DSA), het onderhouden van synchrone werking en acceptabele spanningsprofielen. Deze twee stabiliteitscategorieën worden meestal in gevaar gebracht in de seconden nadat een grote contingentie heeft plaatsgevonden. Daarom behandelt dit proefschrift de twee aspecten van grote storingsstabiliteit van energiesystemen op korte termijn.

De klassieke DSA-methoden behandelen het kortstondige verlies van synchronisme bij het analyseren van één werkpunt en één contingentie tegelijk. Een kleine wijziging in het werkpunt kan echter een stabiel systeem onstabiel maken. Het eerste deel van het proefschrift overwint deze kloof door het idee voor te stellen om de stabiliteitsgrens te parametriseren. De nieuw geïntroduceerde methode construeert de geparametriseerde beveiligingsgrenzen in polynomiale vormen gebaseerd op een tijdshoeveelheid tijddomeinsimulatie (TDS) gegevens. Zo'n methode behoudt de positieve eigenschappen van TDS, terwijl het in staat is om een mate van stabiliteit te schatten, zelfs voor die punten die niet tot de "trainingsset" behoren. De polynoomcoëfficiënten worden verder verbeterd via SIME-parametrisering die een fysieke betekenis heeft. Ten slotte wordt SIME-parametrisering, wanneer ze wordt onderworpen aan de middelen van kwadratische programmering (QP), ook concurrerend met directe methoden in de zin van conservativiteit.

Niettemin, als TDS faalt, is elke op TDS gebaseerde DSA-benadering nutteloos. Meestal wordt de dynamiek van het niet-lineaire machtssysteem beschreven door de set differentiaalalgebraïsche vergelijkingen (DAE). TDS kan problemen ondervinden wanneer het DAE-model singulariteit ervaart vanwege het verlies van spanningsoorsprong. Dit proefschrift introduceert een spanningsimpasse-regio (VIR) als het toestandsruimtegebied waar de spanningsveroorzaker verloren gaat door de niet-lineaire modellering van statische belastingen. De ingang van een dynamisch traject naar een VIR bleek vergezeld te gaan van niet-convergentieproblemen in TDS en significante spanningsdalingen. Passende spanningsuitstootindicatoren (VCIs) worden ook afgeleid voor elk belastingsmodel dat van belang is. Het proefschrift

concludeerde dat VIR een structureel probleem is van het DAE-model dat altijd moet worden verantwoord wanneer de kortetermijnstabiliteit wordt beoordeeld.

Acknowledgment

This project was carried out within the Erasmus Mundus Joint Doctorate in Sustainable Energy Technologies and Strategies (SETS Joint Doctorate) and was funded mainly by the European Commission Erasmus Mundus Doctoral Fellowship and partially by KTH Royal Institute of Technology. I would like to express my gratitude towards all partner institutions within the program as well as the European Commission for their support.

Foremost, I would like to thank to my supervisor, prof. Mehrdad Ghandhari, for his guidance, knowledge, support and motivation throughout the project and also for his patience in all those moments when not everything went as planned (equally important). Moreover, my sincere gratitude goes to my co-supervisor, dr. Bertil Berggren, for his continuous and prompt feedback, innovative ideas, persistent corrections of (the?) articles and interesting discussions. Thank you both for making this thesis possible.

Special thanks also go to my supervisor at Instituto de Investigacion Tecnológica (IIT), prof. Luis Rouco, who hosted me in his Modeling, Analysis and Control (MAC) research unit during my research stay at Comillas in Madrid. I would in particular like to acknowledge the research efforts of dr. Francisco Echavarren (aka Paco) for his insightful contribution to the development of Voltage Impasse Regions idea during my “Comillas mobility".

Every PhD project needs an adequate support system. Thus, a round of applause goes to these people: Sara Tamarit, SETS program coordinator at Comillas, for her kindness and capability to tackle the challenges of this international project; to our hard-working administrators/coordinators Eleni, Brigitt and Annica; and to the Electric Power and Energy Systems (EPE) division “captain", prof. Lars Nordström, for providing a friendly work environment as a part of the division vision.

I am using this opportunity to mention my Master & Bachelor theses supervisor, prof. Andrija Sarić, who encouraged me to pursue a PhD and to additionally thank him for organizing two invited lectures for me in Novi Sad. Many thanks go to dr.

Vedran Perić, for his reliability, useful advice and also for bringing me HB beer from Munich. You are a true friend.

Now, five lines and three quarters to a very special group of people from extended PSOC research group (in the order of appearance)—my SETS “twinnie" Omar, Dimitraki mu, Taha Roomie, wise Fabi, Steeefan “the professor", my favorite Croat Tin, the great expert Danilo (Данило) and the lady who recently landed at KTH after falling out of the sky (Angel). Thank you all for many unnecessary fikas that were so necessary. You made me laugh to tears—I will miss you.

As one of the veterans of the corridor, I had a pleasure to enjoy EPE’s multi-cultural atmosphere while meeting a collection of amazing people from whom I learned so much. Many of them are already remarkable doctors while others are likely to become. My sincere appreciation for the time spent with all of you present and former EPE members, guest researchers, SETS students and colleagues from IIT can be nicely condensed into the single quote by dr. Francisco J. Gómez López: *“While I am writing these letters, lots of names are coming and leaving so I prefer to mention no one, because I wouldn’t like to forget any of them."* Working at EPE was such a fortune, however, my computer is too ancient to upgrade to Windows 10.

There are people whose presence indirectly made a difference during my PhD years. The first two of them are excellent engineers and friends, Sonja and Maja, thanks to who I have realized that as opposed to power flow, the mismatch between spiritual and spatial distances does not necessarily have to converge to maintain an equilibrium. Thank you also dear Tetiana and Yelena for being there for me. I owe a lot to family Latinović for their willingness to help us out along the road (sometimes literally). Not to forget Jezda who does not completely belong to any of the previous groups so I mention him here.

Finally, I express my deepest gratitude to the ones closest to me. I thank from the bottom of my heart to the life-long wind at my back—my parents, Snežana and Predrag, and my sister, Marija, for their unconditional love, wonderful childhood and for teaching me how to dream. Last but not least, my heartfelt love goes to the two ultimate sources of my strength and inspiration: to my incredible husband Nemanja, who does not have to be acknowledged to understand that this thesis would have never been written without him; and to our fabulous children, Miona and Mihailo, without whose endless energy this thesis could have been maybe written in 2017, but then I would not get the chance to reconsider the existence of “perpetuum mobile". You empowered a new me and I had so much fun. Thank You.

"The scientific man does not aim at an immediate result. He does not expect that his advanced ideas will be readily taken up. His work is like that of a planter—for the future. His duty is to lay the foundation for those who are to come, and point the way."

—Nikola Tesla, July 1934

"Благо оном ко зна да не зна, а хоће да зна."

—српска народна пословица

To my dear parents,
who taught me that "a pencil and a notebook" create possibilities.
To my beloved Nemanja,
whose patience and humor make the possibilities real.
To our lovely children,
whose laughter and curiosity persuaded me that impossible is ok, too.

Мојим драгим родитељима,
који су ми указали да су "свеска и оловка" врло моћан алат за померање стена.
Мом духовитом Немањи,
који за такве стеновите подухвате ипак бира бушилицу.
Нашој раздраганој деци,
која се уз стену најрадије попну...и спусте...и опет попну...
Волим Вас до неба.

Contents

List of Acronyms

AC	Alternating Current
ANN	Artificial Neural Networks
CCT	Critical Clearing Time(s)
CLS	Constrained Least Squares
CUEPApp	Closest Unstable Equilibrium Point Approximation
DAE	Differential Algebraic Equations
DSA	Dynamic Security Assessment
EAC	Equal Area Criterion
HVDC	High Voltage Direct Current
LTC(s)	Load Tap Changer(s)
ODE	Ordinary Differential Equations
OEL(s)	OverExcitation Limiter(s)
OLS	Ordinary Least Squares
OP	Operating Point
PEBS	Potential Energy Boundary Surface
PMUs	Phasor Measurement Units
PRM	Pattern Recognition Methods
QP	Quadratic Programming
RAS	Rotor Angle Stability
REMV	Relative Error Mean Value
RK	Runge-Kutta
RNM	Reduced Network Model
SCADA	Supervisory Control And Data Acquisition
SD	Standard Deviation
SEP	Stable Equilibrium Point
SIME	SIngle Machine Equivalent
SMIB	Single Machine Infinite Bus
SNB	Saddle-Node Bifurcation

SPM	Structure Preserving Model
SSA	Static Security Assessment
SSR	Sum of Squared Residuals
SSSA	Small Signal Stability Analysis
TDS	Time Domain Simulation
TEF	Transient Energy Function
TS	Trajectory Sensitivities
TSO(s)	Transmission System Operator(s)
UEP(s)	Unstable Equilibrium Point(s)
VCI_{CP}	Voltage Collapse Indicator for the Constant Power load
VCIs	Voltage Collapse Indicators
$VCIs_{CC}$	Voltage Collapse Indicators for the Constant Current load
VIR	Voltage Impasse Region(s)
ZIP	The load model composed of constant impedance (Z), constant current (I) and constant power (P) components

List of Figures

List of Tables

Chapter 1

Introduction

1.1 Background

The progress of the civilization during the previous 140 years has been heavily associated with the electrification and power availability [1–4]. A reliable power system is not only a basin for the continuous technological development, but rather a pre-requisite for the quality of everyday life that the humanity is accustomed to. Hence, to operate a power system in a secure manner is a high priority task. The responsibility of the engineering community is therefore great — the society should not suffer from the side-effects of occurrences in the power system. Additionally, a continuously evolving power system poses a major challenge to power engineers and researchers. Growth in power consumption, new components/apparatus and cost-effective operation are strongly coupled with dynamic stability that needs to be frequently reassessed. This thesis will attempt to add value to the broad field of dynamic security assessment by making a modest advance towards the fundamental understanding of some important dynamical phenomena that occur in power systems.

Power system security and supply reliability are primary tasks for Transmission System Operators (TSOs). The major challenge of security analysis is the nature of the power system itself — its inability to store large amounts of electrical power requires a set of actions that maintain uninterrupted and reliable supply. The scenario of cascading outages followed by uncontrollable islanding and voltage collapse that result in catastrophic blackouts [5] is unacceptable in modern "electrified" society. The reasons for these incidents vary from typical large disturbances such as generator outage [6], loss of transmission lines [7] and overloading [8] to the

ones that are not expected to induce such disastrous outcomes (for instance, a faulty relay [9]). Some external unfortunate plots of events were even more improbable to predict — storms [10], lightnings [11], celestial events (the sun's coronal mass ejection) [12] or even a cruise ship passing [13] are on the list. Regardless of the reason, the aftermath of blackouts is similar. The extent of havoc in which large portions of countries have been left in darkness was reaching up to 32 GW of power generation shortage [14] and 620 million customers affected [15, 16].

On the other hand, power systems are subject to interminable upgrade in order to be able to cope with the surge in population and consequently, consumption. The most important evolutionary milestones in power systems have involved: interconnections [17], open electricity markets [18], growth in share of renewable energy sources [19] and development of power electronic based controllable technologies in transmission [20]. The TSOs need to take all of these factors into consideration when carrying out security assessment. The security margin of operation modes have also vastly decreased as the regulation power of TSO weakened due to higher percentage of variable energy sources [21]. To achieve high security and mitigate the aforementioned hazardous situations, TSOs design various remedial actions that are compliant with deterministic or probabilistic security criteria. One of the most well-known deterministic approaches, (N-1) criterion [22], requires that the power system security is always guaranteed after an unplanned loss of an important component. Although the (N-1) rule and other deterministic criteria served well in the past, they presume the same likelihood of occurrence for all contingencies. The second, probabilistic security approach [23], is more realistic since it accounts for the risk of security-limiting events. However, there is a trade-off — the risk-based criterion comes with large computational time.

No matter which of the security principles is enforced, the TSOs have to make sure that a power system accommodates to a new operational state without security violations. This decision practically involves two types of security analyses [24]:

- **Static security assessment (SSA)** which considers the capability of the power system to operate in a stable state with respect to the security constrains after a contingency. SSA primarily investigates bus voltages and transmission line flow violations [25].

- **Dynamic security assessment (DSA)** which works with the dynamic response of a power system to disturbances. The aim of DSA is to determine if the system will manage to handle a contingency by recovering to a secure state. When analyzing the dynamics associated to a contingency, DSA needs

to check different aspects of power system transient behaviour, e.g. Rotor Angle Stability (RAS), transient voltages and frequency stability [26].

Fig. 1.1 demonstrates how SSA and DSA cooperate while analyzing the consequences of a probable disturbance. SSA checks the afore mentioned security limitations for the expected set of pre- and post-disturbance operating conditions. DSA further investigates if the secure transition between the states is possible with respect to the list of critical contingencies. The output of this combined analysis shapes TSO actions during various regimes in system operation.

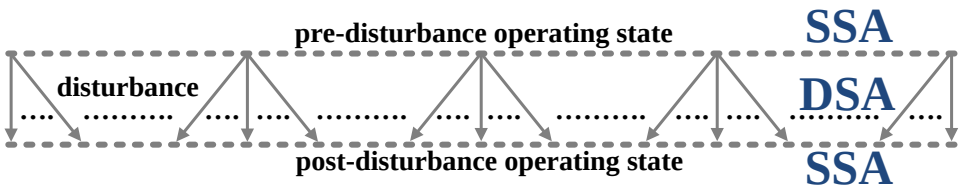

Figure 1.1: The distribution of tasks between SSA and DSA

The accepted standard is that power system operation may be decomposed into four regimes with corresponding remedial actions (controls): (i) *normal*, (ii) *alert*, (iii) *emergency* and (iv) *restorative* state [27–29]. Normal state [30] refers to the desirable state where a power system operates within its security constraints. Another operating state, alert regime [31], appears when security margin is dangerously small (for instance, after a disturbance). The alert state is considered insecure since a likely contingency could lead to a violation of some security constraint and induce so-called emergency state. The alert state involves preventive actions that tend to dislocate the operating state (o.s.) into a normal regime. The incidence of the two remaining operating regimes is highly undesirable. An emergency state [32] denotes a critical regime in power system operation which usually occurs after some significant contingency. In these cases power system may exhibit loss of synchronism, excessive voltage drops, violation of thermal security limits for system components or significant decrease in frequency. Emergency controls aim to rapidly stop further degradation in power system operation such that a new stable state may be attained. A possible aftermath of an emergency state is a quasi-stationary state known as restorative regime [33]. The restorative regime denotes a phase in system operation where a service to some customers is lost. Consequently, the restorative controls gradually shift the operating condition from partial to complete load supply. Some authors also consider *"in extremis"* operation as a separate, disintegrated regime that

links the emergency and restorative states [29]. Fig. 1.2 shows the afore mentioned regimes, their corresponding controls and relationships that exist among them.

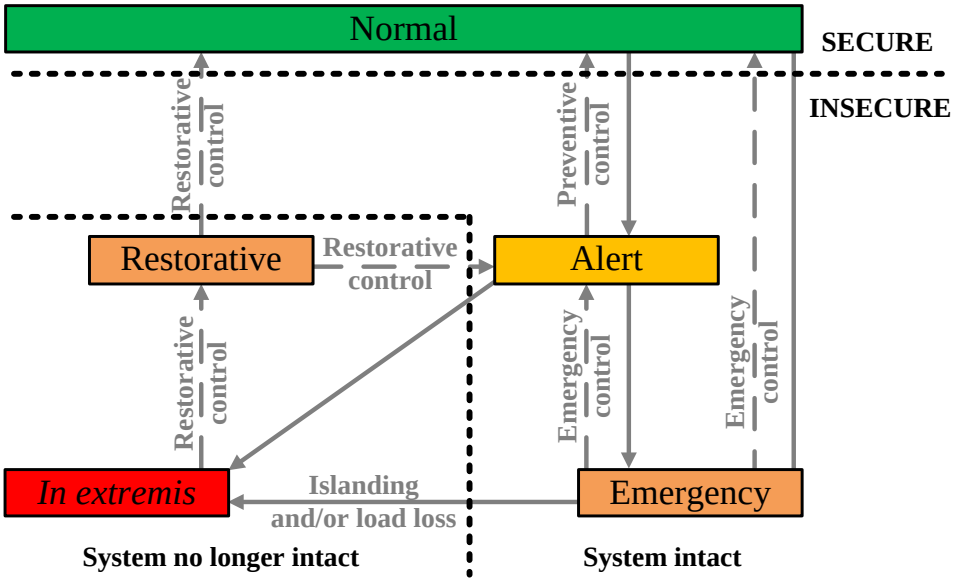

Figure 1.2: The states in power system operation

SSA and DSA jointly strive towards having an alert state as the worst case outcome of a probable disturbance. A time line of such a disturbance [34, 35] is depicted in Fig. 1.3 from the viewpoint of the two (normal and alert) regimes. Once the system is in the alert regime, TSO typically has 15-30 minutes [36] to assess the situation and perform preventive actions in order to regain a normal operating state.

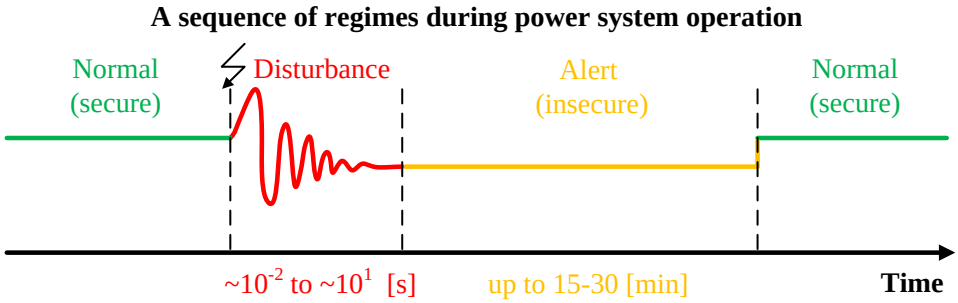

Figure 1.3: Timeline of a disturbance in the framework of security assessment

The worst outcome of a disturbance is an emergency operation that progresses to a complete blackout, as illustrated in Fig. 1.4. When a fault has already occurred it is usually too late to design new TSOs remedial actions/automatic controls (they are mostly of fast-operating, emergency type with predefined settings). DSA has to be carried out in advance in order to minimize consequences once a contingency starts posing serious stability risks that could lead to power system failure. This is the point where appropriate DSA can make a difference between a usual day for people and a day under a blackout. Hence, faster and more efficient DSA methods are always needed — this is a timely issue, and the number of the strategies introduced so far corresponds to DSA relevance [37].

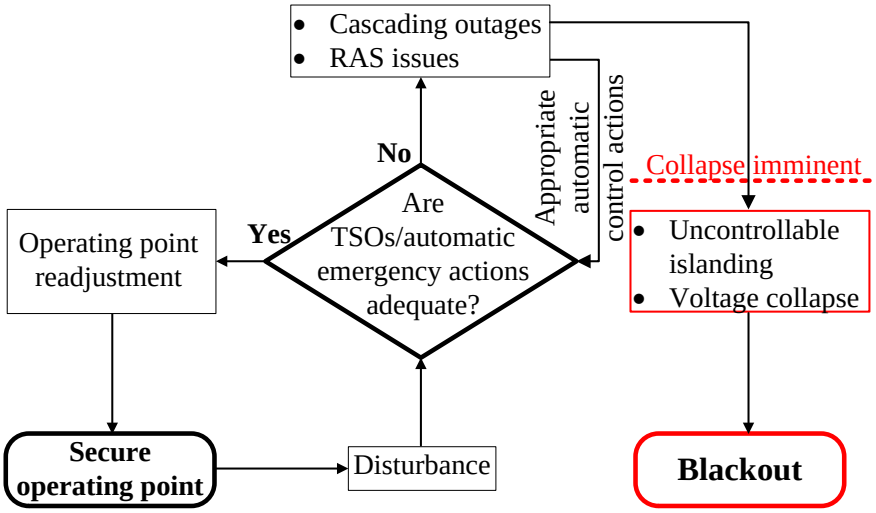

Figure 1.4: General scenario of a blackout in power systems

The DSA strategies have gradually transformed in order to follow up with evolving circumstances in power system operation. In this sense, DSA has made a long way from a purely off-line analysis [38] to the one that comprises various off-line and on-line tools [39]. Nowadays, the three main classes of DSA methods stand out [40]: simulation-based approaches [41], pattern-recognition techniques [42] and expert system methods [43]. The simulation programs either rely on numerical integration or they utilize the analytical concepts that are derived for the purpose of DSA (e.g. Transient Energy Function (TEF) [44], SIngle Machine Equivalent (SIME) [45] and alternatively, trajectory sensitivities [46]). The second, machine learning class of methods [47, 48] is of more recent date and it combines the

decision trees [49] with the quantities established by Supervisory Control And Data Acquisition (SCADA) [50] or Phasor Measurement Units (PMUs) [51]. The last class listed (expert system methods) is partially heuristic as it is based on particular TSOs' experience/knowledge [52] and a set of inference rules. The DSA means vary greatly, yet, the final aim of all DSA methodologies is the same. The duty of DSA is to estimate the dynamic security region as the collection of the modes of operation where the risk of power system instability is regarded as acceptable.

Although the dynamic stability aspects are diverse and plentiful, the DSA programs are mostly interested into the electromechanical dynamics which are inherent to large disturbances [53]. Large disturbances are capable to jeopardize the basic principle of power system operation, i.e. its ability to maintain the synchronism of Alternating Current (AC) generators [54]. In the standardized classification of power system stability [55] that is depicted in Fig. 1.5, the transient stability of rotor angles and short-term voltage stability are the ones that reflect the events in the electromechanical timescale (hundredths of seconds to tens of seconds).

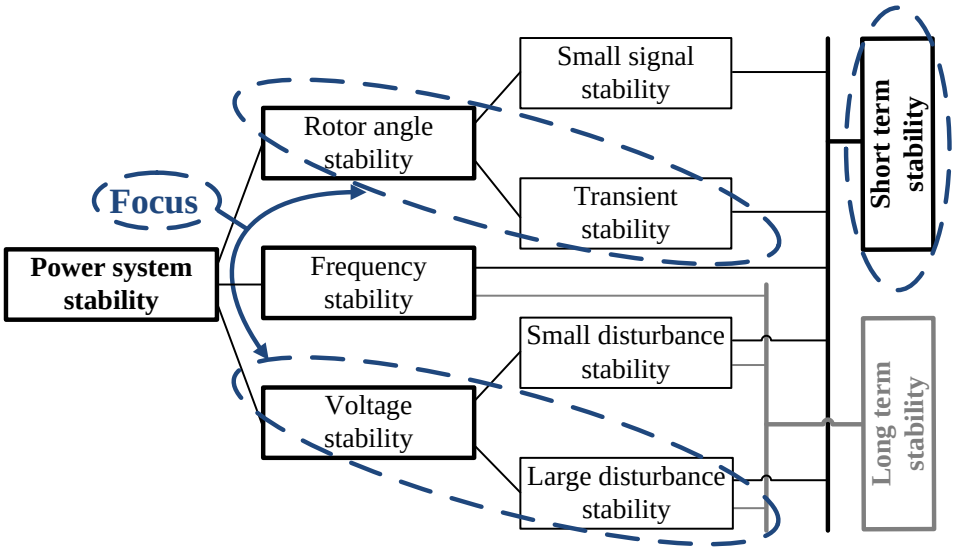

Figure 1.5: Thesis focus in the standard classification of power system stability

Transient stability (also known as short-term Rotor Angle Stability (RAS)) is the governing short-term instability mechanism [56] that gives rise to other stability issues, including over/under voltage transients. If the lack of synchronizing power is present, out-of-step relays may trip the lines due to depressed voltage which

results in the partitioning of a power system. Partitioning methods (e. g. spectral clustering [57]) are important constituents of a DSA platform. Furthermore, short-term frequency stability is normally challenged due to the formation of islands with power imbalance. A deficit of power may lead to a rapid decay of frequency and then the consequential blackout of the island is a matter of seconds [58]. Henceforward, this thesis will principally address two types of stability from Fig. 1.5:

- **Large-disturbance RAS (transient stability)** which refers to the ability of the power system to remain in synchronism after being subjected to some severe disturbance. After a disturbance, the insufficient synchronizing torque may result in increasing angular swings of some AC generators. This phenomenon which typically occurs in the first 3-5 [s] after a disturbance is often referred to as *first-swing instability*. It could as well happen that a large group of generators in one area oscillates against another large group of generators from a different area. The resulting oscillations, known as interarea swing mode of oscillations, are slower and they may interact with local plant mode oscillations by prolonging the RAS time-scale to as much as 20 [s] for very large systems [59].

- **Large-disturbance short-term voltage stability** is of interest in the several seconds successive to a large disturbance (it is "voltage analogous" to transient stability analysis). In general, large-disturbance voltage stability analysis has the aim to determine if a power system is capable to maintain stable voltage profiles at system buses after a contingency occurs. The standard large-disturbance short-term voltage instability assessment involves the dynamics of components that respond fast to contingencies (e.g. HVDC (High Voltage Direct Current) converters, induction motors, electronically controlled loads [55, 60] etc.). When it comes to short-term voltage instability, the most serious event is *voltage collapse*. Voltage collapse denotes the progressive, substantial drop of voltages that is voltage-instability-provoked. The voltage dropping to abnormal levels may alternatively lead the power system into a blackout [61, 62].

The usual practice is that the two types of stability are assessed separately. In the continuation, the analysis will lay stress on large-disturbance RAS and relatively unknown voltage collapse that may occur as the rotors oscillate. The voltage collapse of interest has a driving force that is different than the aforementioned dynamics of fast acting load components. In that sense, the thesis will focus on both the separate and common treatment of the important short-term stability mechanisms.

1.2 Challenges and research motivation

The main concern of DSA in the power utilities of modern interconnected systems is fault propagation. It is important to understand the system response to faults in order to determine the list of critical contingencies and corresponding stability margins. The Critical Clearing Time (CCT) is one of the ways to measure how critical a contingency is. Before carrying out any further security assessment, DSA needs to evaluate RAS in seconds after large disturbances (i.e. transient stability). The safe operation of a power system is unattainable without the stable/damped electromechanical dynamics that are triggered by large disturbances [54]. By leaving the expert system methods aside (due to their heuristic nature), the RAS approaches proposed so far may be divided into the following two areas:

- **Simulation programs** that are implemented in most of the commercial softwares. These programs are usually based on some analytical concept out of which the most important ones will be briefly reviewed in the sequel.

  - *Time Domain Simulation (TDS)*, the classical RAS tool, performs the numerical integration of the set of Differential Algebraic Equations (DAE) that describe the dynamics of the system in the fault-on and the post-fault period. The procedure is then repeated for the most dangerous contingencies. The results obtained by TDS are very accurate due to the possibility to use detailed models (dynamics of generators, loads, control devices and influence of protection systems may be included). TDS also provides information about the state variables in the transient period.

    Although the classical TDS is convenient for the off-line analysis in the system planning phase, for large power systems thousands of differential and algebraic equations should be solved which is time consuming. Therefore, TDS is not suitable as a tool for on-line RAS assessment. Researchers have attempted to develop methods that are based on large-step-size numerical integration [63], however, the improvement with the existing utilities is not significant. Another disadvantage is that TDS is incapable to give information about stability margins [64]. The knowledge about stability margins would enable the TSOs to create preventive actions for a specific contingency and operating point.

  - *Direct methods* (also known as Transient Energy Function (TEF) methods) have been introduced in the late 40's [65] to support on-line RAS

assessment by relieving the computational burden of TDS. The further development of direct methods [66–68] originated from the idea to replace the integration of DAE in the post-fault period with a stability criterion. The "measure" of stability—stability index is then calculated based on energy-like Lyapunov functions. The relation between the actual stability index and the critical value of the index (i.e. critical energy) represents the quantitative measure of RAS (stability margin).

Direct methods do not provide TSOs with knowledge about state variables for the post-fault period. Nevertheless, the main limitation of direct methods is the construction of proper energy functions [69] for general power system models with transfer conductances. In these cases, there is no analytical energy function and approximations are to be made [70]. Another challenge rises from the concepts that are employed in order to calculate the critical energy. These issues are numerical in nature and they are mostly related with the choice/identification of the Unstable Equilibrium Point (UEP) of interest [71–73]. The improvements in the construction of energy-functions are continuously made, and some of them are of recent date [74–76]. However, the unified solution has not yet been reached and the challenges in TEF construction persist.

– *SIngle Machine Equivalent (SIME)* method is a hybrid direct-temporal method that combines TDS and TEF to assess transient stability [77,78]. The SIME method unifies the multi-machine system trajectories into a single trajectory. As the first step, the TDS program is used to identify the mode of separation of the machines in order to create the two-machine equivalent of a power system. It is enough to carry out a single TDS that results in instability to determine the mode of machine separation. Further on, the two-machine equivalent is replaced by a SIME with time-varying parameters. Once having the SIME, the Equal Area Criterion (EAC) [54] can be directly applied to assess transient stability of the power system (and determine CCT, for instance). As such, the SIME method combines the advantages of TDS and TEF—it has high accuracy, it is fast and it provides the information that is important for the TSOs (e.g. the stability margin data, the information about the mode of machine separation and corresponding critical machines etc.).

– *Trajectory Sensitivities (TS)* approach estimates the sensitivity of a state variable to a small perturbation of a system parameter, via analytical [46] or numerical formulation [79]. The idea of trajectory sensitivity analysis

was to linearize the system around the trajectory with respect to some important system parameter. Although the stability margin is available and there are no modeling constraints in this case, the sensitivity analysis is computationally more intensive than the previously reviewed methods.

The drawback of all these approaches that are commonly used in simulation programs is that they investigate a specific operating state (o.s.) and associated phenomenon. When a change in the operating conditions occurs, a completely different stability criterion may hold. Although the trajectory sensitivity analysis may resemble the solution of this problem, this linearization-based method is only reliable when the change in parameters is incremental.

- **Pattern Recognition Methods (PRM)** made a step further towards on-line RAS assessment by establishing the functional relationship between the o.s. and corresponding stability margin [80]. PRM consist of two stages. The first stage reduces the dimensionality of the problem by an off-line construction of the training set that extracts the power system feature of importance. In the second stage, the classifier function is determined with the help of the training set. It is usually proposed to train Artificial Neural Network (ANN) as the classifier function [81, 82]. The ready-trained estimators are capable to make stability predictions for the operating states that were not included in the training set.

  The problems with the estimation accuracy of ANN (and of other classifier function techniques) often happen when network conditions vary [83]. *However, the main shortcoming of the pattern/data recognition methods is that they provide functional, and not analytical relations.*

Hence, the challenges in nowadays RAS assessment are various. Short-term voltage stability assessment has not been mentioned here in the context of methodology since DSA simulation programs do not model the explicit automatic actions that are related to over/under voltages. Voltage stability assessment rely on the monitoring of the voltage transients while RAS is analyzed. So far, short-term voltage stability has been treated as the issue that arises from fast-reacting component dynamics. For instance, stalling of the induction motor loads is considered to be one of the main factors contributing to short-term voltage instability (and slow post-disturbance voltage recovery [84]). Nonetheless, the voltage-related problems in DSA simulations may happen even when “ordinary" static load models (other than the constant impedance

model) are employed. Very few works in this field ascribed these incidents to the existence of “impasse surfaces" [85] or “singularity surfaces" [86] where “voltage causality" is lost. *Yet, the structured research that analytically describes the loss of voltage causality, its connection to RAS region and load modeling has not been carried out so far.*

As the summation of the two previous subsections, the following research motivation and the corresponding challenges may be outlined:

1. Motive (1.M): Due to the global importance of RAS assessment in power system security, there is a need for an efficient on-line DSA tool in order to meet the (N-1) criterion at all times.

- Challenge (1.1C): The existing DSA methodologies are either slow (TDS), computationally demanding (TDS, TS), imprecise/unreliable (TEF, PRM) or they require modeling simplifications (TEF).
- Challenge (1.2C): The DSA simulation programs either focus on one contingency and one operating point at a time (TDS, TEF) or they may support a very small change in system parameters (TS). With every larger change of the parameters (operating condition), new RAS assessment should take place.
- Challenge (1.3C): PRM do not provide analytical relationship between the operating conditions and RAS (e.g. estimated CCT). This means that even if PRM would always estimate with high accuracy (which is not the case), CCT can be found based on the operating conditions but not vice versa.

2. Motive (2.M): In RAS assessment, rotor oscillations may induce voltage instability issues that are not linked to dynamic modeling of loads. In order to prevent unexpected voltage collapse on a power swing, this phenomenon needs a precise analytical description.

- Challenge (2.1C): The majority of the large-disturbance voltage stability methods deal with the short-term effects of fast-responsive dynamical loads.
- Challenge (2.2C): The works on impasse surfaces linked the non-existence of DAE solution in state-space with the loss of voltage causality due to the non-linear modeling of static loads. However, this connection between short-term voltage collapse and transient stability has not been established in analytical form until now.

The description on how this thesis approached the identified challenges follow.

1.3 Scope and main objectives

The work of this thesis is comprised of both short-term RAS and voltage collapse phenomena that are associated to large disturbances. The most appropriate is to place the thesis into the framework of on-line DSA, since the main concerns of DSA are RAS and voltage transients. The aim of the work was to make improvements with respect to the Motives (1.M-2.M) and Challenges (1.1C-2.2C) that are counted in the previous subsection. Following the list, the main objectives of the thesis are:

1. Objective (1.O): To construct an improved RAS methodology that outperforms the existing approaches. In order to be considered as an improvement, the newly proposed RAS methodology must satisfy the following requirements:

- (1.1O): The method needs to be comparatively fast, precise and it should not impose modeling constraints. It should also be possible to assess stability margin information.
- (1.2O): It is expected that the method is capable to carry out the short-term RAS assessment under large perturbations of the o.s. without facing the problems with the accuracy of estimates.
- (1.3O): The methodology should define the short-term RAS index as an analytical function of the o.s. (e.g. CCT=f(o.s.)). The aim is also to be able to inverse this function (o.s.=f^{-1}(CCT)) if a certain set of o.s. is required to be estimated instead of CCT.

2. Objective (2.O): To investigate the coupling between RAS and voltage collapse that occurs in seconds after large disturbances. In that sense, the two groups of questions to be answered are:

- (2.1O): Do the non-linear static models of load affect the loss of voltage causality along a post-fault trajectory? What are the practical implications of these events when it comes to DSA simulation?
- (2.2O): If the connection between aforementioned load modeling and impasse surfaces exists, what are the reasons for that (analytically speaking)? Are there some means to predict short-term voltage collapse in these cases?

It is considered that this thesis has fulfilled its aim once the given Objectives (1.O-2.O) are adequately addressed.

1.4 Scientific contributions

On its way to tackle the Objectives (1.O-2.O), this thesis first provides an insight into the short-term stability issues of interest. This means that the existing models, analytical and numerical tools are to be clearly presented. The thesis contributions are hereby listed in the form of solutions to the corresponding objectives:

1. Solution (1.S): The new methodology for short-term RAS assessment is proposed. The base for the approach is that the perturbation of the operating point is described by the parametrization of RAS stability boundary, i.e. the interesting parts of the stability boundary are mapped into the points of the security boundary by means of polynomial regression [J1,C1].

- (1.1S): The data for the boundary construction is collected by TDS, however, very small number of points is needed due to the proper choice of the parametrization technique. Several data collection approaches and parametrizations (axis of the multidimensional parameter-space) are proposed and compared. The final choice is the newly introduced parametrization that has a physical meaning and represents the directional sensitivity of the SIME equivalent to the changes in operating conditions. The result is a method that is accurate enough and can be applied without limitations in terms of modeling. Once the boundaries are constructed, they may be assessed on-line while providing the stability margin information (the difference between actual clearing times and CCT).

- (1.2S): The parameter-space boundary is constructed by means of non-linear analysis and is therefore suitable for RAS assessment even when the o.s. drastically change.

- (1.3S): The polynomial regression model of the security boundary is introduced in order to: (i) provide the analytical dependency between CCT and parameters and (ii) enable the manipulation with the polynomial coefficients such that Quadratic Programming (QP) can be applied for the purposes of conservative CCT estimation.

2. Solution (2.S): The coupling between the short-term RAS and voltage stability has been established by introducing and defining the concept of Voltage Impasse Regions (VIR). The VIR may appear inside RAS region and interfere with stability assessment [J2].

- (2.1S): The mathematical model for the voltage collapse study has been derived and the voltage magnitudes have been defined as the functions of relative rotor angles. The obtained expressions for voltage magnitudes led to the conclusion that for some points along the post-fault trajectory, DAE system faces singularity and TDS exhibits problems with convergence.
- (2.2S): The thesis determined that if the non-linear static loads are employed, the solutions for voltage magnitudes become impossible at certain state-space areas that are denoted as VIR. Extensive analysis has been carried out to precisely define VIR and determine the mechanisms leading to its appearance. Additionally, several Voltage Collapse Indicators (VCIs) are proposed as the metrics of proximity to a VIR with respect to different load models.

JCR journal papers:

[J1] M. Oluic, M. Ghandhari and B. Berggren, “Methodology for rotor angle transient stability assessment in parameter space", *IEEE Trans. Power Syst.*, vol. 32, no. 2, pp. 1202-1211, Mar. 2017.

[J2] M. Oluic, B. Berggren, F. M. Echavarren, M. Ghandhari and L. Rouco, “On the nature of voltage impasse regions in power system dynamics studies”, *IEEE Trans. Power Syst.*, vol. 33, no. 3, pp. 2660-2670, May 2018.

Conference papers:

[C1] M. Oluic, M. Ghandhari and B. Berggren, “On the parametrization of rotor angle transient stability region”, *2015 North American Power Symposium (NAPS)*, Charlotte, NC, 2015, pp. 1-6.

1.5 Thesis outline

The thesis has been organized in chapters with the following outline:

Chapter 2 provides the mathematical models of the power system and its components that are used in this thesis. The chapter also contains a brief review of the RAS region characteristics and the description of the stability analysis methods that are of interest.

Chapter 3 presents the theory and the results of the newly developed methodology for short-term RAS assessment in parameter-space.

Chapter 4 introduces the concepts of SIME-based parametrization and imposes the constraints on the parametrized security boundaries by the means of QP.

Chapter 5 first reviews the static/dynamic aspects of voltage stability assessment and then introduces VIR as a state-space region.

Chapter 6 gives the analytical formulation of the VIR and discusses how the non-impedance static load type and size influence the VIR.

Chapter 7 draws the final conclusions of the thesis and reflects the potential ideas/aims to be addressed in future.

The locations of the thesis contributions from the Solution list (previous subsection) are marked in Table 1.1 that is given below.

Table 1.1: The distribution of the Solutions (1.1S-2.2S) in the thesis outline

Solution	Chapter 2	Chapter 3	Chapter 4	Chapter 5	Chapter 6
(1.1S)	✓	✓	✓		
(1.2S)		✓	✓		
(1.3S)		✓	✓		
(2.1S)				✓	✓
(2.2S)					✓

Chapter 2

Power System Modeling and RAS Assessment

This chapter presents an overview on the modeling, numerical and analytical concepts that are employed in short-term RAS analysis. The overview provides the particular mathematical models of multi-machine power system and its components, as well as the foundation of the TDS/direct methods that will be used in the thesis.

2.1 Foreword

The transient stability (or short-term RAS) analysis deals with the electromechanical oscillations of rotor angles that occur in the first seconds following a large disturbance. The typical large disturbances are, for instance, short-circuits, tripping of a long transmission line, generator outage and the loss of large portions of load [54]. These events may or may not have to be correlated, and their sequence depends on the protective system reaction and the initial operating point. If a large disturbance results in unbounded increasing rotor angles of one or more AC generators, the synchronism is lost. When dealing with large disturbances, it is necessary to take into account the non-linear nature of the power system and its components. Depending on the assumptions regarding the system modeling, this is done by employing either a set of Ordinary Differential Equations (ODE) or a set of Differential Algebraic Equations (DAE). Both equation sets describe the system dynamical behaviour. The evaluation of the power system ability to remain in synchronism then usually comes down to (i) some sort of quantification of transient stability (such as Critical Clearing Times (CCT) or critical energy) and (ii) identification of (in)stability/

margins for contingencies of importance. For the purpose of better understanding of the aforementioned concepts, the general non-linear power system model, the modeling of the specific components and a brief explanation of the methods of interest follow in the sequel.

2.2 General power system model and its components

While a power system operates in a steady-state, the operating condition can be determined from the *power flow calculations*. The power flow equations are based on the Kirchoff's current law [87] which states that the sum of currents (or powers) flowing into a junction of a circuit (i.e. bus) is equal to the sum of currents (powers) leaving the same bus. The power flow solution would be completely sufficient if there is such thing as a perfect steady-state. Nevertheless, the operating conditions continuously fluctuate in power systems, where a majority of changes are small enough to be well-described by the means of linearization. In the sense of RAS (and based on the classification from Fig. 1.5), this is the task for Small Signal Stability Analysis (SSSA) [88]. The SSSA linearizes the non-linear model of a power system around the operating point to examine the stability characteristics, most often via eigenvalue analysis [89].

However, the power system "moves" far away from the operating point once a large disturbance takes place. This is when the linearized models are not a valid representation of power system behaviour. For the analysis of large disturbance dynamics, it is necessary to consider a full, general model of a power system that is given by a set of Differential Algebraic Equations (DAE):

$$\begin{aligned} \dot{\boldsymbol{x}} &= \boldsymbol{f}(\boldsymbol{x}, \boldsymbol{y}); \\ \mathbf{0} &= \boldsymbol{g}(\boldsymbol{x}, \boldsymbol{y}), \text{ where:} \end{aligned} \tag{2.1}$$

- $\boldsymbol{f}(\boldsymbol{x}, \boldsymbol{y})$ is the vector-valued function that denotes the differential part of (2.1);
- $\boldsymbol{g}(\boldsymbol{x}, \boldsymbol{y})$ represents the set of the algebraic equations;
- $\boldsymbol{x}$ and $\boldsymbol{y}$ are the vectors that contain the state and algebraic variables, respectively.

The structure of the vector of state variables $\boldsymbol{x}$ depends on the chosen modeling of the dynamical components (in particular, generating units). The vector of the algebraic variables $\boldsymbol{y}$ usually consists of the voltage magnitudes and the voltage angles of the system buses. If the number of the state and algebraic variables are denoted by n_x and n_y, respectively, the vector $\boldsymbol{x}$ has dimension $n_x \times 1$ and the

vector $\boldsymbol{y}$ is of $n_y \times 1$ size. In the steady-state, when the dynamics are not present, the initial pre-fault conditions at $t = t_0$ may be solved from:

$$0 = \boldsymbol{f}(\boldsymbol{x_0}, \boldsymbol{y_0}) \quad \text{and} \quad 0 = \boldsymbol{g}(\boldsymbol{x_0}, \boldsymbol{y_0}), \tag{2.2}$$

where the initial operating point is given by $\boldsymbol{x_0} = \boldsymbol{x}(t_0)$ and $\boldsymbol{y_0} = \boldsymbol{y}(t_0)$. Practically, $\boldsymbol{y_0}$ is usually found first by running the power flow. The initial vector of state-variables ($\boldsymbol{x_0}$) is then calculated based on the previously obtained $\boldsymbol{y_0}$.

The structure of realistic power systems is complex. The electrical power is first produced in generating units. The principle of operation of the generating units depends on the type of the energy source (hydro, solar, nuclear, wind or thermal energy [90], for example) that needs to be converted into electrical power. After passing through the step up transformers, this power is then carried by the high voltage transmission lines to the step down transformers that are connection points for the demand centers. To analyze the static and dynamic conditions in power systems, simplifications need to be made in order to have compact models. A general, simplified representation of a power system that has n generators (G_k, $k = 1, ..., n$) and a total of N load buses is depicted in Fig. 2.1.

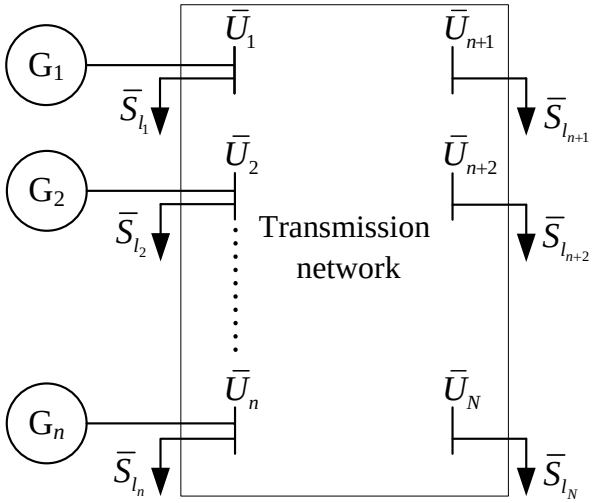

Figure 2.1: The general model of a power system

Out of the N load buses, the first n buses are known as generator terminal buses. At each of the N buses, a load (represented by its complex power $\bar{S}_{l_k}$, $k = 1, ..., N$) may be connected. The transmission network represents the meshed

grid that consists of lines that transmit the required power from the generation to the loads.

In order to apply the DAE form (2.1) to the model from Fig. 2.1, the modeling of the specific components first needs to be defined. Depending on the proposed study, different power system components (and corresponding models) may be included. The aim of this thesis is to further develop the analytical concepts that are related to RAS and to provide an insight into the state-space characteristics. In order to be able to distinguish between the important mechanisms and the ones that do not influence the investigated phenomenon, the following modeling is employed.

2.2.1 Synchronous generator

The total number of state variables in the power system is mostly affected by the choice of the dynamic modeling of the generators (G_k). The phenomenon of interest determines how detailed the generator model should be. Since short-term RAS deals with the loss of synchronism (rotor angle dynamics), this type of stability studies may consider the classical model of the generator [54]. In this model, the generator is given by a voltage source (with a constant magnitude) behind d-axis transient reactance, as shown in Fig. 2.2.

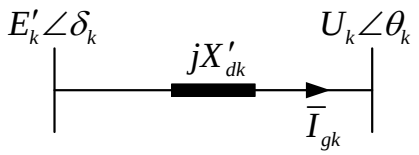

Figure 2.2: The equivalent circuit of the classical model of a synchronous generator

The classical model is a dynamical system of the second order — it describes the dynamics of the rotor angles and the angle speeds. In the electrical circuit of the k^{th} generator ($k = 1, ..., n$) from Fig. 2.2:

- $\bar{E}'_k = E'_k\angle\delta_k$- is the phasor of the internal transient voltage of the k^{th} generator, with the constant magnitude $E'_k = const.$ and the rotor angle δ_k;
- X'_{dk} - denotes the k^{th} machine d-axis transient reactance which here also includes the reactance of the associated k^{th} transformer;
- $\bar{U}_k = U_k\angle\theta_k$ - outlines the phasor of the voltage at the terminal bus of the k^{th} generator, with the magnitude U_k and the voltage angle θ_k and

- $\bar{I}_{gk}$ - stands for the current of the k^{th} generator.

In the case of classical model, the dynamics of the k^{th} synchronous generator ($k = 1, ..., n$) from the Fig. 2.2 are fully defined by the swing equation in per unit [p.u.] as [91]:

$$\begin{aligned} \dot{\delta}_k &= \omega_k; \\ \dot{\omega}_k &= \frac{1}{M_k}(P_{mk} - P_{ek} - D_k\omega_k), \end{aligned} \tag{2.3}$$

where the two state variables are (i) δ_k (rotor angle measured from synchronously rotating reference) and (ii) ω_k (the deviation of the rotor angle speed from synchronous speed ω_s). The active electrical power input of the generator is denoted as P_{ek} and it can be derived from the complex electrical power that the k^{th} generator injects into its terminal bus as:

$$P_{ek} = \mathrm{Re}(\bar{U}_k\bar{I}^*_{gk}) = \frac{E'_kU_k\sin(\delta_k - \theta_k)}{X'_{dk}}. \tag{2.4}$$

For the k^{th} generator with rated three-phase apparent power S_{ng_k}, the remaining parameters from the model (2.3) are given as follows:

- $M_k = 2H_kS_{ng_k}/\omega_sS^{3\phi}_{base}$ - is the constant that reflects the inertia H_k of the k^{th} generator, where $S^{3\phi}_{base}$ is arbitrarily chosen three-phase base power;
- P_{mk} - denotes the mechanical power of the generator that is assumed to be constant in the case of the classical model (i.e. $P_{mk} = const.$) and
- D_k - is a small, positive damping constant that represents the inherent damping of the generator.

2.2.2 Load models

This thesis will employ the static load models that express the load power via voltage dependency. This means that standard static load models, ZIP model and exponential model [92], omit the dynamics of loads. The argument for using this type of load model is that load dynamics are not the driving mechanism for the short-term rotor angle instability. The dynamic load models are of particular importance for short-term and long-term voltage stability studies. However, this thesis aims to investigate the short-term voltage stability issues that are not related to load dynamics. This is the main reason why the dynamic load models are not considered.

When the static load model is employed, the load at any terminal or purely load bus k ($k = 1, ..., N$) from Fig. 2.1, may be represented by its complex power:

$$\bar{S}_{l_k} = P_{l_k} + jQ_{l_k}. \tag{2.5}$$

Complex power $\bar{S}_{l_k}$ may relate to a specific static load model or it can be given in a more general form. Both variations contain only algebraic equations that enable the dynamic incorporation of a load connection to some bus k, as shown in Fig. 2.3.

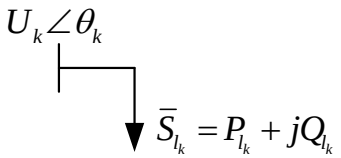

Figure 2.3: The representation of the static load connection

The simplest load representation is known as exponential static load model. In the exponential model, the active and reactive components of the complex load power at bus k are given as the functions of the voltage magnitude at the same bus:

$$\begin{aligned} P_{l_k} &= P_{l_{k0}} \left(\frac{U_k}{U_{k_0}} \right)^{mp}; \\ Q_{l_k} &= Q_{l_{k0}} \left(\frac{U_k}{U_{k_0}} \right)^{mq}, \quad \text{where} \end{aligned} \tag{2.6}$$

- mp, mq - are the voltage exponents that correspond to the active and reactive load power, respectively;
- U_{k_0} - is the initial value of the voltage magnitude at bus k and
- $P_{l_{k0}}, Q_{l_{k0}}$ - are the values of the active and reactive load power at voltage U_{k_0}.

The values $mp = mq = 0$ represent constant power load, $mp = mq = 1$ are used for constant current characteristic and $mp = mq = 2$ represent constant impedance load model. Different combinations of the parameters mp and mq are applicable, and then the load model is of composite type.

The more general approach involves the employment of the ZIP load model where the load power consists of three components—constant impedance (Z),

constant current (I) and constant power (P) component. In the ZIP model, the active and reactive components of the complex load power $\bar{S}_{l_k}$ are expressed as:

$$\begin{aligned} P_{l_k} &= P_{l_{k0}}\Big[k_{Pz}(\frac{U_k}{U_{k_0}})^2 + k_{Pi}(\frac{U_k}{U_{k_0}}) + k_{Pp}\Big] \text{ and} \\ Q_{l_k} &= Q_{l_{k0}}\Big[k_{Qz}(\frac{U_k}{U_{k_0}})^2 + k_{Qi}(\frac{U_k}{U_{k_0}}) + k_{Qp}\Big]. \end{aligned} \tag{2.7}$$

The parameters k_P and k_Q define how large is the fraction of each load component (constant impedance (Z), constant current (I) and constant power (P) component). These parameters ($k_{Pz}, k_{Pi}, k_{Pp}, k_{Qz}, k_{Qi}$ and k_{Qp}) can vary in the range $[0, 1]$ while the equality $k_{Pz} + k_{Pi} + k_{Pp} = k_{Qz} + k_{Qi} + k_{Qp} = 1$ also needs to hold.

2.2.3 Line model

Once the choice is made for the generators and loads, the model for the lines of the transmission network from Fig. 2.1 should also be defined. The standard model of long, transmission lines that is usually used for the purposes of power system analysis is known as the Π model [93]. The Π model represents a line between some buses k and p as a series impedance ($\bar{Z}_{kp} = R_{kp} + jX_{kp}$) and a shunt admittance ($\bar{Y}_{sh-kp}$) that is connected to the ground. The shunt is divided into two equal parts ($\bar{y}_{sh-kp} = jb_{sh-kp}$) that are connected at the two ends of the line. Every line that connects some bus k with another bus p will in this thesis be represented by a slightly simplified Π model with a purely reactive series impedance ($R_{kp} = 0$), as in Fig. 2.4. This assumption has a physical meaning since $X_{kp} \gg R_{kp}$ for transmission lines.

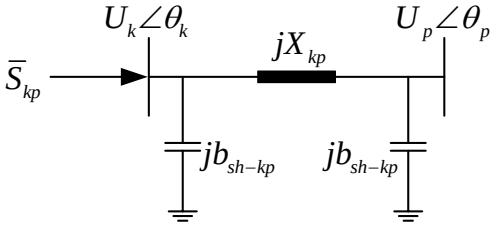

Figure 2.4: Π-model of a transmission line

The reactive series impedance between the buses k and p may also be written in the admittance form:

$$\bar{y}_{kp} = \frac{1}{jX_{kp}} = jb_{kp}, \quad \text{where} \quad b_{kp} = -\frac{1}{X_{kp}}. \tag{2.8}$$

Now the active and reactive parts of the complex power ($\bar{S}_{kp} = P_{kp} + jQ_{kp}$) that is transmitted through the line are seen at the end k as:

$$\begin{aligned} P_{kp} &= -U_k U_p b_{kp} \sin(\theta_k - \theta_p) \\ Q_{kp} &= (-b_{sh-kp} - b_{kp}) U_k^2 + U_k U_p b_{kp} \cos(\theta_k - \theta_p), \ \forall k, p = 1, ..., N \wedge k \neq p. \end{aligned} \tag{2.9}$$

For the case of the general power system with N buses, the whole transmission network will be represented by the $(N \times N)$ admittance matrix $\mathbf{Y_{BUS}}$:

$$\mathbf{Y_{BUS}} = \mathbf{G_{BUS}} + j\mathbf{B_{BUS}} = \begin{bmatrix} \bar{Y}_{11} & \bar{Y}_{12} & \dots & \bar{Y}_{1N} \\ \bar{Y}_{21} & \bar{Y}_{22} & \dots & \bar{Y}_{2N} \\ \vdots & \vdots & \ddots & \vdots \\ \bar{Y}_{N1} & \bar{Y}_{N2} & \dots & \bar{Y}_{NN} \end{bmatrix}. \tag{2.10}$$

The matrix $\mathbf{Y_{BUS}}$ may always be uniqely determined by inspection for a given transmission network. Since the network is assumed to be lossless ($\mathbf{G_{BUS}} = 0$), the admittance matrix $\mathbf{Y_{BUS}}$ only has the reactive component $j\mathbf{B_{BUS}}$. Considering the line model from Fig. 2.4, the non-diagonal and diagonal entrances of the admittance matrix may be defined as follows:

$$\bar{Y}_{kp} = jB_{kp} = -jb_{kp} \qquad \text{for } k, p = 1, ..., N \wedge k \neq p, \tag{2.11}$$

$$\bar{Y}_{kk} = jB_{kk} = \sum_{\substack{p=1 \\ p \neq k}}^{N} j(b_{kp} + b_{sh-kp}) \qquad \text{for } k = 1, ..., N, \tag{2.12}$$

respectively.

2.3 Dynamic modeling of multi-machine power systems

Now that all the power system elements of interest for the thesis have been presented, the general multi-machine models can be formulated.

2.3.1 DAE model of multi-machine power systems

As mentioned before, the dynamical model of a multi-machine power system consists of differential and algebraic parts. Based on the modeling from the previous section, the set of the differential equations for the n-machine model is given as:

$$\begin{aligned} \dot{\delta}_k &= \omega_k; \\ \dot{\omega}_k &= \frac{1}{M_k}(P_{mk} - P_{ek} - D_k\omega_k), \quad \text{for} \quad k = 1, ..., n. \end{aligned} \tag{2.13}$$

The algebraic set of equations represents the active and reactive power mismatch equations for all N system buses:

$$\begin{aligned} 0 &= P_k + P_{l_k}; \\ 0 &= Q_k + Q_{l_k}, \quad \text{for} \quad k = 1, ..., N, \end{aligned} \tag{2.14}$$

where P_k and Q_k are the real and reactive powers that are injected into bus k, respectively. The definition of the active and reactive powers differ depending on the bus type. For generators terminal buses ($k = 1, ..., n$), these injected powers may be defined as:

$$\begin{aligned} P_k &= \sum_{p=1}^{N} B_{kp} U_k U_p \sin(\theta_k - \theta_p) - \frac{E'_k U_k \sin(\delta_k - \theta_k)}{X'_{dk}}; \\ Q_k &= -\sum_{p=1}^{N} B_{kp} U_k U_p \cos(\theta_k - \theta_p) - \frac{E'_k U_k \cos(\delta_k - \theta_k) - U_k^2}{X'_{dk}}, \end{aligned} \tag{2.15}$$

and for the other buses ($k = n + 1, ..., N$), the injected active and reactive powers are:

$$\begin{aligned} P_k &= \sum_{p=1}^{N} B_{kp} U_k U_p \sin(\theta_k - \theta_p); \\ Q_k &= -\sum_{p=1}^{N} B_{kp} U_k U_p \cos(\theta_k - \theta_p). \end{aligned} \tag{2.16}$$

When written in the form of Eqs. (2.13) and (2.14), the multi-machine power system is now fully defined as the general DAE model:

$$\begin{aligned} \dot{\boldsymbol{x}} &= \boldsymbol{f}(\boldsymbol{x}, \boldsymbol{y}); \\ \mathbf{0} &= \boldsymbol{g}(\boldsymbol{x}, \boldsymbol{y}), \end{aligned} \tag{2.17}$$

where the vectors of the state and algebraic variables are:

$$\begin{aligned} \boldsymbol{x} &= \begin{bmatrix} \delta_1 & \delta_2 & \dots & \delta_n & \omega_1 & \omega_2 & \dots & \omega_n \end{bmatrix}^T \\ \boldsymbol{y} &= \begin{bmatrix} U_1 & U_2 & \dots & U_N & \theta_1 & \theta_2 & \dots & \theta_N \end{bmatrix}^T. \end{aligned} \tag{2.18}$$

The vector of state variables $\boldsymbol{x}$ contains generator rotor angles and angle speeds and the vector of the algebraic variables $\boldsymbol{y}$ represents the magnitudes and angles of

buses voltages. The given power system model is known as the Structure Preserving Model (SPM) [94]. In SPM, all the system buses are retained. The main advantages of this detailed model are that (i) it preserves the original network topology and (ii) it provides freedom in terms of modeling. Another option is to simplify the SPM of a power system by suppressing the load buses. To make this reduction, all the loads need to be of a certain type. This model is known as Reduced Network Model (RNM), and its characteristics are given in the following subsection.

2.3.2 RNM model of multi-machine power systems

Multi-machine power system can also be given in the form of Reduced Network Model (RNM) [95] where only generators buses are preserved. The aim of RNM is to simplify dynamical analysis by replacing a DAE system with a system of Ordinary Differential Equations (ODE). To do the reduction from SPM to RNM, the augmented power system from Fig. 2.5 is used.

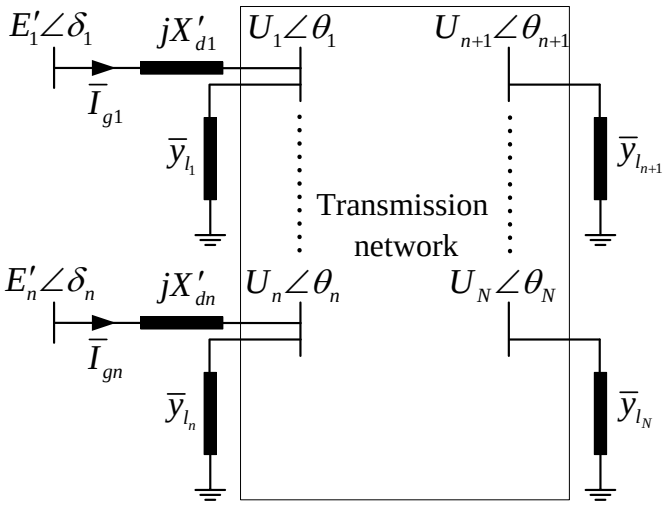

Figure 2.5: The power system model for reduction of DAE to ODE

Considering the modeling of components that is given in this thesis, the only additional assumption for the model in Fig. 2.5 is that all the loads ($k = 1, ..., N$) are modeled as constant admittances/impedances ($\bar{y}_{l_k}/\bar{Z}_{l_k}$), i.e.:

$$\bar{y}_{l_k} = \frac{1}{\bar{Z}_{l_k}}, \text{ where } \bar{Z}_{l_k} = R_{l_k} + jX_{l_k} = \frac{U_k^2}{P_{l_k} - jQ_{l_k}}. \tag{2.19}$$

Now let matrix $\mathbf{Y_{LOAD}}$ to be defined as an $N \times N$ diagonal matrix where $(k,k)^{th}$ entrances ($k = 1, ..., N$) are the load admittances $\bar{y}_{l_k}$. The new admittance matrix is constructed then as $\mathbf{Y'_{BUS}} = \mathbf{Y_{BUS}} + \mathbf{Y_{LOAD}}$, in which the $(k,p)^{th}$ element of $\mathbf{Y'_{BUS}}$ is given by $\bar{Y}'_{kp} = G'_{kp} + jB'_{kp}$. To derive the mathematical model of RNM, all the algebraic variables in the differential part of the model (2.17) need to be expressed as functions of state variables. This is always possible to do when all the loads are of constant impedance type. For the model from Fig. 2.5, the following matrix equation holds:

$$\begin{bmatrix} \boldsymbol{I_G} \\ \mathbf{0} \end{bmatrix} = \begin{bmatrix} \mathbf{Y_A} & \mathbf{Y_B} \\ \mathbf{Y_C} & \mathbf{Y_D} \end{bmatrix} \begin{bmatrix} \boldsymbol{E'} \\ \boldsymbol{U} \end{bmatrix} \quad \text{where} \tag{2.20}$$

- $\boldsymbol{I_G} = \begin{bmatrix} \bar{I}_{g1} & \bar{I}_{g2} & \dots & \bar{I}_{gn} \end{bmatrix}^T$ - stands for the vector of the generators currents and $\mathbf{0}$ denotes $(N \times 1)$-dimensional zero vector;
- $\boldsymbol{E'} = \begin{bmatrix} \bar{E}'_1 & \bar{E}'_2 & \dots & \bar{E}'_n \end{bmatrix}^T$ - is the vector of the generators internal voltages;
- $\boldsymbol{U} = \begin{bmatrix} \bar{U}_1 & \bar{U}_2 & \dots & \bar{U}_N \end{bmatrix}^T$ - is the vector of voltages at both generators terminal buses and pure load buses;
- $\mathbf{Y_A}$ - represents the $(n \times n)$-diagonal matrix where diagonal $(k,k)^{th}$ entrances ($k = 1, ..., n$) are defined as $\bar{Y}_{A_{kk}} = 1/jX'_{dk}$;
- $\mathbf{Y_B}$ - is a matrix of $(n \times N)$ dimensions in which the only non-zero elements $\bar{Y}_{B_{kk}} = -1/jX'_{dk}$ are at $(k,k)^{th}$ positions ($k = 1, ..., n$);
- $\mathbf{Y_C} = \mathbf{Y_B^T}$ and;
- $\mathbf{Y_D}$ - is an $(N \times N)$ matrix that essentially represents $\mathbf{Y'_{BUS}}$ whose elements are expanded for the corresponding entrances of $\mathbf{Y_A}$.

Starting from the compact form of Eq. (2.20), by substitution it can be shown that:

$$\begin{aligned} \boldsymbol{I_G} &= (\mathbf{Y_A} - \mathbf{Y_B}\mathbf{Y_D}^{-1}\mathbf{Y_C})\boldsymbol{E'} \\ \boldsymbol{I_G} &= \mathbf{Y_{RNM}}\boldsymbol{E'}, \end{aligned} \tag{2.21}$$

where $\mathbf{Y_{RNM}}$ is the RNM admittance matrix of $(n \times n)$ dimensions. In the following notation, the non-diagonal $(k,p)^{th}$ entrance of $\mathbf{Y_{RNM}}$ is $\bar{Y}_{RNM_{kp}} = G_{kp} + jB_{kp}$ and the diagonal elements are $\bar{Y}_{RNM_{kk}} = G_{kk} + jB_{kk}$. The current of the k^{th}

generator in the rotor reference frame ($\bar{I}_{gk} = (I_{qk} + jI_{dk})e^{j\delta_k}$) can then easily be expressed from Eq. (2.21) in the following form:

$$\bar{I}_{gk} = (G_{kk} + jB_{kk})E'_k e^{j\delta_k} + \sum_{\substack{p=1 \\ p\neq k}}^{n} (G_{kp} + jB_{kp})E'_p e^{j\delta_p} \tag{2.22}$$

from which I_{qk} and I_{dk} components of $\bar{I}_{gk}$ can be solved as:

$$\begin{aligned} I_{qk} &= G_{kk}E'_k + \sum_{\substack{p=1 \\ p\neq k}}^{n} E'_p\Big(G_{kp}\cos(\delta_k - \delta_p) + B_{kp}\sin(\delta_k - \delta_p)\Big) \quad \text{and} \\ I_{dk} &= B_{kk}E'_k + \sum_{\substack{p=1 \\ p\neq k}}^{n} E'_p\Big(B_{kp}\cos(\delta_k - \delta_p) - G_{kp}\sin(\delta_k - \delta_p)\Big). \end{aligned} \tag{2.23}$$

By the virtue of Eqs. (2.3), (2.4), (2.22) and (2.23), the dynamical equations for RNM with n generators ($k = 1, ..., n$) can now be defined:

$$\begin{aligned} \dot{\delta}_k &= \omega_k; \\ \dot{\omega}_k &= \frac{1}{M_k}(P_{mk} - P_{ek} - D_k\omega_k), \quad \text{where} \\ P_{ek} &= E'_k I_{qk} = G_{kk}E'^2_k + \sum_{\substack{p=1 \\ p\neq k}}^{n} E'_k E'_p\Big(G_{kp}\cos(\delta_{kp}) + B_{kp}\sin(\delta_{kp})\Big) \end{aligned} \tag{2.24}$$

and $\delta_{kp} = \delta_k - \delta_p$. The above given equations completely describe the dynamic behaviour of a power system in ODE form:

$$\dot{\boldsymbol{x}} \;\; = \boldsymbol{f}(\boldsymbol{x}). \tag{2.25}$$

By describing the system with the first order differential equations, it is sufficient to follow up the behaviour of the state variables when carrying out short-term RAS. The vector of state variables is the same as in the case of DAE model from Eq. (2.17), i.e. state variables are rotor angles and generator angle speeds:

$$\boldsymbol{x} \;\; = \Big[\delta_1 \quad \delta_2 \quad \dots \quad \delta_n \quad \omega_1 \quad \omega_2 \quad \dots \quad \omega_n\Big]^T. \tag{2.26}$$

In this manner, only internal generator buses are retained and there is no need to solve the algebraic set of equations. After having SPM and RNM of power system defined, the subsequent text will briefly review some of the existing methodologies for transient stability assessment.

2.4 TDS in RAS analysis

Time Domain Simulation (TDS) is the most accurate method that is used for the purpose of dynamic stability analysis. It offers wide modeling opportunities that, on the other hand, introduce corresponding computational burden. In dynamics of small disturbances, TDS can be successfully replaced by analytical techniques that can be applied if the DAE system from (2.1) is linearized around a stable equilibrium $(\boldsymbol{x_0}, \boldsymbol{y_0})$. Linearized power system models provide reliable information about stability only locally, i. e. close to an equilibrium. For larger excursions of state/algebraic variables, some non-linear analysis tool (e.g. TDS) should be employed instead. After a large disturbance occurs, the automatic actions of protective system may also lead to configurational changes. As a consequence of a fault (large disturbance), the power system goes through the following stages: (i) the pre-fault stage that corresponds to the steady state, (ii) fault-on stage and (iii) the post-fault period in which the fault has been cleared. If the time when a disturbance occurs is denoted by t_f and the time of fault clearing is t_{cl}, the SPM of a power system that is described by a set of Differential Algebraic Equations (DAE) (2.1) may be divided into three stages (pre-fault (pre), fault-on (f) and post-fault ($post$)):

$$\dot{\boldsymbol{x}} = \boldsymbol{f_{pre}}(\boldsymbol{x}, \boldsymbol{y}); \qquad 0 = \boldsymbol{g_{pre}}(\boldsymbol{x}, \boldsymbol{y}); \qquad 0 \leq t < t_f, \tag{2.27}$$

$$\dot{\boldsymbol{x}} = \boldsymbol{f_f}(\boldsymbol{x}, \boldsymbol{y}); \qquad 0 = \boldsymbol{g_f}(\boldsymbol{x}, \boldsymbol{y}); \qquad t_f \leq t < t_{cl}, \tag{2.28}$$

$$\dot{\boldsymbol{x}} = \boldsymbol{f_{post}}(\boldsymbol{x}, \boldsymbol{y}); \qquad 0 = \boldsymbol{g_{post}}(\boldsymbol{x}, \boldsymbol{y}); \qquad t_{cl} \leq t < \infty. \tag{2.29}$$

The principle of TDS is to examine the system behaviour by solving Eq. (2.27), (2.28) and (2.29), for a certain number (n_{st}) of time steps Δt. The result of TDS is a discrete array of solutions at each time step r ($r = 1, ..., n_{st}$), both for the states ($\boldsymbol{x}^r$) and the algebraic ($\boldsymbol{y}^r$) variables. The state and network solutions are typically obtained by using one of the two common approaches, namely:

- **Partitioned solution method** [96] where the differential and algebraic equations are solved separately (there is a delay between solutions). The solution of the algebraic equations $\boldsymbol{y}^r$ at time step r is used to initiate the solution ($\boldsymbol{x}^{r+1}$) in the subsequent time step ($r + 1$). The vector of state variables ($\boldsymbol{x}^{r+1}$) is further found by any explicit integration technique, e.g. Euler method, modified Euler (predictor-corrector) method and the family of Runge-Kutta (RK) methods (e.g. of second, fourth order and modified methods) [54, 97].

- **Simultaneous solution strategy** [98] refers to the solution algorithm where both the state ($\boldsymbol{x}^r$) and algebraic ($\boldsymbol{y}^r$) variables are solved simultaneously in

r^{th} time step. General practice is to obtain the solution ($\boldsymbol{x}^r$,$\boldsymbol{y}^r$) by the means of Newton's method [99] from a set of non-linear equations. A formula for implicit integration has to be used to transform the differential equations into algebraic ones. This solution technique is applied for stiff problems, i.e. for wide ranges of time scales of differential equations.

Both approaches share the same criterion for short-term RAS. One TDS is carried out for each clearing time (t_{cl}). The clearing time is increased in discrete steps until the TDS in which rotor angles swing out of step. The clearing time of the simulation preceding the unstable one is then proclaimed as the Critical Clearing Time (CCT) t_{cc}. Since the framework of this thesis is short-term stability, the timescale is the same for both voltage and RAS issues. In this case, a partitioned solution approach will suffice for the explicit integration of differential equations in both SPM (2.17) or RNM (2.25). The examples of the effective explicit solvers that belong to RK and Euler classes of methods follow.

2.4.1 Explicit RK methods

In the family of explicit RK methods, the idea was to employ approximated Taylor series to solve x^{r+1} at $t_{r+1} = t_r + \Delta t$ (which corresponds to $(r+1)^{th}$ time step). The simplification compared to Taylor series is that the effect of the derivatives of higher order are taken into account by evaluating the first derivative several times. Depending on the number of these evaluations, various RK methods have been introduced. Starting from the solution x^r at time t_r in r^{th} time step and for a certain number of stages q, the general idea is to solve x^{r+1} by formula:

$$x^{r+1} \quad = x^r + \Delta x^r = x^r + \Delta t \sum_{s=1}^{q} b_s k_s \tag{2.30}$$

where the coefficients k_s ($s = 1, ..., q$) are defined as:

$$\begin{aligned}
k_1 &= f(t_r, x_r) \\
k_2 &= f(t_r + c_2\Delta t, x_r + a_{21}k_1\Delta t) \\
k_3 &= f(t_r + c_3\Delta t, x_r + (a_{31}k_1 + a_{32}k_2)\Delta t) \\
k_4 &= f(t_r + c_4\Delta t, x_r + (a_{41}k_1 + a_{42}k_2 + a_{43}k_3)\Delta t) \\
&\vdots \\
k_q &= f(t_r + c_q\Delta t, x_r + (a_{q1}k_1 + a_{q2}k_2 + \cdots + a_{q(q-1)}k_{q-1})\Delta t).
\end{aligned} \tag{2.31}$$

The product of weights (b_s) and estimated slopes ($k_s\Delta t$) are summed up for $s = 1, ..., q$ in order to obtain the incremental change Δx^r. To have a good x^{r+1} solution,

it also needs to hold that $\sum_{j=1}^{s-1} a_{sj} = c_s$, for $s = 2, ..., q$. Researchers have developed different RK methods [100] with specified orders (n_{ord}), and in those cases certain requirements regarding local truncation error [101] are to be fulfilled. These requirements affect the total number of stages (q) with respect to coefficients c_s, a_{sj} (when $s = 2, ..., q$, $j = 1, ..., s-1$) and b_s (for $s = 1, ..., q$). The usual practice is to arrange the coefficient data in so-called Butcher tableau [102]:

$$\begin{array}{c|ccccc} 0 & & & & & \\ c_2 & a_{21} & & & & \\ c_3 & a_{31} & a_{32} & & & \\ \vdots & \vdots & & \ddots & & \\ c_q & a_{q1} & a_{q2} & \dots & a_{q(q-1)} & \\ \hline & b_1 & b_2 & \dots & b_{q-1} & b_q \end{array} . \tag{2.32}$$

This thesis will carry out the integration of differential equations by the means of Dormand-Prince [103] method that is often used in short-term RAS analysis. Dormand-Prince method is one of the embedded RK methods that can adapt its step size in order to control local truncation error. This is implemented by combining the method of order n_{ord} and the method of order $(n_{ord} - 1)$ in each time step r ($r = 1, ..., n_{st}$). The method of the order $(n_{ord} - 1)$ shares all the coefficients with the higher order one, except for the b_s ($s = 1, ..., q$), i.e. the solution of the additional method at the $(r+1)^{th}$ time step is:

$$x_*^{r+1} = x^r + \Delta x_*^r = x^r + \Delta t \sum_{s=1}^{q} b_s^* k_s. \tag{2.33}$$

By deducting the lower order estimate from the higher order one, the error $E_{rr}^{r+1} = x^{r+1} - x_*^{r+1}$ is observed to adjust the step size. The Butcher tableau for embedded RK solvers is then extended for the coefficients b_s^* ($s = 1, ..., q$) as:

$$\begin{array}{c|ccccc} 0 & & & & & \\ c_2 & a_{21} & & & & \\ c_3 & a_{31} & a_{32} & & & \\ \vdots & \vdots & & \ddots & & \\ c_q & a_{q1} & a_{q2} & \dots & a_{q(q-1)} & \\ \hline & b_1 & b_2 & \dots & b_{q-1} & b_q \\ & b_1^* & b_2^* & \dots & b_{q-1}^* & b_q^* \end{array} . \tag{2.34}$$

For the specific case of Dormand-Prince method, there are seven stages ($q = 7$), where stage q in step r corresponds to stage 1 of step $r + 1$ (six evaluations of functions are made). In this case, the coefficients from Butcher tableau have the following values:

$$
\begin{array}{c|ccccccc}
0 & & & & & & & \\
\frac{1}{5} & \frac{1}{5} & & & & & & \\
\frac{3}{10} & \frac{3}{40} & \frac{9}{40} & & & & & \\
\frac{4}{5} & \frac{44}{45} & -\frac{56}{15} & \frac{32}{9} & & & & \\
\frac{8}{9} & \frac{19372}{6561} & -\frac{25360}{2187} & \frac{64448}{6561} & -\frac{212}{729} & & & \\
1 & \frac{9017}{3168} & -\frac{355}{33} & \frac{46732}{5247} & \frac{49}{176} & -\frac{5103}{18656} & & \\
1 & \frac{35}{384} & 0 & \frac{500}{1113} & \frac{125}{192} & -\frac{2187}{6784} & \frac{11}{84} & \\
\hline
 & \frac{35}{384} & 0 & \frac{500}{1113} & \frac{125}{192} & -\frac{2187}{6784} & \frac{11}{84} & 0 \\
 & \frac{5179}{57600} & 0 & \frac{7571}{16695} & \frac{393}{640} & -\frac{92097}{339200} & \frac{187}{2100} & \frac{1}{40}
\end{array}
\quad , \tag{2.35}
$$

where the last row provides the coefficients for the 4^{th} order solution, and the previous row corresponds to the estimate with the 5^{th} order of accuracy. The coefficients are chosen such that the error of the 5^{th} order solution is minimized. The Dormand-Prince method will be used for TDS integration in the studies that concern RAS. This method will be paired with the trust-region Dogleg algorithm that will solve the algebraic part of DAE model from (2.27)-(2.29). The Dogleg [104] algorithm is a combination of Steepest Descent [105] and Newton-Raphson [106] solvers for systems of non-linear algebraic equations.

2.4.2 Modified Euler Method

Modified Euler [54] is another commonly employed method of explicit integration in non-stiff dynamical systems. It belongs to the class of predictor-corrector methods [107] since it involves the two corresponding steps:

- **Predictor step** which is identical to the standard Euler method that estimates the solution at $(r+1)^{th}$ time step by using the first derivative (slope) at the beginning of the step to account for the Δx^r:

$$x_p^{r+1} = x^r + \Delta x^r = x^r + \left.\frac{dx}{dt}\right|_{x=x^r} \cdot \Delta t = x^r + f(x^r)\Delta t. \tag{2.36}$$

  The difference compared to the standard Euler method is that this step is used only to predict the value at the end of the step (i.e. this is not considered as the final solution in the given step).

- **Corrector step** adjusts the incremental change by taking the average of the derivatives at the beginning and at the end of the step $(r+1)$. The derivative at the end of the step is found based on the predicted value x_p^{r+1}. The corrected solution can then be given by:

$$\begin{aligned} x_c^{r+1} = x^r + \Delta x_c^r &= x^r + \left(\left.\frac{dx}{dt}\right|_{x=x^r} + \left.\frac{dx}{dt}\right|_{x=x_p^{r+1}} \right) \frac{\Delta t}{2} \\ &= x^r + (f(x^r) + f(x_p^{r+1}))\frac{\Delta t}{2}. \end{aligned} \tag{2.37}$$

In this thesis, predictor-corrector Euler will be implemented for solving differential equations in the studies that relate to voltage collapse and Voltage Impasse Regions (VIR). The idea is to continue the integration by the means of TDS even the solution of algebraic equations fails to converge.

2.5 Short-term RAS as a stability region problem

Although TDS is the most reliable tool when it comes to the analysis of large disturbances, it is time consuming. In the process of CCT identification, many TDS have to be carried out and a large portion of computational time is consumed by the post-fault dynamics. A popular alternative to TDS is the class of approaches that are known as Direct Methods. They are also referred to as Transient Energy Function (TEF) methods. The idea to replace the numerical integration of a post-fault dynamical system with a unique stability criterion started to develop in the 40's [65] and was conceptually pursued until the 60's [66–68]. These findings have further served as the basin of Direct Methods.

2.5.1 Characterization of the stability region

In Direct Methods, the short-term RAS is observed as a stability region problem of a Stable Equilibrium Point (SEP). For a general, non-linear system of differential equations:

$$\dot{\boldsymbol{x}} = \boldsymbol{f}(\boldsymbol{x}), \tag{2.38}$$

equilibrium points $\boldsymbol{x_i}$ are found by setting the time derivative on the left-hand side to zero (i.e. $\mathbf{0} = \boldsymbol{f}(\boldsymbol{x})$). Direct methods deal with hyperbolic equilibrium points, which means that the Jacobian of $\boldsymbol{f}(\boldsymbol{x})$ at the given equilibrium point $\boldsymbol{x_i}$ has no eigenvalues with zero real parts. Those equilibria that have one eigenvalue with positive real part are known as type-1 Unstable Equilibrium Points (UEPs), and those with any higher number (z) of eigenvalues in the right half plane are referred to as type-z equilibrium points. The theory that concerns direct methods is mostly interested in type-1 UEPs. The Stable Equilibrium Point (SEP) $\boldsymbol{x_s}$ has all its eigenvalues in the left half plane. Both SEP and UEPs may change if configurational changes occur in relation to a fault, as described in the model (2.27)-(2.29). Therefore, in the further notation, $\boldsymbol{x_s^{post}}$ will denote the SEP of a post-fault system and a type-1 UEP of the same system will be given as $\boldsymbol{x_{ui}}$. The post-fault stability region $A(\boldsymbol{x_s^{post}})$ of SEP $\boldsymbol{x_s^{post}}$ can now be defined as an open, invariant and connected subset of the state-space from which all the trajectories will converge to SEP $\boldsymbol{x_s^{post}}$ [108]:

$$A(\boldsymbol{x_s^{post}}) = \left\{\boldsymbol{x} | \boldsymbol{x}(t) \underset{t\to\infty}{=} \boldsymbol{x_s^{post}}\right\}. \tag{2.39}$$

Equation (2.39) is identical to the definition of the stable manifold of $\boldsymbol{x_s^{post}}$. Hence, in a similar fashion, stable (W^s) and unstable (W^u) manifolds of a type-1 UEP $\boldsymbol{x_{ui}}$ may be defined as invariant sets:

$$\begin{aligned} W^s(\boldsymbol{x_{ui}}) &= \left\{\boldsymbol{x} | \boldsymbol{x}(t) \to \boldsymbol{x_{ui}} \quad \text{as} \quad t \to \infty\right\}; \\ W^u(\boldsymbol{x_{ui}}) &= \left\{\boldsymbol{x} | \boldsymbol{x}(t) \to \boldsymbol{x_{ui}} \quad \text{as} \quad t \to -\infty\right\}. \end{aligned} \tag{2.40}$$

The following assumptions regarding vector fields need to hold to define the boundary of the stability region in the terms of the previously defined concepts [95, 109]:

1. The UEPs of (2.38) that are located on the stability boundary $\partial A(\boldsymbol{x_s^{post}})$ are hyperbolic.

2. The transversality condition of stable and unstable manifolds of UEPs is valid for all the equilibrium points on the boundary $\partial A(\boldsymbol{x_s^{post}})$.

3. Every trajectory $\boldsymbol{x}(t)$ on the stability boundary $\partial A(\boldsymbol{x}_s^{post})$ will converge to one of the UEPs that are located at the boundary as $t \to \infty$. This is not a generic property of all non-linear dynamical systems, however, it can be guaranteed if the existence of an energy-like function $V(\boldsymbol{x})$ can be demonstrated for the post-fault system. If the number of state variables is here temporarily denoted by n, the suitable $\mathbb{R}^n \to \mathbb{R}$ function $V(\boldsymbol{x})$ exists if it is continuously differentiable (C^1) and:

   C1. $\dot{V}(\boldsymbol{x}) \leq 0$ is valid for all the points in state-space that are not equilibria.

   C2. The set in state space described by $\dot{V}(\boldsymbol{x}) = 0$ has zero measure if $\boldsymbol{x}$ is not an equilibrium point.

   C3. If $V(\boldsymbol{x})$ is bounded $\implies$ $\boldsymbol{x}(t)$ is bounded.

The boundary of the stability region of a post-fault SEP $\boldsymbol{x}_s^{post}$ then equals to the union of closure of the stable manifolds of type-1 UEPs that are placed on the stability boundary $\partial A(\boldsymbol{x}_s^{post})$ [69]:

$$\partial A(\boldsymbol{x}_s^{post}) = \bigcup_i \overline{W^s}(\boldsymbol{x}_{ui}). \tag{2.41}$$

The region of attraction and its features are illustrated in Fig. 2.6 for an autonomous dynamical system that has two state variables (x_1 and x_2).

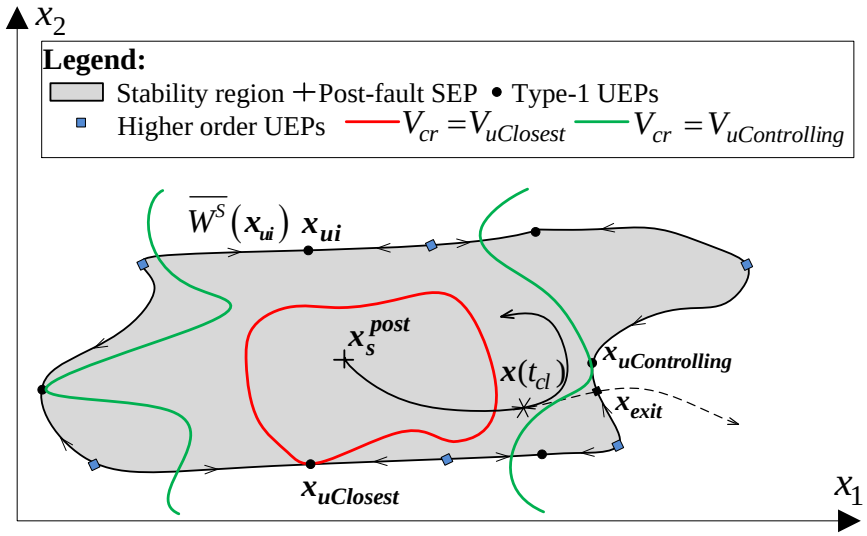

Figure 2.6: Two-dimensional state-space representation of a stability region

2.5.2 Direct methods

From the viewpoint of the stability region $A(\boldsymbol{x}_s^{post})$ from (2.39), a system will be considered transiently stable if at the time when a fault is cleared (t_{cl}), the point on the trajectory $\boldsymbol{x}(t_{cl})$ is inside the region of attraction. Direct methods [110] assess the state-space location by the means of stability index $V(\boldsymbol{x})$ that is actually an energy-like Lyapunov function. In physical systems, Lyapunov functions are scalar functions that are usually generalized from the idea of energy of a dynamical system [111]. The same follows for power systems. The measure of energy $V(\boldsymbol{x}_s^{post})$ is zero, and its derivative is negative semidefinite inside the stability region $A(\boldsymbol{x}_s^{post})$. The advantages of direct methods are that (i) they replace the demanding post-fault integration of TDS by a stability criterion and that (ii) they give stability margins. The aim of this and remaining subsections of this chapter is to provide a general discussion on direct methods.

To show a simple example of an energy function, let us consider the RNM model (2.24) with n generators and an additional $(n+1)^{th}$ reference bus that has a very large inertia ($\delta_{n+1} = 0,\ \dot{\omega}_{n+1} = 0$). If transfer conductances of RNM admittance matrix are neglected, the model (2.24)/(2.25) may be written as:

$$\begin{aligned}
&\dot{\delta}_k = \omega_k; \\
&\dot{\omega}_k = \frac{1}{M_k}\left(P_k^{eq} - \sum_{\substack{p=1 \\ p\neq k}}^{n+1} E'_k E'_p B_{kp} \sin(\delta_k - \delta_p) - D_k \omega_k\right), \text{ for } k = 1, ..., n,
\end{aligned} \tag{2.42}$$

where $P_k^{eq} = P_{mk} - G_{kk}E_k'^2$. Clearly, some portion of the active load is lost by neglecting the transfer conductances for a system with purely reactive transmission network. By looking back to Eq. (2.21), it may be noticed that the effect of load is distributed between diagonal and non-diagonal elements of $\mathbf{Y_{RNM}}$. Hence, disregarded transfer conductances would probably decrease the accuracy of RAS assessment. However, the assumption to neglect G_{kp} in RNM enables an exact and simple construction of an energy function. This is sufficiently good in the context of a thesis which briefly revises direct methods for the purpose of conceptual discussion. More sophisticated energy functions may be found in [69, 112].

The SEP of the system (2.42) is $\boldsymbol{x}_s^{post} = (\boldsymbol{\delta}_s^{post}, \mathbf{0})$, where $\mathbf{0} = \boldsymbol{\omega}_s^{post}$ denotes $(n \times 1)$-dimensional zero vector of angle speeds relative to infinite bus reference and the vector of rotor angles is:

$$\boldsymbol{\delta}_s^{post} = \begin{bmatrix} \delta_{1s}^{post} & \delta_{2s}^{post} & \dots & \delta_{ns}^{post} \end{bmatrix}^T. \tag{2.43}$$

Then, for the system from Eq. (2.42), a well-defined Lyapunov function [95]:

$$\begin{aligned} V(\boldsymbol{\delta},\boldsymbol{\omega}) &= \frac{1}{2}\sum_{k=1}^{n} M_k\omega_k^2 - \sum_{k=1}^{n} P_k^{eq}(\delta_k - \delta_{ks}^{post}) \\ &- \sum_{k=1}^{n}\sum_{p=k+1}^{n+1} E_k' E_p' B_{kp}\Big(\cos(\delta_k-\delta_p) - \cos(\delta_{ks}^{post} - \delta_{ps}^{post})\Big) \\ &= V_K(\boldsymbol{\omega}) + V_p(\boldsymbol{\delta}) \end{aligned} \tag{2.44}$$

exists if all $D_k = 0$. The function (2.44) can be interpreted as the summation of the kinetic energy of rotating masses ($V_K(\boldsymbol{\omega})$) and the remaining, angle dependent part—accumulated potential energy ($V_p(\boldsymbol{\delta})$). Let the functions:

$$u_k = \sum_{\substack{p=1\\p\neq k}}^{n+1} E_k' E_p' B_{kp}\sin(\delta_k - \delta_p), \text{ for } k = 1,...,n, \tag{2.45}$$

be the entrances of the vector-function $\boldsymbol{u}$. In the cases when some $D_k \neq 0$, it is assumed that the Jacobian matrix $d\boldsymbol{u}/d\boldsymbol{\delta}$ is non-singular at the equilibrium points. By finding the derivative of $V(\boldsymbol{\delta}(t),\boldsymbol{\omega}(t))$ along the trajectory $(\boldsymbol{\delta}(t),\boldsymbol{\omega}(t))$:

$$\dot{V}(\boldsymbol{\delta}(t),\boldsymbol{\omega}(t)) = \sum_{k=1}^{n}\left(\frac{dV}{d\delta_k}\dot{\delta}_k + \frac{dV}{d\omega_k}\dot{\omega}_k\right) = -\sum_{k=1}^{n} D_k\omega_k^2, \tag{2.46}$$

it becomes clear that $\dot{V}(\boldsymbol{\delta}(t),\boldsymbol{\omega}(t)) = 0$ holds only for $\boldsymbol{\omega} = 0$ which corresponds to equilibrium points. Due to $D_k > 0$, in all other cases the derivative $\dot{V}(\boldsymbol{\delta}(t),\boldsymbol{\omega}(t))$ is strictly negative. Hence, the conditions C1-C2 from the previous subsection are fulfilled for C^1 function (2.44). From the known proof about the boundedness of the trajectory $(\boldsymbol{\delta}(t),\boldsymbol{\omega}(t))$ from [110] (which relates to the same model of the generator and the same energy function), it may be concluded that $V(\boldsymbol{\delta},\boldsymbol{\omega})$ from (2.44) also satisfies the condition C3.

In the framework of direct methods, the RAS criterion is that the energy at the time of fault clearing is less than some critical energy ($V(t_{cl}) < V_{cr}$). If this condition is satisfied, it is expected that the system will not leave the stability region $A(\boldsymbol{x_s^{post}})$ which is equal to the system being transiently (first-swing) stable. Finding critical energy V_{cr} is essential step to apply the energy function theory instead of classical TDS. In the past, various approaches have been developed in order to calculate critical energy as accurately as possible. A short description of the most utilized approaches for V_{cr} calculation is given in the sequel.

2.5.3 UEP-oriented assessment

From the theoretical concepts presented in Subsection 2.5.1, various UEP-oriented methods have been developed in order to approximate the stability boundary $\partial A(\boldsymbol{x_s^{post}})$. The idea of UEP-oriented methods is to use constant energy surface $V_{cr} = V_{ui}$ passing through a relevant (i^{th}) type-1 UEP that lies on the stability boundary. The energy of a relevant UEP is further used as a critical energy instead of the energy of trajectory's exit point. The exit point is difficult to detect, however, a trajectory exits the boundary at one of the stable manifolds $W^s(\boldsymbol{x_{ui}})$ of type-1 UEPs. All the trajectories that start on one of manifolds $W^s(\boldsymbol{x_{ui}})$ would converge to $\boldsymbol{x_{ui}}$ as $t \to \infty$. Therefrom originated the idea of using the energy of type-1 UEPs since they are easier to detect than exit points. The two approaches stand out [69]:

- **Closest UEP method** [69] approximates the stability boundary by the equipotential curve $V_{cr} = V_{uClosest}$ (shown by red colour in Fig. 2.6). The method consists of the following steps:

  1. It is first necessary to find all type-1 UEPs and determine which of them are located on the stability boundary. This step practically checks if the unstable manifolds of type-1 UEPs converge to SEP by integration in ϵ-neighborhood of type-1 UEPs.
  2. The selected UEPs are ordered according to the energy value. The type-1 UEP with the lowest energy is Closest UEP ($\boldsymbol{x_{uClosest}}$) and its energy is proclaimed as the critical one ($V(\boldsymbol{x_{uClosest}}) = V_{uClosest} = V_{cr}$).
  3. Stability check is further carried out by comparing the values of energy at fault clearing $V(\boldsymbol{x}(t_{cl}))$ with the critical energy $V_{uClosest}$.

  The Closest UEP method is simple, however, it has an obvious drawback. The method is conservative, i.e. the point where a trajectory crosses the stability boundary ($\boldsymbol{x_{exit}}$) may not belong to the unstable manifold of the Closest UEP (as illustrated in Fig. 2.6). The consequence for short-term RAS is an energy margin estimate that is much smaller than the one obtained from TDS.

- **Controlling UEP method** takes into account the direction of a post-fault trajectory to avoid drawbacks in Closest UEP approach. The Controlling UEP ($\boldsymbol{x_{uControlling}}$) is the type-1 UEP on the stability boundary $\partial A(\boldsymbol{x_s^{post}})$ whose stable manifold $W^s(\boldsymbol{x_{uControlling}})$ contains exit point ($\boldsymbol{x_{exit}}$). In Fig. 2.6, the critical energy $V(\boldsymbol{x_{uControlling}}) = V_{uControlling} = V_{cr}$ corresponds to the green equipotential curve. The general algorithm of this method is comparatively more complicated than the Closest UEP approach:

1. All the stable manifolds of type-1 UEPs on the boundary need to be derived.
2. The Controlling UEP ($\boldsymbol{x}_{uControlling}$) is identified as the type-1 UEP whose closure of stable manifold $W^s(\boldsymbol{x}_{uControlling})$ is crossed first by a post-fault trajectory.

To implement the given steps is not trivial. Some proposed methods employ tangent hyperplanes [113], however, the theoretically most robust is so-called Boundary of stability region Controlling Unstable equilibrium (BCU) method [71]. Although BCU is fast, divergence issues and problems regarding exit point detection can occur.

A common drawback of UEP-oriented method comes from the fact that UEPs are not static entities. Varying operating conditions do not cause only changes in the stability region. It has been shown that UEPs also change their positions on the boundary, and that they may collide and disappear [73].

2.5.4 PEBS

Potential Energy Boundary Surface (PEBS) method [114] has been introduced in order to avoid challenging identification of UEP of interest. PEBS observes the stability region problem in the subspace of rotor angles where it provides an estimate of an exit point. From the definition of $V_p(\boldsymbol{\delta})$ in Eq. (2.44), the model (2.42) can be reformulated as:

$$\begin{aligned} \dot{\delta}_k &= \omega_k; \\ \dot{\omega}_k &= \frac{1}{M_k}\Big(- \frac{\partial V_p(\boldsymbol{\delta})}{\partial \delta_k} - D_k\omega_k \Big), \text{ for } k = 1, ..., n, \end{aligned} \tag{2.47}$$

where the model (2.47) retains the same energy function that is provided by Eq. (2.44). The motivation for this approach comes from the fact that both the SEP $\boldsymbol{x}_{\boldsymbol{s}}^{\boldsymbol{post}} = (\boldsymbol{\delta}_{\boldsymbol{s}}^{\boldsymbol{post}}, \mathbf{0})$ and all UEPs $\boldsymbol{x}_{\boldsymbol{ui}}^{\boldsymbol{post}} = (\boldsymbol{\delta}_{\boldsymbol{ui}}^{\boldsymbol{post}}, \mathbf{0})$ are located in the subspace of rotor angles ($\mathbf{0} = \boldsymbol{\omega}_{\boldsymbol{s}}^{\boldsymbol{post}} = \boldsymbol{\omega}_{\boldsymbol{ui}}^{\boldsymbol{post}}$). Hence, it is enough to study the associated gradient system [114]:

$$\dot{\delta}_k = -\frac{\partial V_p(\boldsymbol{\delta})}{\partial \delta_k}, \text{ for } k = 1, ..., n, \tag{2.48}$$

and determine its stability boundary which equals to PEBS. Assuming that the fault-on trajectories are orthogonal to PEBS [115], the potential energy at the point

of PEBS crossing ($\boldsymbol{\delta_{PEBS}}$) may with good accuracy be taken as the critical one ($V_p(\boldsymbol{\delta_{PEBS}}) = V_{PEBS} = V_{cr}$). In order to find CCT, it is sufficient to carry out two simple numerical steps (as depicted in Fig. 2.7):

1. The first maximum of $V_p(\boldsymbol{\delta}(t^*)$ should be identified along a fault-on trajectory at some time t^*. This maximum is considered as the critical energy, i.e.:

$$V_p(\boldsymbol{\delta}(t^*) = V_p(\boldsymbol{\delta_{PEBS}}) = V_{PEBS} = V_{cr}. \tag{2.49}$$

2. The critical clearing time t_{cc} is then found along the trajectory of the original system (2.42) where: $V_K(\boldsymbol{\omega}(t_{cc})) + V_p(\boldsymbol{\delta}(t_{cc})) = V_{cr}$. This means that, at the time of fault clearing, $V(\boldsymbol{\delta}, \boldsymbol{\omega}) \leq V_p(\boldsymbol{\delta_{PEBS}})$ needs to hold to achieve RAS.

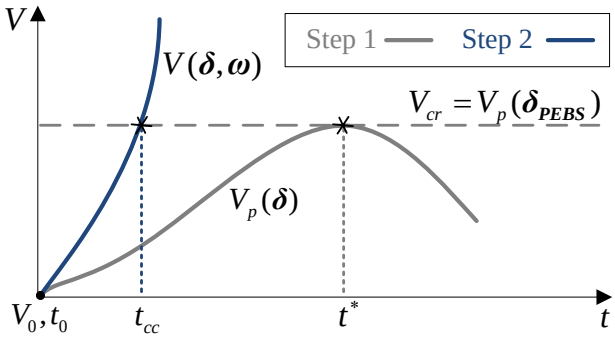

Figure 2.7: Graphical description of PEBS method

PEBS is a very convenient method since it takes into account a direction of a trajectory without having to calculate UEPs. Nevertheless, PEBS method only works with the projection of the stability boundary on angle space that does not account for the kinetic energy of an exit point. If the location of an exit point along the stable manifold of type-1 UEP is relativly close to UEP itself ($\boldsymbol{\omega_{exit}} \approx 0$), PEBS method performs well. However, it can also happen that an exit point is far enough from UEP to have sufficiently high kinetic energy, which consequently affects the method's accuracy.

Now that the theoretical basis is provided, the following chapters will propose certain solutions/explanations that are of importance for short-term stability analysis.

Chapter 3

Assessment of RAS in Parameter Space

The following chapter presents the conceptual idea and analytical foundation of a new methodology for short-term RAS assessment. The proposed methodology observes RAS as a security region problem in the space of parameters that are of importance for RAS analysis. The approach constructs parameter-space security boundaries in analytical (polynomial) form.

The DSA assessment of short-term RAS consists of large number of tests that investigate how a power system handles critical contingencies. Each of these tests corresponds to a certain pre-fault and post-fault operating state. Since the electromechanical transients occur rather fast [35], the extensive RAS analysis has to be carried out in advance. The previously explained approaches (TDS and direct methods) can be used as tools to determine the severity of a disturbance. The off-line analysis of transient stability usually involves identification of some sort of stability index/margin (CCT, energy or transmitted power, for instance) for each contingency and operating point. However, if a current operating condition for some reason does not belong to a set of pre-checked operating points, the stability margin and the risk of dynamic instability are unknown to TSO. Hence, there is a necessity to develop faster and sufficiently accurate methods for short-term RAS in parameter-space. PRM have attempted to solve this issue by the means of machine learning [80–82]. Among other drawbacks, ANN are trained to provide one-directional information which means that the functional relationship between an input and an output does not have an analytical form. To find a function that relates parameters and the measure of stability is another task of the proposed methodology.

The sections of this chapter will first illustrate the effect that changes of an operating point have on RAS region and the measure of stability. Then a data acquisition method is chosen and a method algorithm is proposed. This chapter deals with Stage 1 of the proposed algorithm, i.e. it explains (i) the idea of parametrization of the stability boundary, (ii) the tools of the parametrization and (iii) the polynomial model for the construction of security boundaries.

3.1 Illustrative example

Before proposing a new methodology, this section will outline the importance of understanding how a change in operating conditions may affect short-term RAS and stability region characteristics. The aim is to illustrate a perturbation of an equilibrium point from both TDS and direct methods point of view and also to compare the performance of the two approaches.

3.1.1 Test system

The simple two-machine infinite-bus system from Fig. 3.1 is employed in the study. The generators are represented by the classical model [54] and the lines are given in Π form [93] where shunt admittances are not depicted for simplicity. Series resistances are neglected. Additionally, loads are set to zero such that all power generation is being absorbed by the infinite bus with constant voltage $\bar{U}_3 = 1\angle 0$. In the terms of RNM model from (2.42), this means that beside transfer conductances being zero, it also holds that $G_{11} = G_{22} = 0$.

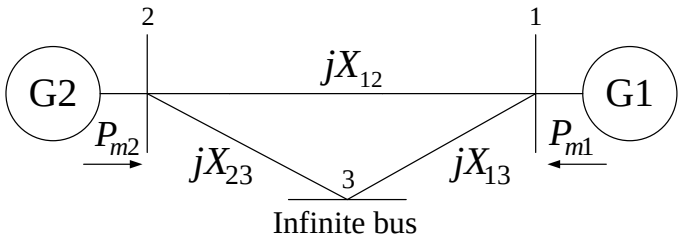

Figure 3.1: Two-machine infinite-bus test system

Having an infinite bus in the system, it is a logical choice to take this 3^{rd} bus as the reference. The pre-fault Stable Equilibrium Point (SEP) of the full order system is then given as $x_s^{pre} = (\delta_{1s}^{post}, \delta_{2s}^{post}, 0, 0)$. In this study, a pre-fault SEP

equals to a post-fault SEP (x_s^{post}) since there will be no changes in configuration. The motivation for this modeling comes from the possibility to employ RNM of a power system (2.42):

$$\begin{aligned}
\dot{\delta}_1 &= \omega_1; \\
\dot{\delta}_2 &= \omega_2; \\
\dot{\omega}_1 &= \frac{1}{M_1}\Big(P_{m1} - E_1' E_2' B_{12}\sin(\delta_1 - \delta_2) - E_1' B_{13}\sin(\delta_1)\Big); \\
\dot{\omega}_2 &= \frac{1}{M_2}\Big(P_{m2} - E_1' E_2' B_{12}\sin(\delta_2 - \delta_1) - E_2' B_{23}\sin(\delta_2)\Big),
\end{aligned} \tag{3.1}$$

and its exact energy function that has the form:

$$\begin{aligned}
V(\boldsymbol{\delta},\boldsymbol{\omega}) =& V_k(\boldsymbol{\omega}) + V_p(\boldsymbol{\delta}) + C_0 \quad \text{where} \\
V_k(\boldsymbol{\omega}) =& \frac{M_1\omega_1^2}{2} + \frac{M_2\omega_2^2}{2}; \\
V_p(\boldsymbol{\delta}) =& -P_{m1}\delta_1 - P_{m2}\delta_2 - E_1' E_2' B_{12}\cos(\delta_1 - \delta_2) \\
& - E_1' B_{13}\cos(\delta_1) - E_2' B_{23}\cos(\delta_2); \\
C_0 =& -V_p(\delta_{1s}^{post}, \delta_{2s}^{post}),
\end{aligned} \tag{3.2}$$

where C_0 is the value of the potential energy at SEP, with an opposite sign. The constant C_0 is extracted from the general expression for $V_p(\boldsymbol{\delta})$ in order to present the energy function (2.44) concisely. This representation also intuitively outlines that the value of the energy function (3.2) is zero at post-fault SEP ($V(x_s^{post}) = 0$). One may also notice that system (3.1) belongs to the class of conservative systems ($D_1 = D_2 = 0$) which do not support asymptotic stability of SEP. However, due to the existence of the exact energy function, it is possible to get a good picture on how stability margins/region are affected by changes in operating conditions.

3.1.2 Stability region characteristics

In order to analyze the system behavior, three-phase short circuits at the terminal buses of generator 1 (Fault 1) and generator 2 (Fault 2) are simulated for different operating points. Since the role of loads is taken over by the infinite bus, the mechanical power inputs of the generators (P_{m1}, P_{m2}) are chosen as the parameters that will be subject to change (they are varied in the range (0.8-2.5 [p.u.])). The embedded Dormand-Prince method was used as the solver in TDS. Critical clearing times (from now on denoted as t_{cc}) have been identified for each fault and operating

condition. To identify t_{cc} for a certain set-up of parameters, fault clearing time (t_{cl}) has been gradually increased until one or both of the rotor angles swing out of step. Data obtained by TDS for the two critical faults are shown in Figs. 3.2 and 3.3.

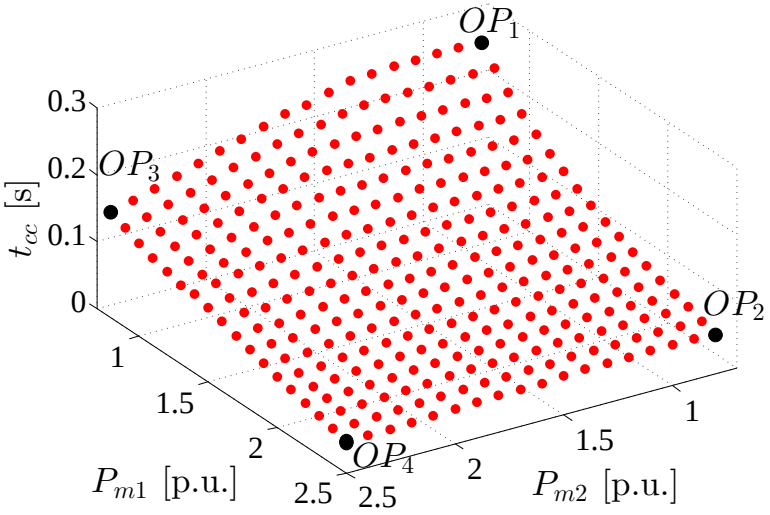

Figure 3.2: TDS results for Fault 1

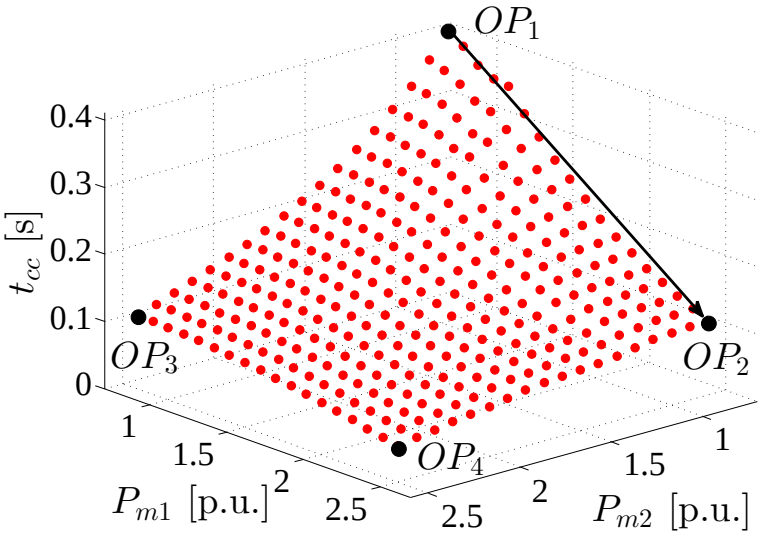

Figure 3.3: TDS results for Fault 2

As expected, t_{cc} decreases as more mechanical power is being injected. From Figs. 3.2-3.3 it is clear that t_{cc} suffers from non-linear changes as the mechanical inputs of the generators are varied. To understand what happens with the stability region of x_s^{post}, this example will focus on the following critical cases of Operating Points (OP):

- OP_1: $P_{m1} = 0.8,\ P_{m2} = 0.8$ [p.u.];
- OP_2: $P_{m1} = 2.5,\ P_{m2} = 0.8$ [p.u.];
- OP_3: $P_{m1} = 0.8,\ P_{m2} = 2.5$ [p.u.] and
- OP_4: $P_{m1} = 2.5,\ P_{m2} = 2.5$ [p.u.].

For each of these four OP, the potential energy surface will be plotted. Despite the fact that the potential energy provides incomplete information (the total energy contains also the portion of kinetic energy), the knowledge about V_p still gives an insight into dynamical behavior of a power system. The boundary of stability region that is defined just in angle space (PEBS) is very close to the original stability boundary in the proximity of type-1 UEPs. PEBS is the union of points where the first local maximum of $V_p(\boldsymbol{\delta})$ is attained along all the radial directions emerging from a post-fault SEP. Practically, this maximum is detected by zero-crossing detection of the directional derivative of the potential energy. For the specific case of the simple system from (3.1), the characterization of PEBS can be given as:

$$PEBS = \left[\begin{array}{cc} \dfrac{-\partial V_p}{-\partial \delta_1} & \dfrac{-\partial V_p}{-\partial \delta_2} \end{array} \right] \cdot \left[\begin{array}{c} \delta_1 - \delta_{1s}^{post} \\ \\ \delta_2 - \delta_{2s}^{post} \end{array} \right] = 0. \tag{3.3}$$

Two unstable, full-order system trajectories were projected on the reduced-order angle-space, as shown in Figs. 3.4-3.6. These projected trajectories for Fault 1 and Fault 2 move along the potential energy surface. In order to additionally associate the directions of the trajectories with the mode of separation of the machines, calculation of type-1 UEPs on the stability boundary is needed. This example avoids complicated and unreliable calculation of UEPs by approximating them. The approximations of interesting UEPs for this test-system are derived from the conclusions for Single Machine Infinite Bus (SMIB) system [116] as:

$$\begin{array}{lll} (\pi - \delta_{1s}^{post}, \delta_{2s}^{post}), & (\delta_{1s}^{post}, \pi - \delta_{2s}^{post}), & (-\pi - \delta_{1s}^{post}, \delta_{2s}^{post}), \\ (\delta_{1s}^{post}, -\pi - \delta_{2s}^{post}), & (\pi - \delta_{1s}^{post}, \pi - \delta_{2s}^{post}), & (-\pi - \delta_{1s}^{post}, -\pi - \delta_{2s}^{post}). \end{array} \tag{3.4}$$

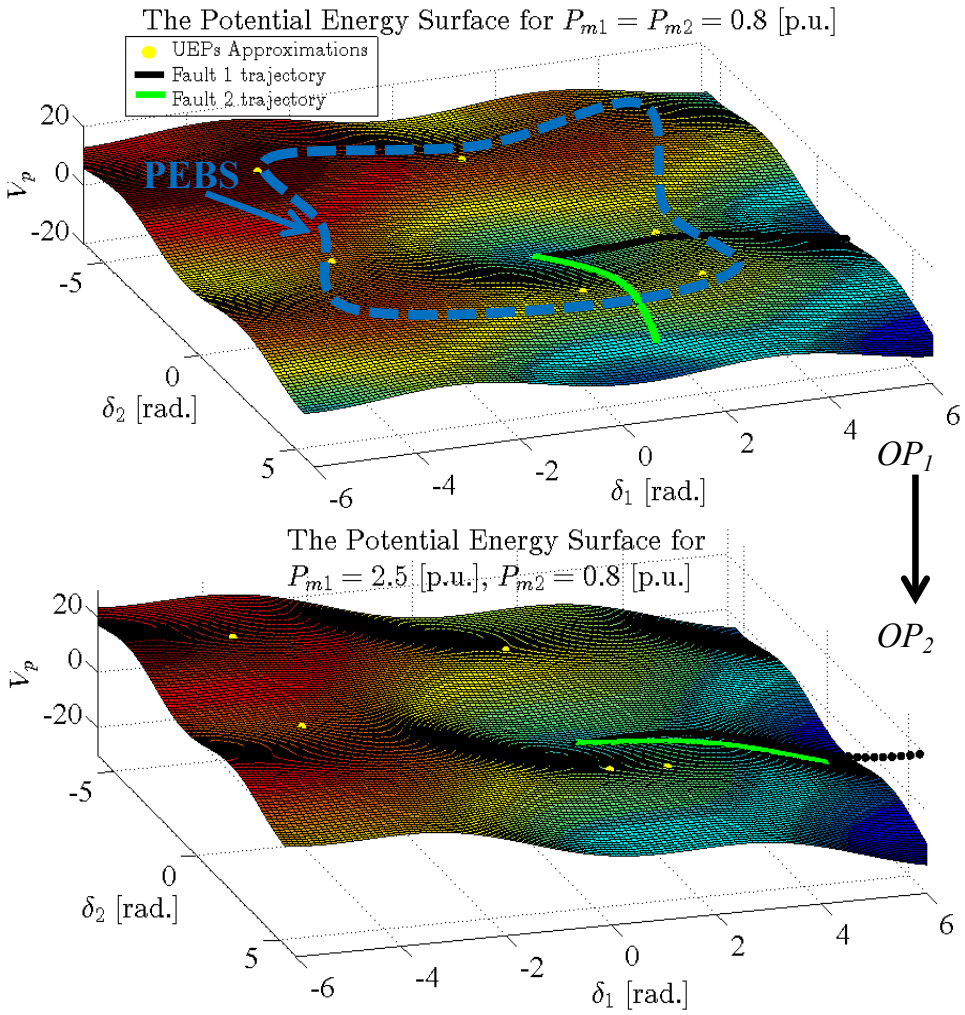

Figure 3.4: Stability region characteristics under operating point perturbation

Each of the approximated equilibria in (3.4) is associated to a certain mode of machine separation. The point where a trajectory exits the stability region is a good indicator about the mode of machine separation. If, for instance, the exit point lies on the stable manifold of the first approximated type-1 UEP from (3.4), G1 would separate from the rest of the system. Then, for each of the four OP, approximations of UEPs were plotted (UEPs Approximations in Fig. 3.4) as yellow markers, in order to follow-up the changes in mode of separation of the machines. In Fig. 3.4,

the Potential Energy Boundary Surface (PEBS), that borders the potential “well", was sketched by a dashed blue line. The bottom of the “well" is the SEP of the post-fault system (x_s^{post}).

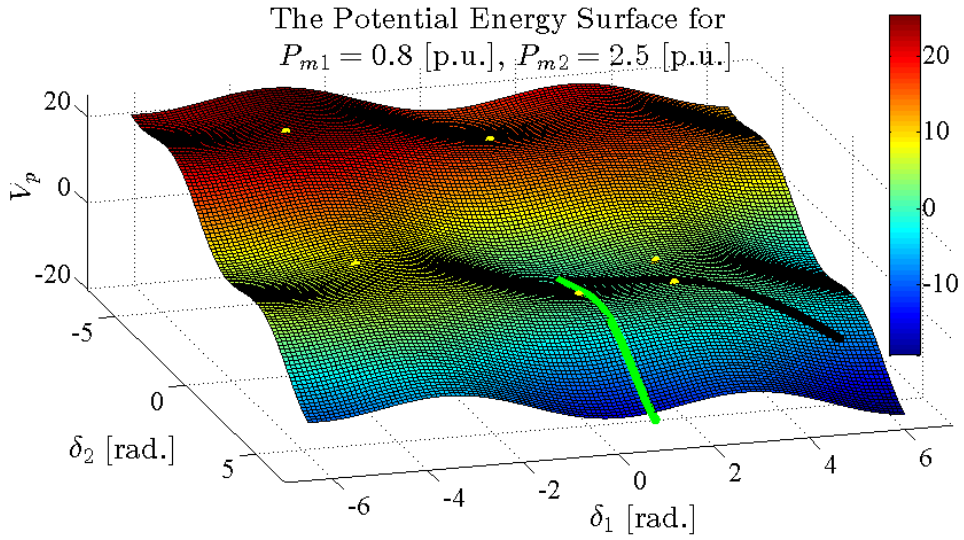

Figure 3.5: Potential energy surface and fault trajectories for $OP3$

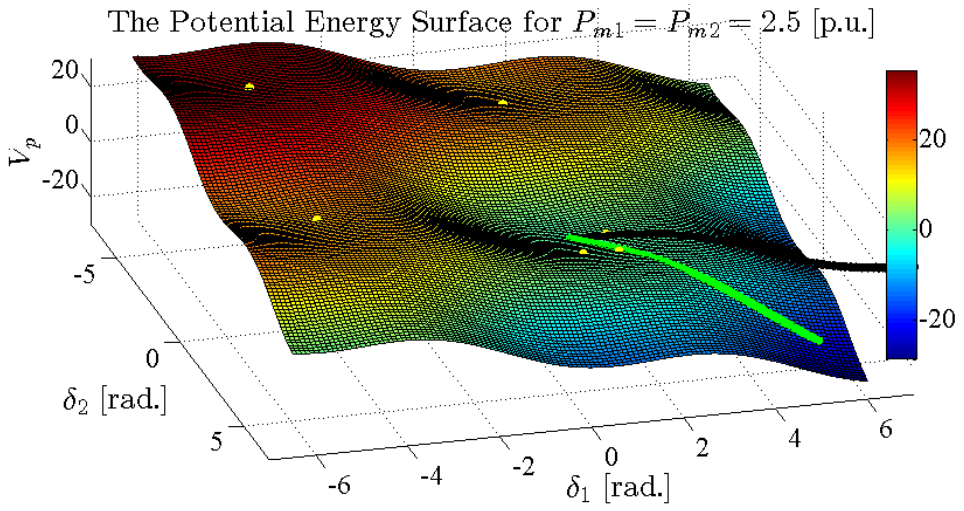

Figure 3.6: Potential energy surface and fault trajectories for $OP4$

Several changes may be noticed as the operating point is varied: (i) SEP and type-1 UEP approximations on the boundary move, (ii) $V_p(\boldsymbol{\delta})$ “well" inclines and (iii) fault trajectories are altered. The changes of UEPs locations in state-space are caused by the variations in SEP x_s^{post} (which is found based on the power flow calculations). This is in line with the research findings that showed how UEPs may move and even disappear as a system becomes more stressed [73]. The potential energy surface apparently tilts towards those UEPs that are “approaching" SEP as the mechanical power inputs increase. Intuitively speaking, this inclination of the energy well makes it easier for the trajectories to escape the stability region in stressed conditions. The increase in mechanical input is reflecting the dynamical behaviour under load increase (with the note that in this case study, the energy function for RNM model is exact). Another related consequence is that the trajectories leave the stability region in different manners. The proximity of a trajectory to an UEP approximation is an indicator of the mode of machine separation, e.g. the machines separate in different ways for OP_1 and OP_2.

This simple illustration demonstrates that the characteristics of a dynamic stability region are significantly influenced by the current operating conditions. Therefore, there is a need to describe these changes analytically, such that a reliable information about the stability margin is always accessible regardless of the variations in operating conditions.

3.1.3 TDS versus direct methods

The same simple system from (3.1) is employed to evaluate the performance of three methods for RAS assessment, namely:

- Time Domain Simulation with Dormand-Prince integration (TDS);
- Closest Unstable Equilibrium Point Approximation (CUEPApp) and;
- Potential Energy Boundary Surface (PEBS) method.

The first approach has already been explained in details and the results have been presented in Figs. 3.2-3.3. The performance test will compare the error made by CUEPApp and PEBS when they estimate t_{cc}. The two approaches belong to the class of direct methods, which means that they do not perform the integration along post-fault trajectory. Instead, t_{cc} is estimated as the point along the unstable, full-order trajectory where the total energy $V(\boldsymbol{\delta}, \boldsymbol{\omega})$ equals to the critical energy. PEBS and CUEPApp differ in the definition of the critical energy as follows:

- CUEPApp method approximates the closest UEP as the one with the lowest potential energy among the equilibria from (3.4). The energy of the approximated closest type-1 UEP is proclaimed as the critical one, i.e.:

$$V_{cr} = \min \begin{Bmatrix} V_p(\pi - \delta_{1s}^{post}, \delta_{2s}^{post}), & V_p(\delta_{1s}^{post}, \pi - \delta_{2s}^{post}), \\ V_p(-\pi - \delta_{1s}^{post}, \delta_{2s}^{post}), & V_p(\delta_{1s}^{post}, -\pi - \delta_{2s}^{post}), \\ V_p(\pi - \delta_{1s}^{post}, \pi - \delta_{2s}^{post}), & V_p(-\pi - \delta_{1s}^{post}, -\pi - \delta_{2s}^{post}). \end{Bmatrix} \quad (3.5)$$

  Hence, to determine t_{cc}, CUEPApp needs to know x_s^{post} (from the load flow) and to carry out one unstable simulation for the given fault and OP. The critical clearing time (t_{cc}) is the time instant where $V(\boldsymbol{\delta}, \boldsymbol{\omega}) = V_{cr}$ on the unstable trajectory.

- Since CUEPApp method is expected to often give conservative estimations of t_{cc}, PEBS method is applied. PEBS does not require the calculation of controlling UEP and on the other hand, it takes into account the direction of a fault-on trajectory. PEBS definition of critical energy is rather straightforward:

$$V_{cr} = V_{PEBS}. \quad (3.6)$$

  The energy V_{PEBS} is the potential energy of the trajectory at $PEBS$ crossing, which can be found based on the explanation from Subsection 2.5.4. This procedure begins with one unstable fault simulation such that the first maximum of V_p is identified along a trajectory. A subsequent simulation identifies t_{cc} by following the same "energy criterion" as in CUEPApp ($V(t_{cc}) = V_{cr}$).

The relative error of t_{cc} that were estimated by direct methods is plotted in Figs. 3.7-3.8. From the figures, it may be concluded that both CUEPApp and PEBS vary from the TDS reference. The character of fault-on trajectories may be blamed for the inaccuracy of estimates in certain regions of the parameter-space. Fig. 3.7 indicates that PEBS does not provide very good estimates for the parameter-space areas close to $OP3$ when fault is at bus 1. This may be associated with the direction of Fault 1 trajectory in Fig. 3.5, which differs from the ones in the cases of OP_1, OP_2 and OP_4. For OP_3, the fault-on trajectory exits the stability region "far" from the type-1 UEP $(\pi - \delta_{1s}^{post}, 0)$. If a trajectory exits the projection of the stability region by crossing the stable manifold of this type-1 UEP, the energy of an exit point contains significant portion of kinetic energy, which further causes lower accuracy of the critical energy estimate (since $V_{cr} = V_{PEBS}$). When CUEPApp provides poor estimates (like in the case of fault 2 from Fig. 3.8), the reason is probably

that the controlling equilibrium is not the closest type-1 UEP. Also, it is good to recall that CUEPApp only approximates the Closest UEP. The general observation from Figs. 3.7-3.8 is that CUEPApp approach has always provided conservative estimations, as expected. PEBS provided both over- and under-estimated t_{cc}.

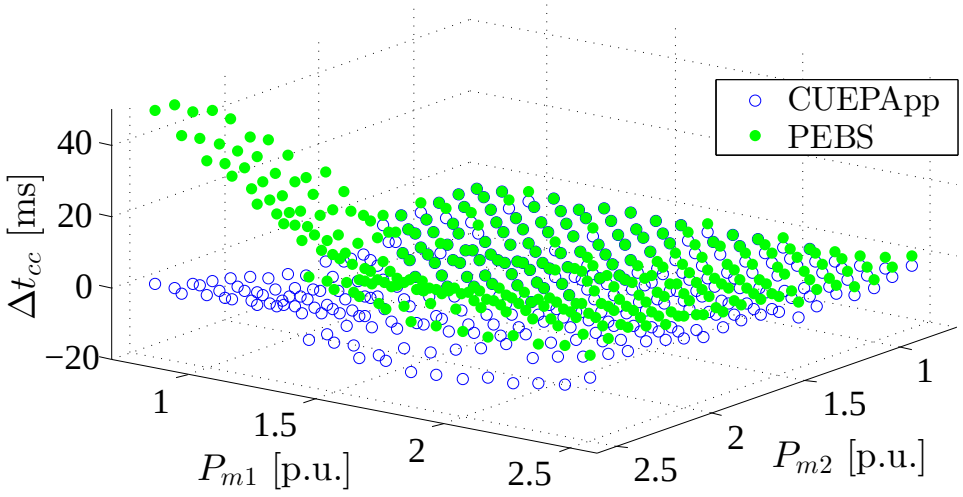

Figure 3.7: The error of direct methods in t_{cc} estimation for Fault 1

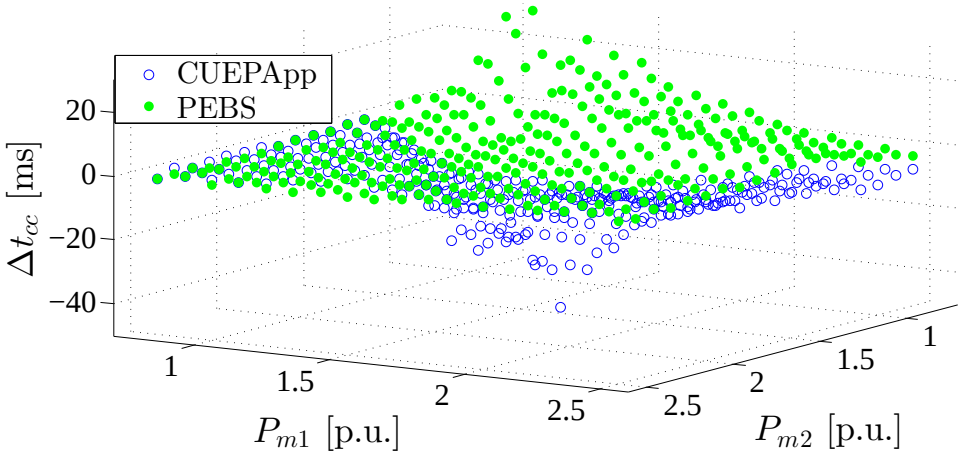

Figure 3.8: The error of direct methods in t_{cc} estimation for Fault 2

The numerical comparison of the average result for the two faults is presented in Table 3.1. The results are given in the form of Relative Error Mean Value (REMV) and its Standard Deviation (SD). The error is measured in [ms] with respect to the TDS reference for each operating condition (and then the average error is calculated for each of the direct methods). Overall observation was that PEBS estimations of t_{cc} are closer to the TDS reference. i.e. CUEPApp estimates were less accurate.

Table 3.1: The average performance of direct methods with respect to TDS reference

TDS	CUEPApp	PEBS
REMV/SD [ms]	REMV/SD [ms]	REMV/SD [ms]
0/0	7.1/7.5	4.9/6.7

Although direct methods may seem attractive due to avoidance of integration of post-fault dynamical equations, they also introduce many difficulties. The primary one is the construction of Lyapunov functions for more complicated models, and some other drawbacks relate to UEP identification and accuracy issues. In this sense, the classical TDS is more reliable tool for DSA. The challenge for TDS is to include some of the advantages that exist in direct methods. This is the topic of the subsequent sections.

3.2 Method idea and algorithm

As shown in the previous example, the characteristics of the stability region change along with operating conditions. It is, therefore, important to have knowledge about the stability index for different operating points in order to assess short-term RAS. The DSA tends to identify stability margins before a critical fault occurs. To simulate faults for a large number of possible operating points requires an extensive amount of computational time. The idea of new methodology is *to describe the perturbation of an operating point by parameterizing the stability boundary* [117]. This means that the important parts of the stability boundary are mapped into security boundary points in parameter-space. Each of these parameter-space points represents the corresponding operating conditions. If it would be possible to make proper expansions over a certain number of parameter-space points, the time for DSA could be reduced drastically.

The proposed methodology is developed in two stages. This chapter mostly deals with parametrizations P1 and P2 in Stage 1 of the algorithm that is depicted in

Fig. 3.9. The focus of this chapter is marked by red color in the figure.

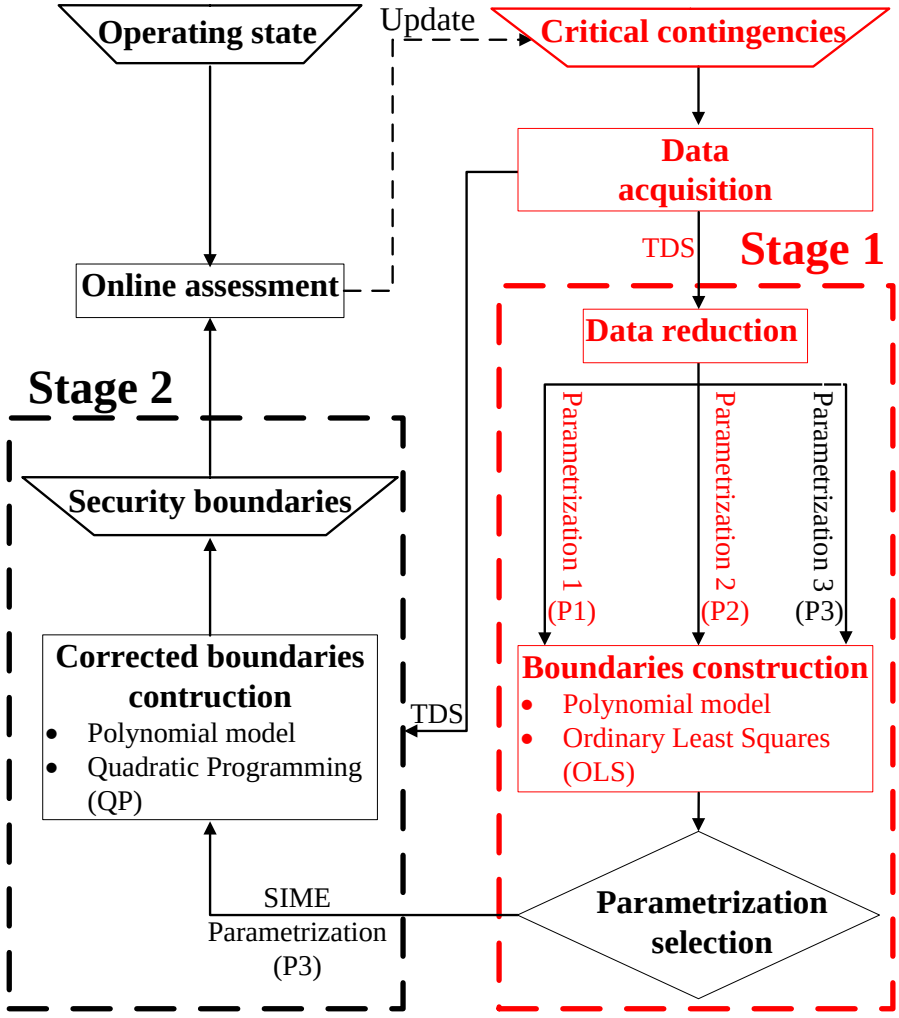

Figure 3.9: The algorithm of short-term RAS methodology construction

Based on the existing knowledge about direct methods and the conclusions that were drawn from the previously presented study, it is reasonable to favor TDS as the data acquisition method. TDS will be carried out for different variations of parameters/operating points and selected critical contingencies. The data acquisition phase has similarities with the standard DSA procedure. However, further on from

this point, the idea is to make polynomial expansions over comparatively smaller data sets by using appropriate functions of selected parameters. It is important to determine how small a sample set can be such that estimations do not deteriorate in accuracy. The mechanical inputs have been chosen as parameters of importance based on the two main arguments:

1. Any change in system parameters has to reflect on generators mechanical inputs via load flow and

2. The amount of additional mechanical power that is required from a generator is strongly connected to the generator ability to remain in synchronism with the rest of the system.

The methodology will determine the analytical relationship between t_{cc} and the functions of parameters of interest (mechanical power inputs of the generators) from the reduced amount of data. The three different proposed functions of parameters will be denoted as parametrizations P1, P2 and P3. All three parametrizations result in security boundaries in polynomial form. This chapter presents the first two parametrizations (P1 and P2) that are actually coming from ordinary polynomial regression over data sets. The third, SIME-based parametrization, will be used in Stage 2 to create corrected polynomial boundaries by the means of Quadratic Programming (QP). P3 (SIME-based) parametrization has a physical meaning and it will be described in details in the following chapter.

3.3 The construction of RAS boundaries

The next step in the method algorithm is to analytically construct boundaries for short-term RAS. This study employs critical clearing times (t_{cc}) as the stability indices. The polynomial of k^{th} order f_p^k is chosen to determine the connection between t_{cc} and parameters of interest. Assuming that the parameters of interest are some power inputs in general form (i.e. $(P_{inp_1}, P_{inp_2}, ..., P_{inp_q})$), the aim of the study is to determine the dependency:

$$t_{cc} = f_p^k(P_{inp_1}, P_{inp_2}, ..., P_{inp_q}). \tag{3.7}$$

The q input powers in Eq. (3.7) depend on the focus of a stability assessment. For instance, TSO may want to use the powers over weak corridors or the power of some loads instead of mechanical inputs of generators.

3.3.1 Polynomial model

For determination of the polynomial f_p^k, it is necessary to gather certain number of data samples. The samples will be collected as $(q+1)$-tuples. Each i^{th} tuple has $(q+1)$ entries $(t_{cc_i}, P_{inp_{1i}}, P_{inp_{2i}}, ..., P_{inp_{qi}})$ that correspond to a certain OP. The polynomial regression model of an i^{th} data sample can be given by:

$$\begin{aligned} t_{cc_i} &= a_{00...00} + a_{10...00}h_1(P_{inp_{1i}}) + a_{01...00}h_2(P_{inp_{2i}}) + ... \\ &+ a_{00...10}h_{(q-1)}(P_{inp_{(q-1)i}}) + a_{00...01}h_q(P_{inp_{qi}}) + \\ &+ a_{20...00}h_1^2(P_{inp_{1i}}) + a_{11...00}h_1(P_{inp_{1i}})h_2(P_{inp_{2i}}) + ... \\ &+ a_{10...01}h_1(P_{inp_{1i}})h_q(P_{inp_{qi}}) + a_{02...00}h_2^2(P_{inp_{2i}}) + ... \\ &+ a_{k0...00}h_1^k(P_{inp_{1i}}) + a_{(k-1)1...00}h_1^{k-1}(P_{inp_{1i}})h_2(P_{inp_{2i}}) + ... \\ &+ a_{00...1(k-1)}h_{(q-1)}(P_{inp_{(q-1)i}})h_q^{k-1}(P_{inp_{qi}}) + a_{00...0k}h_q^k(P_{inp_{qi}}) + \varepsilon_i, \end{aligned} \tag{3.8}$$

where ε_i denotes the unobserved random error of the i^{th} sample. The expressions h_1, h_2, ..., h_q are the explicit functions of input powers P_{inp_1}, P_{inp_2} etc. For p number of $(q+1)$-tuples that are assumed to be available, the polynomial model from Eq. (3.8) may be expressed in matrix notation as:

$$\boldsymbol{t_{cc}} = \mathbf{H}\boldsymbol{a} + \boldsymbol{\varepsilon}, \quad \text{where} \tag{3.9}$$

- $\boldsymbol{t_{cc}} = \begin{bmatrix} t_{cc_1} \\ t_{cc_2} \\ \vdots \\ t_{cc_p} \end{bmatrix}$, $\boldsymbol{a} = \begin{bmatrix} a_{00...00} \\ a_{10...00} \\ \vdots \\ a_{00...1(k-1)} \\ a_{00...0k} \end{bmatrix}$, $\boldsymbol{\varepsilon} = \begin{bmatrix} \varepsilon_1 \\ \varepsilon_2 \\ \vdots \\ \varepsilon_p \end{bmatrix}$, and

- $\mathbf{H} = \begin{bmatrix} 1 & h_1(P_{inp_{11}}) & \dots & h_{q-1}(P_{inp_{(q-1)1}})h_q^{k-1}(P_{inp_{q1}}) & h_q^k(P_{inp_{q1}}) \\ 1 & h_1(P_{inp_{12}}) & \dots & h_{q-1}(P_{inp_{(q-1)2}})h_q^{k-1}(P_{inp_{q2}}) & h_q^k(P_{inp_{q2}}) \\ \vdots & \vdots & \ddots & \vdots & \vdots \\ 1 & h_1(P_{inp_{1p}}) & \dots & h_{q-1}(P_{inp_{(q-1)p}})h_q^{k-1}(P_{inp_{qp}}) & h_q^k(P_{inp_{qp}}) \end{bmatrix}$.

stand for the vectors of critical clearing times ($\boldsymbol{t_{cc}}$), polynomial coefficients ($\boldsymbol{a}$), unobserved random error ($\boldsymbol{\varepsilon}$) and the matrix of parametrization ($\mathbf{H}$), respectively. The matrix $\mathbf{H}$ has known value for a given k. The number of columns in $\mathbf{H}$ equals

to the size of vector $\boldsymbol{a}$ and depends on the polynomial degree k. To be precise, this dimension (the length of $\boldsymbol{a}$) is equal to the sum of number of partitions (p) of integers (w) into q parts for all the integers up to the chosen degree k:

$$\dim(\boldsymbol{a}) = \sum_{w=0}^{k} p(w). \tag{3.10}$$

The further procedure for the estimation of the optimal polynomial coefficients and the order of f_p^k follows in the sequel.

3.3.2 Coefficients estimation

The matrix equation (3.9) represents a linear problem from the optimization point of view. The coefficients ($\boldsymbol{a}$) of the polynomial function f_p^k should be optimal in the sense that unobserved random error ($\boldsymbol{\varepsilon}$) needs to be minimized. A straightforward solution to estimate the optimal coefficient vector $\hat{\boldsymbol{a}}$ is to employ Ordinary Least Squares (OLS) [118]. This is done by creating a function known as Sum of Squared Residuals (SSR) in which the coefficients $\boldsymbol{a}$ serve as the independent variables:

$$SSR(\boldsymbol{a}) = \sum_{i=1}^{p} \varepsilon_i^2 = \sum_{i=1}^{p} (t_{cc_i} - \boldsymbol{H_i a})^2 = (\boldsymbol{t_{cc}} - \mathbf{H}\boldsymbol{a})^T (\boldsymbol{t_{cc}} - \mathbf{H}\boldsymbol{a}). \tag{3.11}$$

Vector $\boldsymbol{H_i}$ is actually the i^{th} row of the parametrization matrix $\mathbf{H}$ (the row that corresponds to the i^{th} data sample). It may easily be demonstrated that the unique minimum of (3.11) ($\min_{\boldsymbol{a}} SSR(\boldsymbol{a})$) is attained at $\hat{\boldsymbol{a}}$ [119] that satisfies:

$$\hat{\boldsymbol{a}} = \left(\frac{1}{p} \sum_{i=1}^{p} \boldsymbol{H_i} \boldsymbol{H_i^T} \right)^{-1} \frac{1}{p} \sum_{i=1}^{p} \boldsymbol{H_i} \boldsymbol{t_{cc}} = (\mathbf{H^T H})^{-1} \mathbf{H^T} \boldsymbol{t_{cc}}, \tag{3.12}$$

due to $SSR(\boldsymbol{a})$ being a quadratic function with a positive definite Hessian. Once having the optimal coefficient vector $\hat{\boldsymbol{a}}$, t_{cc} may be estimated for any other set of parameters that was not included in data sampling as:

$$\boldsymbol{t_{cc}^{est}} = \mathbf{H}\hat{\boldsymbol{a}}. \tag{3.13}$$

The order of f_p^k is identified through a combined iterative procedure that is based both on conventional model validation [120] and error estimation as:

1. The polynomial order s is gradually increased from 1 to ∞ with the step of length 1.

2. The training set consists of 70% of the available data (r) and the remaining 30% of data ($p-r$) has a role of a test set. Relative Error Mean Value of s^{th} iteration (REMV$_s$) is calculated for the test set (i.e. the absolute values of the relative errors of estimates are summed up and divided by the number of estimates).

3. At the iteration step where REMV$_s \geq$REMV$_{(s-1)}$ holds, the optimal polynomial degree is identified as $k = s - 1$.

The security boundary is now fully described by Eq. (3.13). An example of a 3^{rd} degree boundary in 2-dimensional parameter space is:

$$\begin{aligned} t_{cc_i}^{est} =& \hat{a_{00}} + \hat{a_{10}} h_1(P_{inp_{1i}}) + \hat{a_{01}} h_2(P_{inp_{2i}}) + \\ &+ \hat{a_{20}} h_1^2(P_{inp_{1i}}) + \hat{a_{11}} h_1(P_{inp_{1i}}) h_2(P_{inp_{2i}}) + \hat{a_{02}} h_2^2(P_{inp_{2i}}) + \\ &+ \hat{a_{30}} h_1^3(P_{inp_{1i}}) + \hat{a_{21}} h_1^2(P_{inp_{1i}}) h_2(P_{inp_{2i}}) + \\ &+ \hat{a_{12}} h_1(P_{inp_{1i}}) h_2^2(P_{inp_{2i}}) + \hat{a_{03}} h_2^3(P_{inp_{2i}}). \end{aligned} \tag{3.14}$$

Another advantage of the security boundary (3.13) is that it provides the information about stability margin for a certain OP, fault and fault clearing time (t_{cl}). The measure of stability (i.e. stability margin) is directly available as $\Delta t_{cc} = t_{cl} - t_{cc}$. The margin is negative for stable cases ($t_{cl} < t_{cc}$) and larger than zero if a clearing time is “above" the constructed security boundary for a given operating point.

3.4 Parametrizations over data sets

In this methodology, it is convenient to interpret different parametrizations as various choices for the parameter-space basin. For start, this section will propose two simple parametrizations that are ordinary polynomial fits over data sets [121]:

$$\begin{aligned} &\text{P1:} h_j(P_{inp_j}) = P_{inp_j}, \\ &\text{P2:} h_j(P_{inp_j}) = \sqrt{\frac{1}{P_{inp_j}}}, \quad \text{for} \quad j = 1, ...q. \end{aligned} \tag{3.15}$$

The parametrization P2 may seem unusual, however, there is a reasoning behind this choice. The parametrization P2 is motivated by Equal Area Criterion (EAC) for Single Machine Infinite Bus (SMIB) [122]. In the expression for the critical clearing time that comes from EAC, t_{cc} and the square root of mechanical power input of the generator are inversely proportional [56]:

$$t_{cc} = \sqrt{\frac{2M(\delta_{cc} - \delta_s^{pre})}{P_m - P_e^f}}, \quad \text{where} \tag{3.16}$$

- $P_m,\ M$ - represent the mechanical power input of the generator and the constant that reflects the inertia of the generator, respectively;
- $\delta_{cc},\ \delta_s^{pre}$ - are the critical clearing rotor angle and the generator rotor angle at pre-fault SEP, respectively;
- P_e^f - is the constant electrical power of the generator during a fault.

P2 is clearly closer to the theoretical expression for t_{cc} than P1 is. The reason is that the generators will have to adjust their mechanical inputs in order to compensate for the change of any other power in the system. From Eq. (3.15), the corresponding $\mathbf{H}$ matrices for P1 ($\mathbf{H_{P1}}$) and P2 ($\mathbf{H_{P2}}$) are:

$$\mathbf{H_{P1}} = \begin{bmatrix} 1 & P_{inp_{11}} & \dots & P_{inp_{(q-1)1}} P_{inp_{q1}}^{k-1} & P_{inp_{q1}}^{k} \\ 1 & P_{inp_{12}} & \dots & P_{inp_{(q-1)2}} P_{inp_{q2}}^{k-1} & P_{inp_{q2}}^{k} \\ \vdots & \vdots & \ddots & \vdots & \vdots \\ 1 & P_{inp_{1p}} & \dots & P_{inp_{(q-1)p}} P_{inp_{qp}}^{k-1} & P_{inp_{qp}}^{k} \end{bmatrix}, \quad \text{and}$$

$$\mathbf{H_{P2}} = \begin{bmatrix} 1 & \sqrt{\frac{1}{P_{inp_{11}}}} & \dots & \sqrt{\frac{1}{P_{inp_{(q-1)1}}}} \left(\sqrt{\frac{1}{P_{inp_{q1}}}}\right)^{k-1} & \left(\sqrt{\frac{1}{P_{inp_{q1}}}}\right)^{k} \\ 1 & \sqrt{\frac{1}{P_{inp_{12}}}} & \dots & \sqrt{\frac{1}{P_{inp_{(q-1)2}}}} \left(\sqrt{\frac{1}{P_{inp_{q2}}}}\right)^{k-1} & \left(\sqrt{\frac{1}{P_{inp_{q2}}}}\right)^{k} \\ \vdots & \vdots & \ddots & \vdots & \vdots \\ 1 & \sqrt{\frac{1}{P_{inp_{1p}}}} & \dots & \sqrt{\frac{1}{P_{inp_{(q-1)p}}}} \left(\sqrt{\frac{1}{P_{inp_{qp}}}}\right)^{k-1} & \left(\sqrt{\frac{1}{P_{inp_{qp}}}}\right)^{k} \end{bmatrix}, \tag{3.17}$$

respectively. After the vectors of optimal coefficients ($\hat{\boldsymbol{a}}_{\mathbf{P1}}, \hat{\boldsymbol{a}}_{\mathbf{P2}}$) are found based on p observed samples from Eq. (3.12), any fitted $t_{cc_i}^{est}$ value is simply found as:

$$\begin{aligned} \text{P1:} t_{cc_i}^{est} &= \boldsymbol{H}_{\mathbf{P1}i}(P_{inp_{1i}}, P_{inp_{2i}}, ..., P_{inp_{qi}})\hat{\boldsymbol{a}}_{\mathbf{P1}} \\ \text{P2:} t_{cc_i}^{est} &= \boldsymbol{H}_{\mathbf{P2}i}(P_{inp_{1i}}, P_{inp_{2i}}, ..., P_{inp_{qi}})\hat{\boldsymbol{a}}_{\mathbf{P2}}, \end{aligned} \tag{3.18}$$

where $\boldsymbol{H}_{\mathbf{P1}i}$ and $\boldsymbol{H}_{\mathbf{P2}i}$ are actually obtained when any row (e.g. i^{th} row) of the corresponding $\mathbf{H}$ matrix is applied to the current operating point/set of parameters $(P_{inp_{1i}}, P_{inp_{2i}}, ..., P_{inp_{qi}})$. Equation (3.18) is the characterization of the security boundary. When this characterization is available for the critical faults, OP may be frequently updated during operation (on-line) to check if the new, current state carries the risk of transient instability.

3.5 Results

The developed methodology is aiming at using the smallest number of sample data (p) possible. The goal is to retain accuracy even when large amount of data is unavailable and by doing this, to save some part of computational time that is needed for classical DSA with TDS as a tool. This section will reduce the initial data that has been obtained by different data acquisition methods and it will also compare the results of proposed parametrizations P1 and P2.

The case study is carried out by using the same, simple test system from Fig. 3.1. Once again, the symmetrical, three-phase short circuits at buses 1 (Fault 1) and 2 (Fault 2) are of interest. The data that has previously been collected by TDS (Figs. 3.2-3.3), CUEPApp and PEBS (Figs. 3.7-3.8) is now used as an input to P1. P1 is then employed to construct the boundaries and compare the performance of the data acquisition methods. A unique polynomial degree ($k = 3$) is chosen for this comparison. The amount of retained data has been reduced gradually from 100% to 10%. The data is retained in the form of an equidistant grid of parameter-space points. This means that, in the case when 50% of data is reduced, every 2^{nd} 3-tuple from Figs. 3.2-3.3 is kept. The same applies to the case of 75% of reduced data where every 4^{th} sample is retained. The average results for the two critical faults are presented in Table 3.2. The primary purpose of Table 3.2 was not to compare

Table 3.2: Performance of data acquisition methods in parametrization P1

Data reduction [$\%$]	TDS REMV/SD [ms]	CUEPApp REMV/SD [ms]	PEBS REMV/SD [ms]
0	2.76/2.21	7.29/7.59	5.36/6.91
50	2.83/2.24	7.27/7.49	5.43/7.00
75	2.88/2.25	7.30/7.48	5.34/6.97
90	2.96/2.67	7.22/7.35	5.69/7.04

the performance of data acquisition methods. This has been done in Section 3.1. It is parametrization P1 itself that is of interest here. From the given results, the polynomial approximation seems to work effectively in the terms of accuracy. Even in the case when 90% of initial data is removed, the accuracy was not much affected. And again, Table 3.2 confirms that the two direct methods (PEBS and CUEPApp) vary significantly from the TDS reference.

The methodology further continues with only TDS. Security boundaries will

be constructed for Faults 1 and 2 when $P_{inp_1} = P_{m1}$ and $P_{inp_2} = P_{m2}$. The same data range is used as in Figs. 3.2-3.3. Once $(\hat{\boldsymbol{a}}_{\mathbf{P1}}, \hat{\boldsymbol{a}}_{\mathbf{P2}})$ have been estimated, the 3^{rd} order boundary equation becomes available. Graphical representations of the boundaries for Fault 1 (red surface) and Fault 2 (green boundary) are shown in Figs. 3.10-3.11. Figure 3.10 depicts the expansions created by parametrization P1 when initial data is reduced with 90%. Table 3.3 quantifies the results of these estimations.

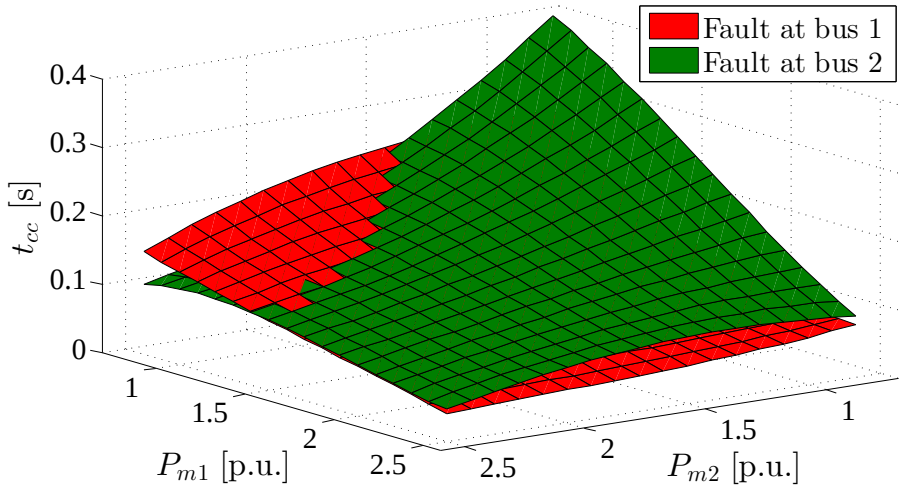

Figure 3.10: Boundaries based on P1 when 10% of data is retained

Table 3.3: The average error of estimates obtained by P1 and P2

Data reduction [%]	P1 REMV/SD [ms]	P2 REMV/SD [ms]
0	2.76/2.21	2.61/2.28
50	2.83/2.24	2.57/2.39
75	2.88/2.25	2.62/2.43
90	2.96/2.67	2.69/3.34

The results from Table 3.3 show that polynomial expansions suffice as models for short-term RAS boundary. It also may be noticed that the amount of reduced data has a minor effect on the accuracy of estimates. The boundaries for different parametrizations and same faults look alike. However, the boundaries created by

P2 appear to be more non-linear in nature. The averaged performance of P2 is also slightly better. This small improvement in P2 implies that those expressions that have physical meaning are likely to give more precise results. The reason is that the axes of parameter-space are more adequate in the case of P2— the sample points are actually functions of powers of interest. This is easy to comprehend by observing Figs. 3.10-3.11. In Fig. 3.10, the lines that connect the points in the parameter-space form a meshed grid of squares. This does not apply to parametrization P2 since the points that correspond to the same powers from P1 now occupy new positions.

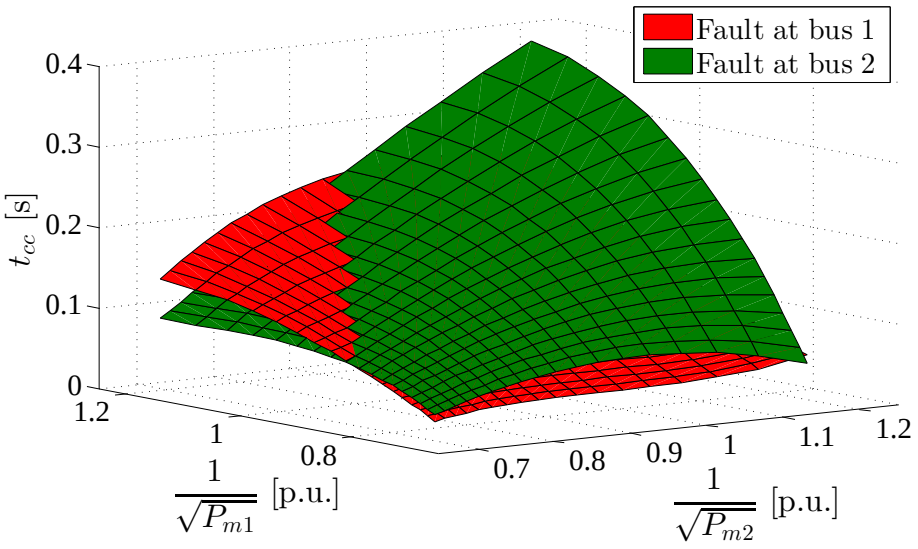

Figure 3.11: Boundaries based on P2 when 10% of data is retained

Finally, several useful conclusions can be drawn from the study of this chapter:

- TDS is more reliable and accurate compared to direct methods (PEBS and CUEPApp). The assessment made by direct methods depends on the nature of faults even in the case of simple system with exact energy function;
- The parametrization with a better choice of axes provided more accurate results;
- The polynomial form of constructed boundaries is suitable for on-line assessment of stability margins.

This study has served as the foundation of the newly introduced parametrization concept that will be further developed in the following chapter.

Chapter 4

SIME-based Parametrization and Constrained RAS Boundary in Parameter-Space

The coming chapter is devoted to further development of the concept of "parameterized boundaries". The aim is to find a more suitable parametrization that has a physical meaning for RAS assessment. The expected outcome of such parametrization are the security boundaries that provide more accurate estimates. Another task of this chapter is to force the security boundaries to be slightly conservative.

It is well-known (and also demonstrated in Chapter 3) that RAS margin is prone to non-linear changes when operating conditions are altered. The parametrization of the stability boundary with the functions of powers as the parameters worked well when security boundaries are constructed as polynomials. This chapter will investigate how to improve these power functions in order to obtain even more accurate estimates. Since the polynomials have demonstrated the capability of supporting the construction of non-linear security boundaries, the new parametrization will keep the polynomial analytical form. Slightly better performance of P2 compared to P1 indicates that a new, better parametrization should be inspired by the analytical relationships that are relevant for finding t_{cc}. The exact expression for t_{cc} has only been developed for the case of Single Machine Infinite Bus (SMIB) system [123]. This system, associated RAS criterion and the SIngle Machine Equivalent (SIME) [45] of a power system constitute the theoretical foundation that is needed for the development of a new parametrization P3. The conservativeness of P3 will add the value to the methodology by making it competitive with UEP-oriented direct methods.

Parametrization P3 (also known here as *SIME-based parametrization*) will be introduced as a “more accurate" and physically meaningful alternative to parametrizations P1 and P2 that were presented in the previous chapter. In order to propose the new, SIME-based parametrization (P3), some important theoretical concepts from power system dynamic analysis need to be explained first.

4.1 SIME method

A SIngle Machine Equivalent (SIME) is a dynamic replacement for a multi-machine power system. SIME is created by transforming the trajectories of a multi-machine system into simplified model that resembles the dynamics of a single machine as:

$$\begin{aligned} \dot{\delta}_{SIME} &= \omega_{SIME}; \\ \dot{\omega}_{SIME} &= M^{-1}(P_{m_{SIME}} - P_{e_{SIME}}). \end{aligned} \tag{4.1}$$

The parameters of (4.1) are determined based on the following procedure:

1. In the first step of the SIME method, a two-machine equivalent replaces the original power system model. Each of these two machines represents one of the two groups, namely critical (subscript C) and non-critical group (subscript NC) of generators. The critical group is the one that swings out to instability, i.e. the critical group is responsible for the loss of synchronism. The generators are divided into two groups based on their mode of separation for a certain fault and operating state. This means that one TDS first needs to be carried out in order to identify in which way the machines separate. The equivalent groups will have the corresponding angles (δ_C, δ_{NC}) and angle speeds (ω_C, ω_{NC}) defined as:

$$\delta_C = M_C^{-1} \sum_{i \in C} M_i \delta_i, \qquad \delta_{NC} = M_{NC}^{-1} \sum_{j \in NC} M_j \delta_j, \tag{4.2}$$

$$\omega_C = M_C^{-1} \sum_{i \in C} M_i \omega_i, \qquad \omega_{NC} = M_{NC}^{-1} \sum_{j \in NC} M_j \omega_j, \text{ where} \tag{4.3}$$

$$M_C = \sum_{i \in C} M_i \qquad \text{and} \qquad M_{NC} = \sum_{j \in NC} M_j. \tag{4.4}$$

2. The critical (C) and non-critical (NC) equivalent groups are further substi-

tuted by a SIME (4.1) whose parameters are given by:

$$\begin{aligned}
\delta_{SIME} &= \delta_C - \delta_{NC};\\
\omega_{SIME} &= \omega_C - \omega_{NC};\\
P_{m_{SIME}} &= M_T^{-1}\left(M_C \sum_{i\in C} P_{mi} - M_{NC} \sum_{j\in NC} P_{mj}\right);\\
P_{e_{SIME}} &= M_T^{-1}\left(M_C \sum_{i\in C} P_{ei} - M_{NC} \sum_{j\in NC} P_{ej}\right);\\
M &= \frac{M_C M_{NC}}{M_T} \quad \text{and} \quad M_T = M_C + M_{NC}.
\end{aligned} \tag{4.5}$$

These parameters will change their values in each integration step as TDS progresses. The time series $\delta_{SIME}, \omega_{SIME}$ may then be interpreted as a dynamical trajectory of one machine.

Clearly, SIME parameters rely on the categorization of machines (i.e. on the way that the generators are grouped). However, by establishing SIME for different faults, various possibilities arise. The degree of the dynamical model for transient stability analysis is reduced. Furthermore, SIME provides the information about the mode of machine separation. The most interesting characteristic of SIME is the possibility to apply some theoretical concepts that are specifically developed for the case of Single Machine Infinite Bus (SMIB) system.

4.2 Equal Area Criterion for SMIB system

This subsection presents some results of interest for transient stability that are obtained by employing a simple SMIB test system from Fig. 4.1.

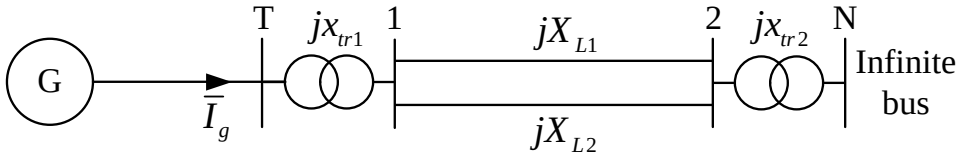

Figure 4.1: SMIB test system for short-term RAS studies

The equivalent circuit of the system from Fig. 4.1 is shown in Fig. 4.2. The assumptions are that (i) the synchronous generator is represented by the classical

model that was given in Subsection 2.2.1, (ii) the transmission lines are modeled by series reactances X_{L1} and X_{L2} (lossless system), (iii) the mechanical power P_m is constant and (iv) both the module and the angle of the infinite bus voltage $\bar{U}_N = U_N \angle \theta_N$ are fixed.

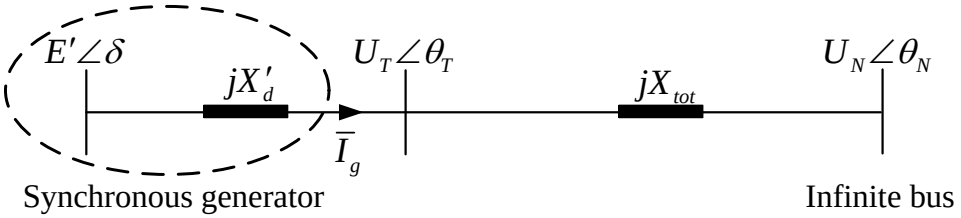

Figure 4.2: The equivalent circuit of SMIB test system

Now, in order to find the criterion for short-term RAS for this test system, both sides of the associated swing equation (for damping $D = 0$):

$$\dot{\omega} = \frac{1}{M}(P_m - P_e(\delta)) \tag{4.6}$$

will be multiplied by the angle speed $\omega = d\delta/dt$ in order to obtain:

$$\omega \frac{d\omega}{dt} = \frac{1}{M}(P_m - P_e(\delta))\frac{d\delta}{dt}. \tag{4.7}$$

For a dynamic trajectory which originates from SEP $(\delta_s^{pre}, 0)$, the necessary transient stability condition is that at some point (and time $t_{\omega=0}$), the equality $\omega(t_{\omega=0}) = d\delta/dt(t_{\omega=0}) = 0$ holds. The equivalent statement would be that there needs to exist a moment $t_{\omega=0}$ along a trajectory where the rotor angle reaches some maximum value δ_{max} and then swings back. By integrating (4.7), it is straightforward to obtain:

$$\begin{aligned} \int_0^{\omega(t_{\omega=0})} \omega d\omega &= \frac{1}{M}\int_{\delta_s^{pre}}^{\delta_{max}} (P_m - P_e(\delta))d\delta \Rightarrow \\ \omega(t_{\omega=0}) &= \sqrt{\frac{2}{M}\int_{\delta_s^{pre}}^{\delta_{max}} (P_m - P_e(\delta))d\delta}. \end{aligned} \tag{4.8}$$

By applying the condition for short-term RAS ($\omega(t_{\omega=0}) = 0$), the equation for finding the maximum rotor angle is set up as:

$$0 = \int_{\delta_s^{pre}}^{\delta_{max}} (P_m - P_e(\delta))d\delta. \tag{4.9}$$

To find a finite δ_{max}, the equation (4.9) is partitioned with respect to the angle δ_{cl} which corresponds to the time of fault clearing t_{cl}:

$$\begin{aligned} 0 = \int_{\delta_s^{pre}}^{\delta_{cl}} (P_m - P_e^f(\delta))d\delta + \int_{\delta_{cl}}^{\delta_{max}} (P_m - P_e^{post}(\delta))d\delta \Rightarrow \\ \int_{\delta_s^{pre}}^{\delta_{cl}} (P_m - P_e^f(\delta))d\delta = \int_{\delta_{cl}}^{\delta_{max}} (P_e^{post}(\delta) - P_m)d\delta \Rightarrow \\ A_a = A_d, \end{aligned} \tag{4.10}$$

where A_a and A_d denote acceleration and deceleration areas under the curves that are “inside" the integrals. This equality is widely known as Equal Area Criterion (EAC) [112] that is used for transient stability assessment. The illustration from Fig. 4.3 will help to clarify the relationships between the electric power characteristics, areas A_a/A_d and rotor angles of importance.

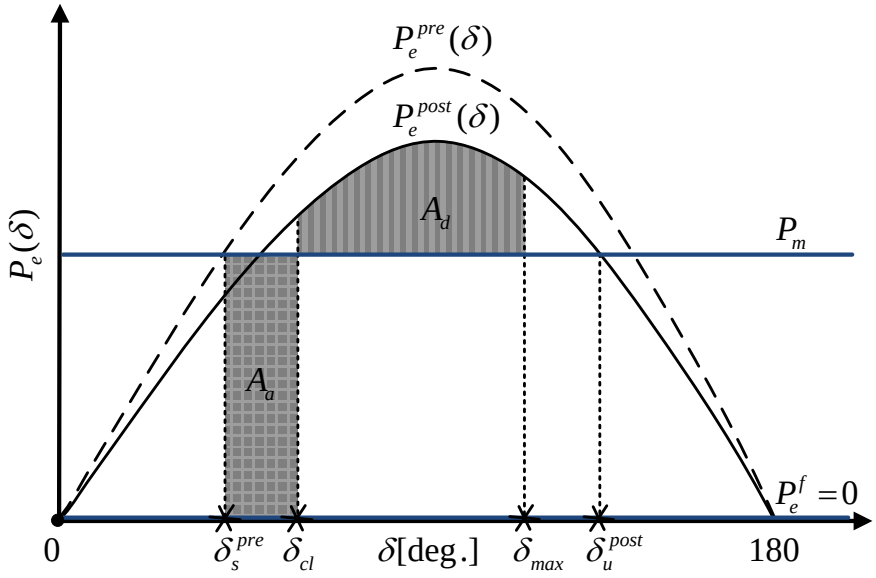

Figure 4.3: Graphical representation of the Equal Area Criterion

In Fig. 4.3, the pre-fault SEP $(\delta_s^{pre}, 0)$ and the post-fault SEP $(\delta_s^{post}, 0)$ are not the same (i.e. $P_e^{pre}(\delta)$ and $P_e^{post}(\delta)$ differ from each other). The electric power during the fault is assumed to be zero ($P_e^f = 0$). This set-up corresponds to an example where a fault has happened on one of the lines from Fig. 4.1 very close

to the infinite bus and where the faulted line was tripped to clear the fault. The acceleration and deceleration areas can now also be interpreted via their physical meaning. From the integration of Eq. (4.7) during a fault (from $\delta = \delta_s^{pre}$ to δ_{cl}), accelerating area A_a can also be given in the following form:

$$\begin{aligned} \int_0^{\omega_{cl}} \omega d\omega = \frac{1}{M} \int_{\delta_s^{pre}}^{\delta_{cl}} (P_m - P_e^f(\delta)) d\delta \Rightarrow \\ \frac{1}{2} M \omega_{cl}^2 = P_m(\delta_{cl} - \delta_s^{pre}) = A_a \Rightarrow \\ A_a = \frac{1}{2} M \omega_{cl}^2. \end{aligned} \tag{4.11}$$

This result indicates that the accelerating area A_a actually represents the kinetic energy that is injected into the system due to the motion of the rotor during a fault. The kinetic energy enlarges along with the angle of fault clearing δ_{cl}. By performing the integration of Eq. (4.7) for the post-fault period in the similar fashion, the following relationships may be obtained:

$$\begin{aligned} \int_{\omega_{cl}}^{0} \omega d\omega = \frac{1}{M} \int_{\delta_{cl}}^{\delta_{max}} (P_m - P_e^{post}(\delta)) d\delta \Rightarrow \\ -\frac{1}{2} M \omega_{cl}^2 = P_m(\delta_{max} - \delta_{cl}) + P_{emax}^{post} \Big(\cos(\delta_{max}) - \cos(\delta_{cl}) \Big) = -A_d \Rightarrow \\ A_d = -P_m(\delta_{max} - \delta_{cl}) - P_{emax}^{post} \Big(\cos(\delta_{max}) - \cos(\delta_{cl}) \Big), \end{aligned} \tag{4.12}$$

where the decelerating area A_d is equivalent to the potential energy of a power system. Potential energy reflects the ability of a power system to absorb the energy that was injected during the fault-on period.

The case from Fig. 4.4 corresponds to the maximum fault clearing angle δ_{cl} that does not lead to instability. This angle is known as critical clearing angle δ_{cc}. The deceleration area in this case reaches its maximum value, i.e. $A_d = A_d^{max}$. If a fault is cleared for an angle that is larger than δ_{cc}, the rotor would swing out beyond unstable UEP of the post-fault system ($\delta_u^{post} = 180^\circ - \delta_s^{post}, 0$), which is the “point of no return" in the sense of transient stability. If this would be the case, the kinetic energy of the generator would be large enough to “push" the machine out of synchronism. This happens due to the fact that the potential energy (which acts as a synchronizing force) has reached its maximum. There is no margin to further increase the potential energy and neutralize the effect of the remaining part of the kinetic energy which then separates the generator from the infinite bus. It

is therefore crucial to know the value of δ_{cc} and its corresponding critical clearing time t_{cc}.

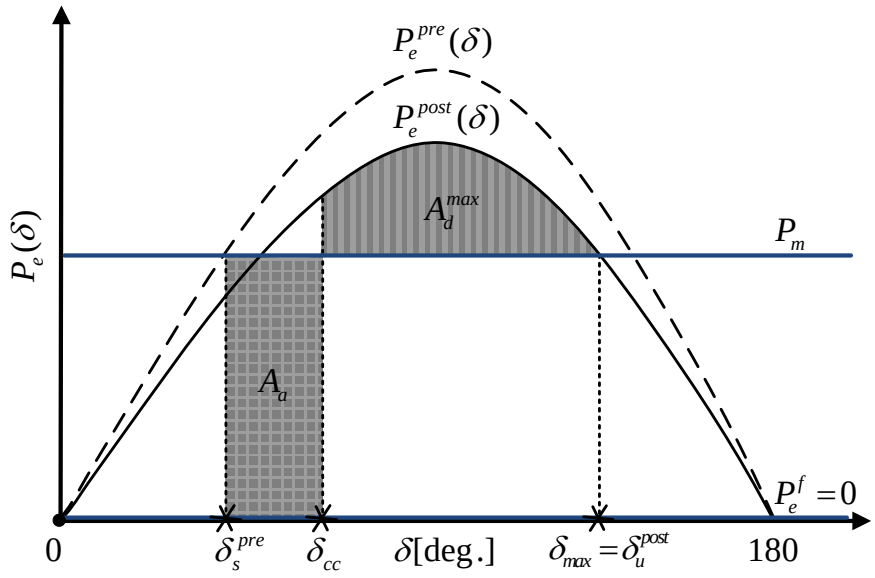

Figure 4.4: Equal Area Criterion for the case of critical clearing angle δ_{cc}

Let it be noted that $P_e^{pre}(\delta) = P_{emax}^{pre}\sin(\delta)$ and $P_e^{post}(\delta) = P_{emax}^{post}\sin(\delta)$. For the system from Fig. 4.2, EAC can then be used for this critical case ($\delta_c = \delta_{cc}$, $\delta_{max} = \delta_u^{post}$) to calculate the critical clearing angle δ_{cc} and the critical clearing time t_{cc} analytically from the following transformations:

$$\begin{aligned} A_a &= A_d^{max} \Rightarrow \\ \int_{\delta_s^{pre}}^{\delta_{cc}} (P_m - P_e^f)d\delta &= \int_{\delta_{cc}}^{\delta_{max}} (P_e^{post}(\delta) - P_m)d\delta \Rightarrow \\ P_m(\delta_{cc} - \delta_s^{pre}) &= -P_{emax}^{post}\Big(\cos(\delta_{max}) - \cos(\delta_{cc})\Big) - P_m(\delta_{max} - \delta_{cc}), \end{aligned} \tag{4.13}$$

that provide the exact result for the critical clearing angle as:

$$\delta_{cc} = \arccos\left(\cos(\delta_{max}) + \frac{P_m}{P_{emax}^{post}}(\delta_{max} - \delta_s^{pre})\right). \tag{4.14}$$

By having δ_{cc}, the two integrations of the swing equation during a fault:

$$\frac{d^2\delta}{dt^2} = \frac{1}{M}(P_m - P_e^f), \tag{4.15}$$

result in the equation from which critical clearing time t_{cc} can be easily found as:

$$\int_{\delta_s^{pre}}^{\delta_{cc}} d\delta = \int_{t=0}^{t_{cc}} \frac{P_m - P_e^f}{M} t dt \Rightarrow \delta_{cc} - \delta_s^{pre} = \frac{P_m - P_e^f}{2M} t_{cc}^2 \Rightarrow$$
$$t_{cc} = \sqrt{\frac{2M(\delta_{cc} - \delta_s^{pre})}{P_m - P_e^f}}, \tag{4.16}$$

when $P_e^f = const$. The given expression for SMIB system will further be employed in the construction of an improved methodology for short-term RAS assessment.

4.3 SIME-based parametrization

The novelty of a new approach lies in the choice of a more adequate parametrization that has a physical meaning and also introduces several other advantages. Chapter 3 has determined that the accuracy of estimates is likely to be affected by the relationship between the parameter-space axes and the parameters of interest.

4.3.1 Polynomial model for SIME parametrization

The idea of the third, SIME-based, parametrization P3 is to incorporate SIME into the expression for the critical clearing time of SMIB as:

$$t_{cc} = \sqrt{\frac{2M(\delta_{cc_{SIME}} - \delta_{s_{SIME}}^{pre})}{P_{m_{SIME}} - P_{e_{SIME}}^f}} \tag{4.17}$$

in order to find a more appropriate basin for the parameter-space. The difference compared to Eq. (4.16) is that the parameters and variables M, $\delta_{cc_{SIME}}$, $\delta_{s_{SIME}}^{pre}$, $P_{m_{SIME}}$ and $P_{e_{SIME}}^f$ are now related to the SIME of a multi-machine power system, as explained in Section 4.1. If, additionally, the most critical case is considered ($P_{e_{SIME}}^f = 0$), the resulting expression for t_{cc} becomes:

$$t_{cc} = \sqrt{\frac{2M(\delta_{cc_{SIME}} - \delta_{s_{SIME}}^{pre})}{P_{m_{SIME}}}}. \tag{4.18}$$

To be able to employ SIME quantities in the expression (4.18), the mode of separation needs to be established. Establishing t_{cc} via TDS always involves one simulation where synchronism is lost. The unstable simulation is all what is needed to determine how the machines separate from each other due to transient instability.

TDS has also been chosen as the data acquisition method in the methodological approach that was proposed in Chapter 3. Hence, the unstable simulation is a step that has been already included in constructing the security boundaries by parametrizations P1 and P2.

Now, let the new quantity — “SIME-distance" be defined as:

$$\delta_{SIME}^{DIST} = 2M(\delta_{cc_{SIME}} - \delta_{s_{SIME}}^{pre}) \tag{4.19}$$

where $\delta_{cc_{SIME}}$ and $\delta_{s_{SIME}}^{pre}$ are the critical clearing angle and pre-fault SEP of SIME, respectively. Clearly, these two angles relate to a specific fault and operating point. The axes of the new parametrization P3 will be defined by h_j functions as:

$$\begin{aligned} \text{P3:} h_j(P_{mj}, \delta_{SIME}^{DIST}) &= \sqrt{\frac{2M(\delta_{cc_{SIME}} - \delta_{s_{SIME}}^{pre})}{P_{mj}}} \\ &= \sqrt{\frac{\delta_{SIME}^{DIST}}{P_{mj}}} \quad \text{for} \quad j = 1, ...n. \end{aligned} \tag{4.20}$$

where n is the number of generators. Each of $h_j(P_{mj}, \delta_{SIME}^{DIST})$ functions defines one of the axes by the ratio between newly introduced “global" index δ_{SIME}^{DIST} and individual mechanical power of one generator (P_{mj}). Hence, the basin of the parameter-space will be constituted by n axes of the form $h_j(P_{mj}, \delta_{SIME}^{DIST})$. In a sense, this parametrization describes the sensitivity of SIME distance δ_{SIME}^{DIST} along different parameter-space directions. This sensitivity should capture any change of active power in the system, since at least some of the mechanical powers $(P_{m1}, P_{m2}, ..., P_{mn})$ will have to compensate for the network/load variation in active power. The angle of SIME pre-fault SEP can be easily found from the knowledge about machine separation and power flow calculations as:

$$\delta_{s_{SIME}}^{pre} = \delta_{s_C}^{pre} - \delta_{s_{NC}}^{pre}, \tag{4.21}$$

where the subscripts of the angle equivalents are used to denote the critical (C) and non-critical (NC) groups of generators. Finding the critical clearing angle of SIME ($\delta_{cc_{SIME}}$) by TDS is equivalent to finding critical clearing time t_{cc}, i.e. $\delta_{cc_{SIME}}$ is available in data samples obtained from simulations. However, $\delta_{cc_{SIME}}$ (and consequently, δ_{SIME}^{DIST}) is not available for the operating points where a simulation has not been carried out/where t_{cc} should be estimated. P3 will therefore involve one additional step where δ_{SIME}^{DIST} is found as a polynomial function of power inputs:

$$\delta_{SIME}^{DIST}(P_{inp_1}, P_{inp_2}, ..., P_{inp_q}) = f_p^k(P_{inp_1}, P_{inp_2}, ..., P_{inp_q}). \tag{4.22}$$

The input powers can be any active powers of importance. The estimates of δ_{SIME}^{DIST} for the points where TDS data has not been collected are easily obtained in the same way as t_{cc} was identified in P1:

$$\boldsymbol{\delta}_{\boldsymbol{SIME}}^{\boldsymbol{DIST_{est}}} = \mathbf{H_{P1}}(P_{inp_{1i}}, P_{inp_{2i}}, ..., P_{inp_{qi}})\hat{\boldsymbol{a}}_{\mathbf{P1}} \Leftrightarrow$$

$$\begin{bmatrix} \delta_{SIME_1}^{DIST_{est}} \\ \delta_{SIME_2}^{DIST_{est}} \\ \vdots \\ \delta_{SIME_p}^{DIST_{est}} \end{bmatrix} = \begin{bmatrix} 1 & P_{inp_{11}} & \dots & P_{inp_{(q-1)1}} P_{inp_{q1}}^{k-1} & P_{inp_{q1}}^{k} \\ 1 & P_{inp_{12}} & \dots & P_{inp_{(q-1)2}} P_{inp_{q2}}^{k-1} & P_{inp_{q2}}^{k} \\ \vdots & \vdots & \ddots & \vdots & \\ 1 & P_{inp_{1p}} & \dots & P_{inp_{(q-1)p}} P_{inp_{qp}}^{k-1} & P_{inp_{qp}}^{k} \end{bmatrix} \begin{bmatrix} \hat{a}_{00...00} \\ \hat{a}_{10...00} \\ \vdots \\ \hat{a}_{00...1(k-1)} \\ \hat{a}_{00...0k} \end{bmatrix}. \quad (4.23)$$

The steps for finding the polynomial degree and optimal coefficients are identical to those described in Chapter 3. By importing the function (4.22) into the axes of parametrization P3 from Eq. (4.20), the parameter-space basin may be given as:

$$\text{P3:} h_j(P_{mj}, \delta_{SIME}^{DIST}(P_{inp_1}, P_{inp_2}, ..., P_{inp_q})) = \sqrt{\frac{\delta_{SIME}^{DIST}}{P_{mj}}} \text{ for } j = 1, ...n. \quad (4.24)$$

The second step of SIME-based parametrization sets up the polynomial regression model for the estimation of the optimal coefficient vector $\hat{\boldsymbol{a}}$. This model will involve a new matrix $\mathbf{H}_{\boldsymbol{SIME}}$ that corresponds to parametrization P3:

$$\boldsymbol{t_{cc}} = \mathbf{H}_{\boldsymbol{SIME}}\boldsymbol{a} + \boldsymbol{\varepsilon}, \quad \text{where} \quad (4.25)$$

- $\boldsymbol{t_{cc}}$, $\boldsymbol{a}$ and $\boldsymbol{\varepsilon}$ are the vectors that have the same structure as in Eq. (3.9) and

- $\mathbf{H}_{\boldsymbol{SIME}} = \begin{bmatrix} 1 & \dots & h_n^k(P_{mn_1}, \delta_{SIME_1}^{DIST}(P_{inp_1}, P_{inp_2}..., P_{inp_q})) \\ 1 & \dots & h_n^k(P_{mn_2}, \delta_{SIME_2}^{DIST}(P_{inp_1}, P_{inp_2}..., P_{inp_q})) \\ \vdots & \ddots & \vdots \\ 1 & \dots & h_n^k(P_{mn_p}, \delta_{SIME_p}^{DIST}(P_{inp_1}, P_{inp_2}..., P_{inp_q})) \end{bmatrix}.$

The optimal coefficient vector for parametrization P3, $\hat{\boldsymbol{a}}_{\mathbf{P3}}$, is once again found by the OLS procedure that was explained in Subsection 3.3.2 of Chapter 3. To sum up, the resulting two-step procedure for the estimation of some i^{th} sample of critical clearing time $t_{cc_i}^{est}$ by SIME parametrization is:

$$\text{Step 1:} \quad \delta_{SIME_i}^{DIST_{est}} = \boldsymbol{H_{P1}}_{\boldsymbol{i}}(P_{inp_{1i}}, P_{inp_{2i}}, ..., P_{inp_{qi}})\hat{\boldsymbol{a}}_{\mathbf{P1}} \quad (4.26)$$

$$\text{Step 2:} \quad t_{cc_i}^{est} = \boldsymbol{H_{SIME_i}}(P_{m1_i}, P_{m2_i}, ..., P_{mn_i}, \delta_{SIME_i}^{DIST_{est}})\hat{\boldsymbol{a}}_{\mathbf{P3}}. \quad (4.27)$$

The values of vectors $\boldsymbol{H_{P1i}}$ and $\boldsymbol{H_{SIME_i}}$ are found by applying the i^{th} rows of the corresponding matrices ($\mathbf{H_{P1}}$ and $\mathbf{H_{SIME}}$) on the operating point of interest. In order to better understand the procedure, matrix $\mathbf{H_{SIME}}$ from Eq. (4.25) can also be given in a more specific form. Assuming that a certain number p of TDS data samples is available, $\mathbf{H_{SIME}}$ has the following structure:

$$\mathbf{H_{SIME}} = \begin{bmatrix} 1 & \sqrt{\frac{\delta^{DIST}_{SIME_1}}{P_{m1_1}}} & \cdots & \sqrt{\frac{\delta^{DIST}_{SIME_1}}{P_{m(n-1)_1}}} & \left(\sqrt{\frac{\delta^{DIST}_{SIME_1}}{P_{mn_1}}}\right)^{k-1} & \left(\sqrt{\frac{\delta^{DIST}_{SIME_1}}{P_{mn_1}}}\right)^{k} \\ 1 & \sqrt{\frac{\delta^{DIST}_{SIME_2}}{P_{m1_2}}} & \cdots & \sqrt{\frac{\delta^{DIST}_{SIME_2}}{P_{m(n-1)_2}}} & \left(\sqrt{\frac{\delta^{DIST}_{SIME_2}}{P_{mn_2}}}\right)^{k-1} & \left(\sqrt{\frac{\delta^{DIST}_{SIME_2}}{P_{mn_2}}}\right)^{k} \\ \vdots & \vdots & \ddots & & \vdots & \vdots \\ 1 & \sqrt{\frac{\delta^{DIST}_{SIME_p}}{P_{m1_p}}} & \cdots & \sqrt{\frac{\delta^{DIST}_{SIME_p}}{P_{m(n-1)_p}}} & \left(\sqrt{\frac{\delta^{DIST}_{SIME_p}}{P_{mn_p}}}\right)^{k-1} & \left(\sqrt{\frac{\delta^{DIST}_{SIME_p}}{P_{mn_p}}}\right)^{k} \end{bmatrix}.$$

From $\mathbf{H_{SIME}}$ matrix it may be observed that the basin of the parameter-space in SIME parametrization has n dimensions, i.e. the number of dimensions equals to the number of generators. If the optimal coefficient vector has the form:

$$\hat{\boldsymbol{a}}_{\mathbf{P3}} = \begin{bmatrix} \hat{a}_{00\ldots00} & \hat{a}_{10\ldots00} & \ldots & \hat{a}_{00\ldots1(k-1)} & \hat{a}_{00\ldots0k} \end{bmatrix}^T,$$

then some i^{th} estimation of $t^{est}_{cc_i}$ is found by a k^{th}-order approximation as:

$$\begin{aligned} t^{est}_{cc_i} = {} & \hat{a}_{00\ldots00} + \hat{a}_{10\ldots00}\sqrt{\frac{\delta^{DIST_{est}}_{SIME_i}}{P_{m1_i}}} + \hat{a}_{01\ldots00}\sqrt{\frac{\delta^{DIST_{est}}_{SIME_i}}{P_{m2_i}}} + \ldots + \hat{a}_{00\ldots01}\sqrt{\frac{\delta^{DIST_{est}}_{SIME_i}}{P_{mn_i}}} \\ & + \hat{a}_{20\ldots00}\frac{\delta^{DIST_{est}}_{SIME_i}}{P_{m1_i}} + \hat{a}_{11\ldots00}\frac{\delta^{DIST_{est}}_{SIME_i}}{\sqrt{P_{m1_i}P_{m2_i}}} + \ldots + \hat{a}_{10\ldots01}\frac{\delta^{DIST_{est}}_{SIME_i}}{\sqrt{P_{m1_i}P_{mn_i}}} + \ldots \\ & + \hat{a}_{k0\ldots00}\left(\sqrt{\frac{\delta^{DIST_{est}}_{SIME_i}}{P_{m1_i}}}\right)^{k} + \hat{a}_{(k-1)1\ldots00}\left(\sqrt{\frac{\delta^{DIST_{est}}_{SIME_i}}{P_{m1_i}}}\right)^{k-1}\sqrt{\frac{\delta^{DIST_{est}}_{SIME_i}}{P_{m2_i}}} + \ldots \\ & + \hat{a}_{00\ldots1(k-1)}\sqrt{\frac{\delta^{DIST_{est}}_{SIME_i}}{P_{m(n-1)_i}}}\left(\sqrt{\frac{\delta^{DIST_{est}}_{SIME_i}}{P_{mn_i}}}\right)^{k-1} + \hat{a}_{00\ldots0k}\left(\sqrt{\frac{\delta^{DIST_{est}}_{SIME_i}}{P_{mn_i}}}\right)^{k}. \end{aligned} \tag{4.28}$$

The definition of parametrization P3 completes Stage 1 (as indicated by red color in the algorithm from Fig. 4.5) of the methodology construction.

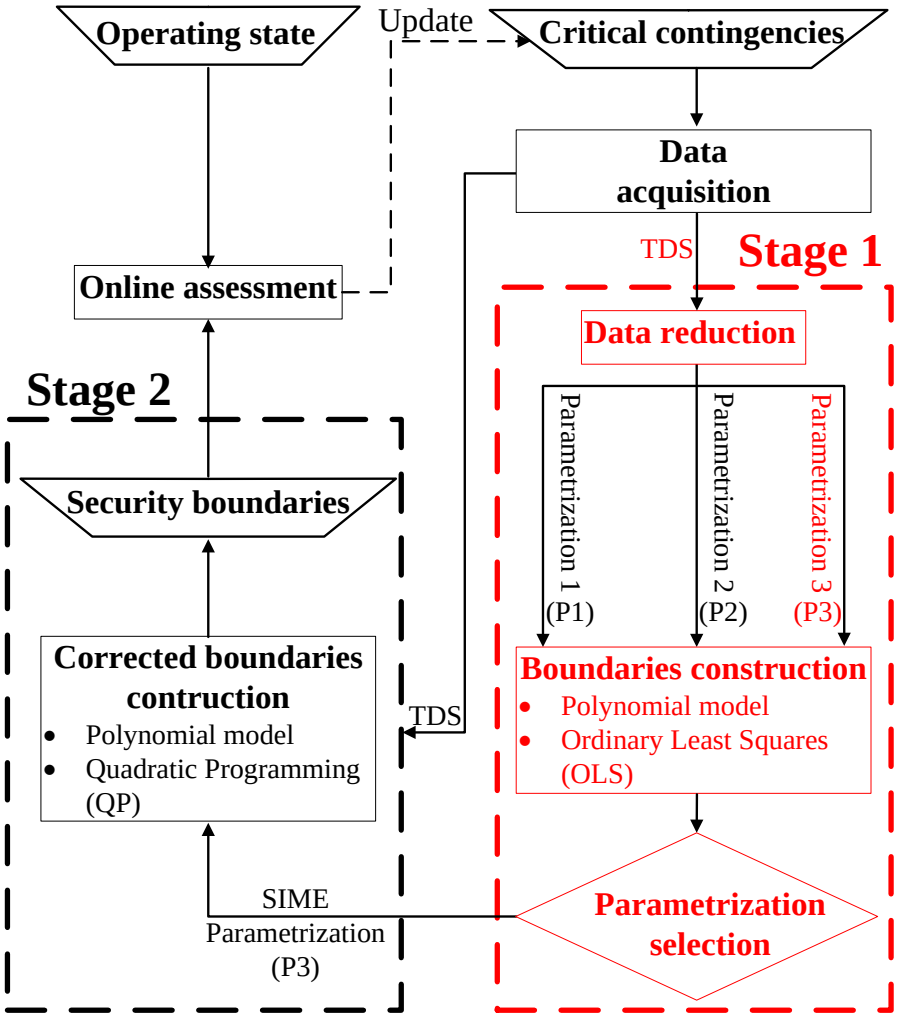

Figure 4.5: Current focus in the construction of the methodology

The expression (4.28) demonstrates that the polynomial coefficients will reflect on how sensitive the SIME distance δ_{SIME}^{DIST} is to changes in parameters. The value of certain polynomial coefficients would be larger if a power system is more sensitive to the changes in mechanical power of some specific generator (individual

terms in (4.28)) or certain groups of generators (cross terms in (4.28)). If some of the generators do not change their mechanical inputs with respect to changes in operating conditions, these generators will be excluded from the basin of the parameter-space. In these cases, the number of parameter-space dimensions in SIME-based parametrization P3 is lower than the total number of machines (n).

Special attention should be paid to the name of the newly proposed parametrization. The attribute “SIME-based" could be slightly misleading—the parametrization will use SIME as a tool, however, the methodology is based on the idea of parametrizing the stability boundary in polynomial form. Hence, it should be emphasized here that the denomination “SIME-based" is merely used to distinguish between P3 and the “ordinary" parametrizations over data sets (P1 and P2).

4.3.2 Performance comparison for proposed parametrizations

The performance of SIME-based parametrization will be demonstrated by returning once again to the simple two-machine infinite-bus system from Fig. 4.6.

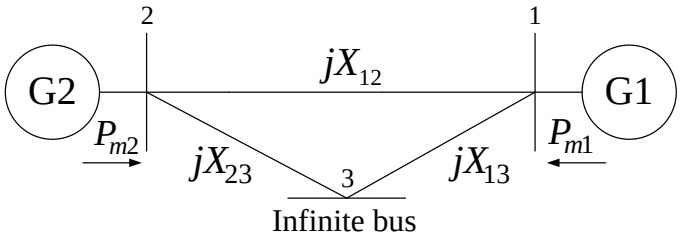

Figure 4.6: Two-machine infinite-bus test system

The same critical faults as before (three phase short circuits at generator buses) are simulated in order to construct the security boundaries by different parametrizations. For the newly introduced parametrization P3, the two steps in the boundary construction procedure are illustrated in Fig. 4.7 for the fault at bus 2. The first step (the uppermost picture of Fig. 4.7) estimates δ_{SIME}^{DIST} based on the varied parameters of importance. Since there are no loads in the test system, the mechanical power inputs of the two generators are chosen as the important parameters. The estimated δ_{SIME}^{DIST} are then used to construct the parameter-space basin that represents the sensitivity of SIME distance to the changes in the operating point (that are reflected by the variations in P_{m1} and P_{m2}). The downmost picture shows the relative error of estimates ($\Delta t_{cc} = t_{cc}^{est} - t_{cc}^{TDS}$) when 100% of TDS data is retained.

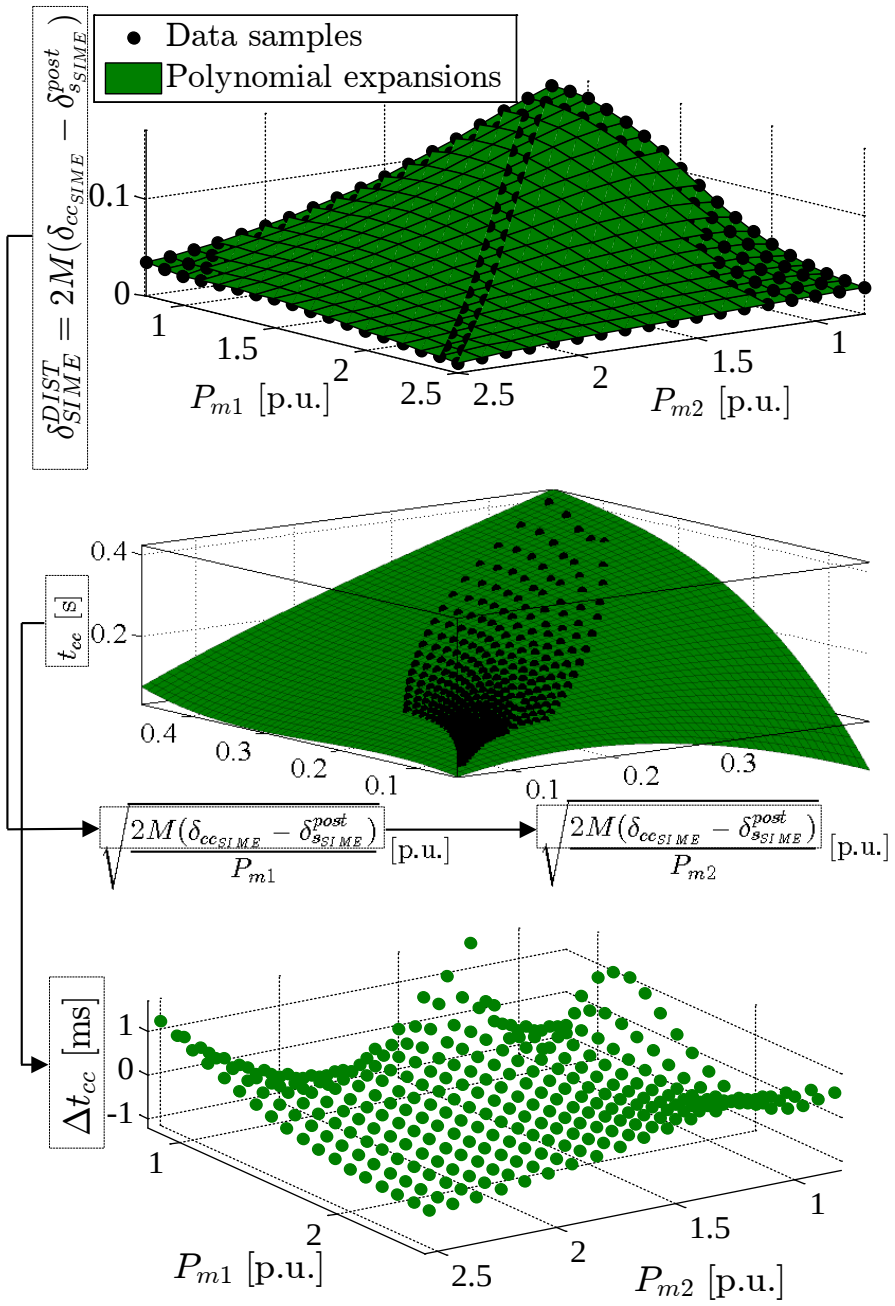

Figure 4.7: The two-step procedure of SIME parametrization P3

It is clear that two polynomial approximations are involved in the procedure. The first approximation predicts $\delta_{SIME}^{DIST_{est}}$ based on P1 and the important parameters that are subject to change. The second one (depicted in the middle picture of Fig. 4.7) identifies t_{cc}^{est} by employing P3. It should be outlined that $\delta_{s_{SIME}}^{pre}$ has been replaced by $\delta_{s_{SIME}}^{post}$ in the figure since there have not been any changes in the configuration. Some of the data samples (black circles) are not visible due to being located under the estimated surfaces. It is interesting to note how the parameter-space locations of the same sample points differ between P1 and P3. In P1, TDS samples form an equidistant network of points, i.e. the placement of samples is not affected by occurrences in the system. However, the distribution of samples is highly non-linear in P3. Sample points become more densely distributed as the system operates in more stressed conditions. The amount of stress is indicated not only by the inverse function of mechanical inputs (as in P2), but also by the critical distance of a SIME equivalent from the origin. Another important observation is that a mode of machine separation is known for the simulated points. This information is beneficial since it provides a good insight into how the machines fall out of synchronism for the operating points where t_{cc}^{est} is estimated. Table 4.1 shows how P3 performs in comparison to P1 and P2 when the same amount of data is retained. The polynomials are of the 3^{rd} order ($k = 3$) for all three parametrizations.

Table 4.1: Comparison of the performance of the parametrizations

Data reduction [%]	P1 REMV/SD [ms]	P2 REMV/SD [ms]	P3 REMV/SD [ms]
0	2.76/2.21	2.61/2.28	0.18/0.18
50	2.83/2.24	2.57/2.39	0.95/1.52
75	2.88/2.25	2.62/2.43	1.33/1.73
90	2.96/2.67	2.69/3.34	2.13/2.74

The comparison from Table 4.1 is based on the recorded error of estimates for the same operating points and both faults in all the cases of data reduction. The numbers in the table represent the average of the absolute value of the relative error (Relative Error Mean Value-REMV) and its Standard Deviation (SD). Apparently, P3 outperforms parametrizations P1 and P2, even when the amount of sample data is heavily reduced. Due to its theoretical foundation, SIME-based parametrization P3 distributes the data samples in a more optimal manner than the other two parametrizations that do not have a physical meaning.

4.4 Constrained SIME parametrization

Previously, Ordinary Least Squares (OLS) technique has been employed to estimate the optimal coefficients $\hat{a}$ in the three parametrizations that this thesis proposed. The objective of OLS is the smallest Relative Error Mean Value (REMV) of t_{cc} estimates. Stage 2 of the methodology construction (outlined in red color in Fig. 4.8) will further improve the selected, SIME-based parametrization P3.

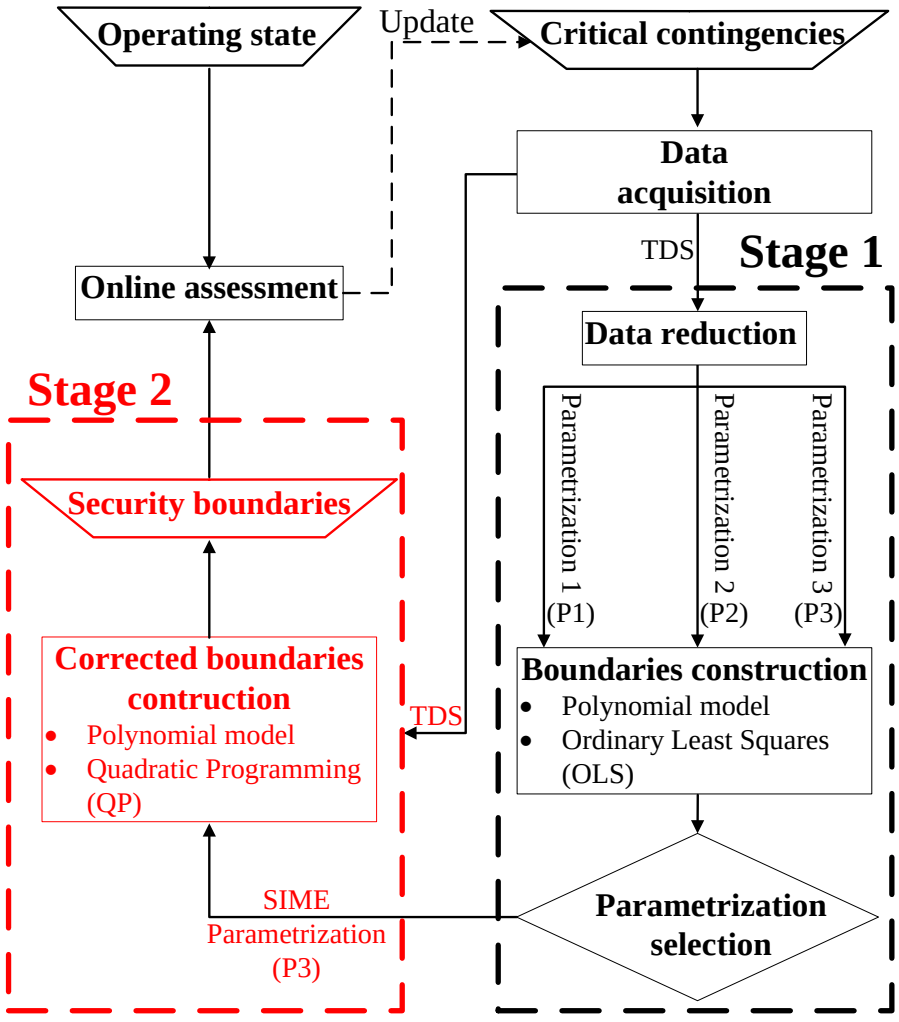

Figure 4.8: Constrained parametrization in methodology algorithm

The aim of Stage 2 is to enable SIME-based parametrization to provide conservative t_{cc} estimates while keeping the accuracy of the estimation as high as possible. In other words, the requirement is that the estimated critical clearing time ($\boldsymbol{t_{cc}^{est}} = \mathbf{H}_{\boldsymbol{SIME}}\hat{\boldsymbol{a}}_{\boldsymbol{corr}}$) has to be smaller than the critical clearing time obtained from TDS ($\boldsymbol{t_{cc}^{TDS}}$). This will be achieved by developing so-called "constrained SIME-based parametrization" which forces the unobserved random error to be positive in most of the cases. The constrained parametrization will make the correction of the coefficient vector $\hat{\boldsymbol{a}}_{\boldsymbol{corr}}$ by setting up a Constrained Least Squares (CLS) problem that should minimize the unobserved random error $\boldsymbol{\varepsilon}$ as:

$$\begin{aligned} &\min_{\boldsymbol{a}_{\boldsymbol{corr}}} \frac{1}{2}\|\boldsymbol{\varepsilon}(\boldsymbol{a}_{\boldsymbol{corr}})\|_2^2 && \text{such that} \quad \boldsymbol{\varepsilon}(\boldsymbol{a}_{\boldsymbol{corr}}) \geq \mathbf{0} \ \text{ or} \\ &\min_{\boldsymbol{a}_{\boldsymbol{corr}}} \frac{1}{2}\|\mathbf{H}_{\boldsymbol{SIME}}\boldsymbol{a}_{\boldsymbol{corr}} - \boldsymbol{t}_{\boldsymbol{cc}}\|_2^2 && \text{such that} \quad \mathbf{H}_{\boldsymbol{SIME}}\boldsymbol{a}_{\boldsymbol{corr}} \leq \boldsymbol{t}_{\boldsymbol{cc}}. \end{aligned} \tag{4.29}$$

The minimization problem from Eq. (4.29) can change its form by performing the following transformations:

$$\begin{aligned} &\frac{1}{2}\|\mathbf{H}_{\boldsymbol{SIME}}\boldsymbol{a}_{\boldsymbol{corr}} - \boldsymbol{t}_{\boldsymbol{cc}}\|_2^2 = \\ &= \frac{1}{2}(\mathbf{H}_{\boldsymbol{SIME}}\boldsymbol{a}_{\boldsymbol{corr}} - \boldsymbol{t}_{\boldsymbol{cc}})^T(\mathbf{H}_{\boldsymbol{SIME}}\boldsymbol{a}_{\boldsymbol{corr}} - \boldsymbol{t}_{\boldsymbol{cc}}) = \\ &= \frac{1}{2}(\boldsymbol{a}_{\boldsymbol{corr}}^{\boldsymbol{T}}\mathbf{H}^{\mathbf{T}}{}_{\boldsymbol{SIME}}\mathbf{H}_{\boldsymbol{SIME}}\boldsymbol{a}_{\boldsymbol{corr}} - 2\boldsymbol{t}_{\boldsymbol{cc}}^{\boldsymbol{T}}\mathbf{H}_{\boldsymbol{SIME}}\boldsymbol{a}_{\boldsymbol{corr}} + \boldsymbol{t}_{\boldsymbol{cc}}^{\boldsymbol{T}}\boldsymbol{t}_{\boldsymbol{cc}}), \end{aligned} \tag{4.30}$$

where the product $\boldsymbol{t}_{\boldsymbol{cc}}^{\boldsymbol{T}}\boldsymbol{t}_{\boldsymbol{cc}} = const.$ is a constant matrix. Adding a constant to an objective function does not affect the result of a minimization procedure. By applying this to the problem from (4.30), it is implied that $\boldsymbol{t}_{\boldsymbol{cc}}^{\boldsymbol{T}}\boldsymbol{t}_{\boldsymbol{cc}}$ can be neglected. The purpose of this action is to transform CLS problem (4.29) into a standard Quadratic Programming (QP) form [124]:

$$\begin{aligned} &\underset{\boldsymbol{x}}{\text{minimize}}\ \frac{1}{2}\mathbf{x}^{\mathbf{T}}\boldsymbol{Q}\mathbf{x} + \boldsymbol{c}^{\boldsymbol{T}}\mathbf{x} && \text{subject to} && \boldsymbol{A}\mathbf{x} \leq \boldsymbol{B}, \ \text{where:} \\ &\mathbf{x} = \boldsymbol{a}_{\boldsymbol{corr}}, && \text{and} && \boldsymbol{A} = \mathbf{H}_{\boldsymbol{SIME}}, \\ &\boldsymbol{Q} = \mathbf{H}^{\mathbf{T}}{}_{\boldsymbol{SIME}}\mathbf{H}_{\boldsymbol{SIME}}, && && \boldsymbol{B} = \boldsymbol{t}_{\boldsymbol{cc}}. \\ &\boldsymbol{c} = -\mathbf{H}^{\mathbf{T}}{}_{\boldsymbol{SIME}}\boldsymbol{t}_{\boldsymbol{cc}}. && && \end{aligned} \tag{4.31}$$

The QP problem from (4.31) will be solved in Matlab by the means of the active-set algorithm [125]. The result of the minimization procedure is a corrected coefficient

vector $\hat{\boldsymbol{a}}_{\boldsymbol{corr}}$. By importing $\hat{\boldsymbol{a}}_{\boldsymbol{corr}}$ into both steps of P3 parametrization from (4.26)-(4.27), some i^{th} estimate of t_{cc} is found by:

$$\text{Step 1: } \delta_{SIME_i}^{DIST_{est}} = \boldsymbol{H}_{\mathbf{P1}\boldsymbol{i}}(P_{inp_{1i}}, P_{inp_{2i}}, ..., P_{inp_{qi}})\hat{\boldsymbol{a}}_{\mathbf{P1}_{corr}} \tag{4.32}$$

$$\text{Step 2: } \quad t_{cc_i}^{est} = \boldsymbol{H}_{\boldsymbol{SIME_i}}(P_{m1_i}, P_{m2_i}, ..., P_{mn_i}, \delta_{SIME_i}^{DIST_{est}})\hat{\boldsymbol{a}}_{\mathbf{P3}_{corr}}. \tag{4.33}$$

The main motivation for imposing a constraint to unobserved random error was to make SIME parametrization competitive with UEP-oriented direct methods. As explained before, the energy of UEP is the lowest among the energies of points that are located on the manifold that is associated to the given type-1 UEP. Therefore, a certain level of conservativeness is expected in these methods, which is desirable in the assessment of short-term RAS. Constrained SIME-based parametrization will also possess this advantageous, conservative characteristic.

4.5 Constrained versus unconstrained SIME parametrization-results and comparison

This section will test the developed concept of constrained parametrization on both RNM ans SPM of a power system. It will also discuss the obtained results and draw the main conclusions related to the short-term RAS assessment study of this thesis.

4.5.1 Two-machine infinite-bus test system

The constrained SIME-based parametrization is now applied to the previously collected TDS data for Fault 1 and Fault 2 that occur at the generator buses of the test system from Fig. 4.6. The error of estimation is shown for both faults in Fig. 4.9 which keeps all 100% of data samples. The error is given in the relative form as $\Delta t_{cc} = t_{cc}^{est} - t_{cc}^{TDS}$ in [ms], which means that a negative error is a desirable one. The case from Fig. 4.9 depicts the effectiveness of the polynomial form in combination with the imposed constraint. The uppermost picture and the picture in the middle of Fig. 4.9 present the errors of estimation in Fault 1 and Fault 2, respectively. These first two pictures of Fig. 4.9 show the projection of error Δt_{cc} along P_{m1}-axis, while the bottom graph of Fig. 4.9 retains all three dimensions (P_{m1},P_{m2}, and Δt_{cc}). The error is less or equal to zero in all the estimated cases, i.e. QP solved the minimization problem adequately.

It is also important to investigate the effect of data reduction. The obtained results are summed up in Table 4.2 and Fig. 4.10 that compare the constrained and "ordinary" SIME-based parametrizations for different percentages of reduced data.

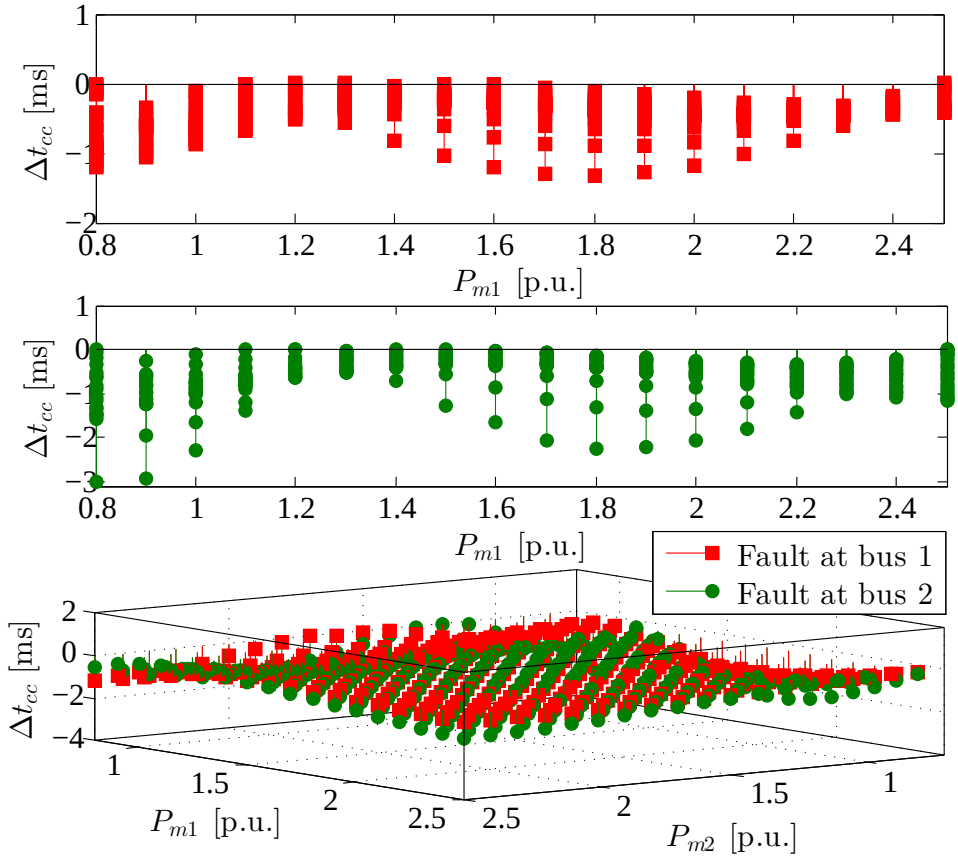

Figure 4.9: The error of constrained P3 when 100% of data is retained

Table 4.2: The comparison of performances of SIME-based parametrizations

Data reduction [%]	unconstrained P3 REMV/($\Delta t_{cc} \geq 0$) [%]	constrained P3 REMV/($\Delta t_{cc} \geq 0$) [%]
0	0.15/39.51	0.40/0.00
50	0.84/42.90	1.45/1.08
75	1.12/43.52	1.97/10.80
90	1.85/47.38	2.61/20.06

The numerical results from Table 4.2 represent the average of the two critical

faults when 100%, 50%, 25% and 10% of data are retained, respectively.

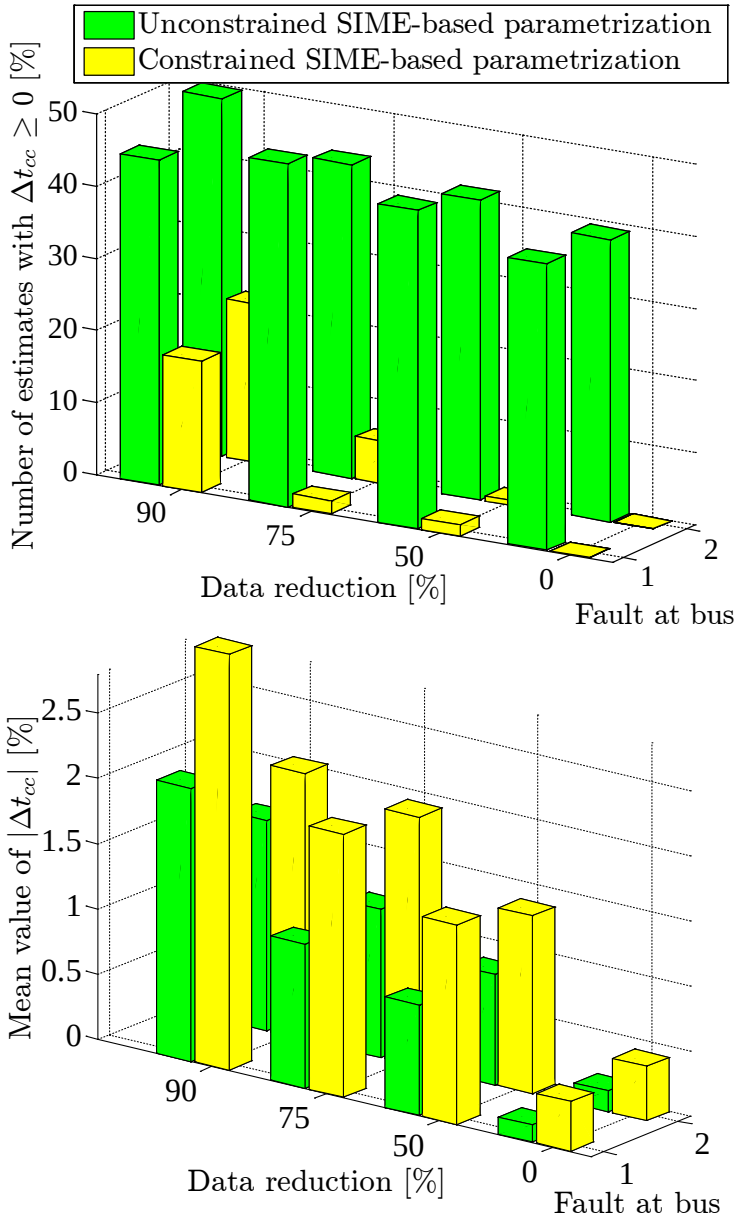

Figure 4.10: Effect of data reduction on the accuracy and conservativeness of P3

On the other hand, the graphical representation from Fig. 4.10 separates the results for Fault 1 and Fault 2. The yellow bars relate to constrained SIME parametrization while the green bars correspond to “ordinary" P3 that was based on OLS. From both Fig. 4.10 and Table 4.2 it is clear that the accuracy of P3 did not significantly deteriorate by imposing the constraint. It may also be observed that QP is highly efficient in achieving the conservativeness of estimates. Even for the case when 90% of TDS samples are eliminated from data set, constrained P3 parametrization places approximately 80% of estimates inside the security region (that is significantly more than 52.62% which is the result of unconstrained P3). The second index of performance, average error of estimation, raised from 1.85% to 2.61% after the constraint was applied. Hence, the accuracy decreased with less than 1%.

The trade-off between the number of over-estimates and the loss of accuracy implies that constrained SIME-based parametrization may become a valuable tool in short-term RAS assessment.

4.5.2 Three-machine system

The second case study tests the performance of SIME-based parametrization when the Structure Preserving Model (SPM) of power system from (2.17) is employed. The study will be carried out by using the three-machine system from Fig. 4.11 that is based on IEEE 9-bus test system. The transformers between the internal and terminal buses of the generators are not shown in the figure.

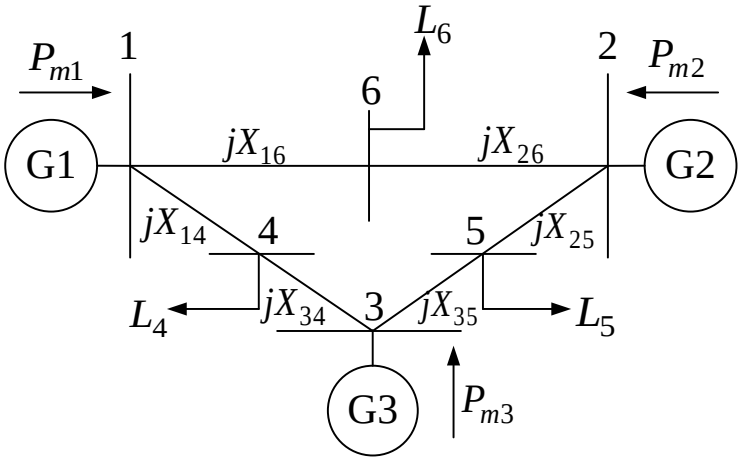

Figure 4.11: Three-machine test system

There are three loads in the system (connected at buses 4, 5 and 6) that will be given by the exponential model from Eq. (2.6) as:

$$P_{l_k} = P_{l_{k0}} \left(\frac{U_k}{U_{k_0}} \right)^{mp} \quad \text{and} \quad Q_{l_k} = Q_{l_{k0}} \left(\frac{U_k}{U_{k_0}} \right)^{mq}. \tag{4.34}$$

The load models can be varied by altering the exponents mp and mq.

The three phase short circuits very close to the generator terminal buses (buses 1, 2 and 3) are chosen as the critical faults in the case study. The faults are cleared without changes in configuration. Constrained SIME-based parametrization will construct one security boundary for each of the contingencies. Since loads exist in the system, the active powers of loads are now chosen as the parameters of importance to be used in Step 1 of the constrained SIME-based parametrization. The active powers of the loads at buses 5 ($P_{inp_1} = P_{l_{50}}$) and 6 ($P_{inp_2} = P_{l_{60}}$) are varied in order to perturb the operating point. Clearly, to be able to use constrained SIME parametrization, a certain dispatching plan needs to be known. Here, each of the generators will compensate for one third of the additional active load power. After estimating $\delta_{SIME}^{DIST_{est}}$, Step 2 provides the final dependency of t_{cc} from SIME-distance and the mechanical power inputs of the three generators (P_{m1}, P_{m2} and P_{m3}). Hence, Step 1 and Step 2 are here carried out in two and three-dimensional parameter-spaces, respectively:

$$\text{Step 1: } \delta_{SIME_i}^{DIST_{est}} = \boldsymbol{H_{P1i}}(P_{l_{50_i}}, P_{l_{60_i}})\hat{\boldsymbol{a}}_{\mathbf{P1}_{corr}} \tag{4.35}$$

$$\text{Step 2: } \quad t_{cc_i}^{est} = \boldsymbol{H_{SIME_i}}(P_{m1_i}, P_{m2_i}, P_{m3_i}, \delta_{SIME_i}^{DIST_{est}})\hat{\boldsymbol{a}}_{\mathbf{P3}_{corr}}. \tag{4.36}$$

The numerical results are provided in Table 4.3 in the form of average REMV and as the percentages of over-estimates for the three critical faults.

Table 4.3: The performance of constrained P3 for various load models

Load model	Data reduction [%] 0	50	75	90
Constant current REMV/($\Delta t_{cc} \geq 0$) [%]	0.20/0	0.43/0.82	0.52/1.44	0.54/3.40
Composite REMV/($\Delta t_{cc} \geq 0$) [%]	0.05/0	0.17/0.10	0.21/0.51	0.19/4.32
Constant impedance REMV/($\Delta t_{cc} \geq 0$) [%]	0.06/0	0.16/0.10	0.21/0.51	0.20/3.50

In this case study, the three types of loads have been applied: (i) constant current load ($mp = mq = 1$), (ii) composite load ($mp = 2$, $mq = 1$) and (iii) constant impedance load model ($mp = mq = 2$). The boundaries were constructed as the second order ($k = 2$) polynomials. The main observation is that the approach resulted in a high accuracy of estimates (largest REMV was 0.54%) and a small number of over-estimates (maximum 4.32% in the case of composite load). Neither the amount of reduced data or the type of the load seem to have significant negative effects on the results obtained by the constrained SIME-based parametrization.

4.5.3 Discussions and remarks

Before concluding this chapter, several general remarks will be extrapolated regarding the obtained results:

- TDS is chosen as the data acquisition tool due to its accuracy and unlimited applicability with respect to system modeling. Direct methods face various challenges when more complex power system models are employed. These challenges may be divided into three main classes that concern: (i) the possibility to construct an energy function, (ii) issues with convergence to a correct type-1 UEP in UEP-oriented approaches and (iii) inaccuracy of UEP-oriented approaches due to exit point being approximated by a type-1 UEP of importance.

- Polynomial models are capable to describe non-linear changes in the stability margin when a power system “moves around" in a parameter-space. These non-linear modifications of the stability margin have a certain, expected tendency—a fault needs to be cleared faster as a system becomes more stressed. Polynomials can work even when a mode of machine separation changes. Also, if the amount of data is insufficient to construct a boundary of a certain order, model validation procedure detects this and adjusts the order of the polynomial.

- SIME-based parametrization P3 is more accurate in comparison with the simple polynomial approximations over data sets (P1 and P2). The parameter-space basin has a physical meaning in P3.

- Quadratic Programming (QP) is highly efficient in placing the majority of estimates inside the short-term RAS security region.

- More parameter-space dimensions increased the accuracy of the estimation. This encourages the application of the methodology to larger systems. A large number of generators (parameter-space dimensions) in more complex systems may raise

concerns about over-fitting. However, not all n generators react to the changes in load or transmitted active power. A distribution of additional injected power among generators (power dispatching) is usually known to TSOs for critical faults that occur in certain areas of power system. The sensitivity of SIME-distance is of interest only with respect to the mechanical powers of those generators that participate in the power compensation. The proposed approach here offers another functionality—it may help identify which generators should compensate for the power change such that the system operates with the largest possible transient stability margin.

Chapters 3 and 4 are based on the work from [117, 121]. The two chapters presented the following solutions that are listed in Section 1.4 of Chapter 1:

1. (1.1S): The proposed constrained SIME-based parametrization is robust—it can be applied whenever it is possible to carry out TDS. The approach will, hence, retain the accuracy of TDS. The methodology, however, is based on a reduced number of data samples in comparison to conventional DSA. Since the boundaries are provided in analytical (polynomial) form, stability margins are also directly known for (other) operating points that were not included in the simulation set.

2. (1.2S): The security boundaries are non-linear, polynomial surfaces that enable short-term RAS assessment during large disturbances.

3. (1.3S): The dependency between t_{cc} and parameters is an invertible function. This is important since TSOs are usually interested in e.g. how much power can be transmitted via some weak corridor or delivered to a certain critical load area (for a known reaction time of a protective system t_{cl}). Inverted boundary equation provides the set of parameters that corresponds to t_{cl}.

Once the boundaries are constructed, stability margins can be directly determined during system operation (on-line) without the necessity to simulate faults. Based on the known operating state, TSOs have then the possibility to evaluate the risk of rotor angle instability, update the contingency list accordingly and change the operating point if e.g. (N-1) stability criterion is not met. All these characteristics indicate that the proposed method has a potential to become a useful tool for short-term RAS assessment in multi-machine power systems.

Chapter 5

Voltage Impasse Regions (VIR) in Power System Dynamics

Even the most sophisticated DSA tool for the analysis of transient stability counts on unlimited validity of the set of DAE. In the continuation, this thesis will investigate short-term dynamics in the presence of state-space areas where the set of DAE faces singularity due to load modeling. These "singularity areas" of state-space will be introduced as "Voltage Impasse Regions" (VIR) at which voltage causality is lost.

Dynamic Security Assessment (DSA) observes voltage stability as an ability of a power system to maintain voltages at all the buses within acceptable bounds after some (small or large) disturbance occurs. Disturbances that often cause voltage instability issues are trippings of transmission lines or losses of generation equipment [126]. In a worst-case scenario, a combination of a disturbance and the absence of sufficient voltage support may lead to a *voltage collapse*. Voltage collapse denotes a catastrophic sequence of events that (i) results in sudden and drastic decline of voltage profiles in significant portion of a power system or alternatively, (ii) leads to a blackout [55]. Voltage instability can also appear in the form of over-voltages [127] that may occur when, for instance: a network behaves in a capacitive manner; too large capacitive loads activate self-excitation of the synchronous generators or when the excess of the reactive power cannot be absorbed due to under-excitation limiters.

In voltage stability studies, the most common form of instability that occurs after a disturbance is a progressive fall of bus voltages that is typically driven by the dynamics of load restoration [128]. This restoration leads to an imbalance between the power of consumption on one side and the capacity of available transmission

and generating resources on the other side. In weak AC systems, voltage instability can also occur at HVDC terminals due to the reactive power load characteristic of the converters [129, 130]. The well-known self-restoration mechanisms along with other voltage-instability contributors may lead to a voltage collapse in both:

- **short-term** time scale (several seconds after a disturbance), as for the case of induction motors [131, 132] and HVDC converters and
- **long-term** voltage instability, which mostly concerns the dynamics of Load Tap Changers (LTCs) [133–136], OverExcitation Limiters (OELs) [137] and thermostatic loads [138]). The analysis of long-term dynamics may be of interest up to many minutes after a contingency has occurred.

All of the aforementioned issues are the topics of voltage instability analysis that is typically decoupled from Rotor Angle Stability (RAS) assessment. Nevertheless, a voltage collapse is essentially connected to rotor angle instability. It is well-known that the loss of synchronism between two groups of machines leads to a substantial voltage drop close to the electrical center of the network [54]. By resolving a RAS problem, voltages are restored with respect to a post-fault SEP.

However, by employing certain types of static load models while assessing RAS, a problem of different nature may arise. It could happen that not only voltages decline to unacceptably low levels—moreover, the voltage solutions could completely cease to exist if rotor angles reach certain points of state-space during transients. These points belong to the manifolds that are most often denoted in the literature as “impasse/singularity surfaces" [85, 86]. In that sense, this issue unifies RAS with voltage stability under a more general problem that deals with the global existence of solutions of DAE model [139]. In practice, “impasse surfaces" were used to explain the difficulties in TDS for the systems with non-impedance static load models [112]. However, an analytical formulation of the relationship between the two has not been identified so far. It appears that the effect of “impasse surfaces" has been overlooked by research community due to impasse surfaces not intersecting with power system equilibria [140]. The upcoming two chapters will show that this standpoint should be taken with precaution by performing a thorough analysis that introduces Voltage Impasse Regions (VIR). The task of the following study is to precisely define VIR as the state-space areas where voltage causality is lost (i.e. where voltage solutions cannot be found based on the DAE model) when some of the loads are given by constant-power and constant-current characteristics. Before defining the VIR, some basic state-space concepts first need to be revised from both static and dynamic point of view.

5.1 Static approach to voltage collapse

The subject of this study is the existence of plausible voltage solutions. This task is equivalent to the identification of voltage collapse in the static stability analysis. Since the voltage instability has been mostly associated to the loss of long-term equilibrium [126], static approaches heavily rely on the existence of a small signal stable, post-fault operating point and the size of static stability margin [141]. Voltage collapse is, in a fact, a loadability problem from the static point of view. Various sets of system parameters (different operating points) correspond to different sizes of load that can be supplied. If a system is more stressed due to increased load or a change in some other parameter, static distance to a voltage collapse (static voltage stability margin) typically decreases. In the framework of previously presented RAS region, parametric changes alter the location of a post-fault SEP (x_s^{post}), which affects both the shape of the stability region and short-term RAS margin (as sketched in Fig. 5.1). If changes in parameters would “push" a power system to its loadability limit, x_s^{post} would no longer exist and short-term RAS region would become an empty set.

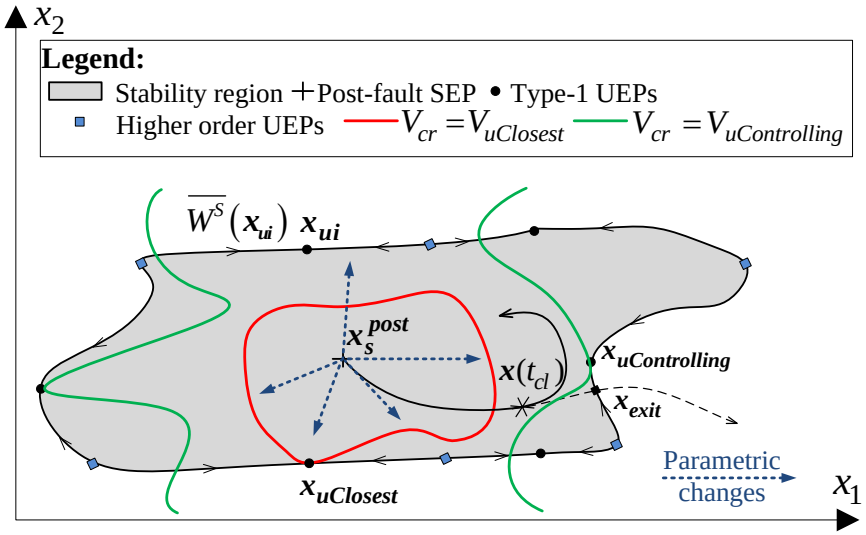

Figure 5.1: Changes in stability margin due to parametric changes

Hence, the existence of a stable post-fault equilibrium is a prerequisite for any other type of stability analysis. Consequently, an extensive amount of work has

been carried out in the past to address this issue. The common trait of these methods is that they re-assess the operating state with respect to some smooth deviations of control parameters ($\boldsymbol{p}$, that are typically load powers and generator schedulings) and stress level λ. By increasing the stress level along some direction $\boldsymbol{d}$, a set of actual parameters is given by:

$$\boldsymbol{p} = \boldsymbol{p_0} + \lambda \boldsymbol{d}, \tag{5.1}$$

where $\boldsymbol{p_0}$ is an initial parameter set. In order to identify the largest λ that does not lead to voltage collapse, most of the methods in static approach have focused on one of the two perspectives of the same concept:

1. **post-contingency power flow solvability** [142], which is a convenient characteristic to investigate due to power flow programs being widely available. Power flow utilizes the fact that the equations for finding a long-term equilibrium may be approximated by the set of network equations $\boldsymbol{G}$ where both short-term and long-term state-space variables have been eliminated:

$$\boldsymbol{0} = \boldsymbol{G}(\boldsymbol{y}, \lambda). \tag{5.2}$$

   By increasing λ, a loadability limit is determined as the point where power flow diverges. This is usually carried out by the Newton method and its modified versions [143–145] that have been specifically developed for this purpose. Another option is to employ optimization methods and calculate a loadability limit by the means of optimal power flow [146].

2. **occurrence of Saddle-Node Bifurcation (SNB)** [147, 148] that basically relies on a small-signal stability analysis which employs the complete DAE model:

$$\begin{aligned} \dot{\boldsymbol{x}} &= \boldsymbol{f}(\boldsymbol{x}, \boldsymbol{y}, \lambda); \\ \boldsymbol{0} &= \boldsymbol{g}(\boldsymbol{x}, \boldsymbol{y}, \lambda), \end{aligned} \tag{5.3}$$

   where the scaling factor λ has been taken into account. The dynamics of long-term variables are not included here, however, it is easy to expand the model and carry out the analysis in the similar fashion. The aim of the small-signal stability analysis in the given framework is to determine how far a system can move from a stable operating point by changing λ (and consequently, $\boldsymbol{p}$) and still remain in a stable state. For this purpose, DAE model (5.3) is linearized as:

$$\begin{bmatrix} \boldsymbol{\Delta}\dot{\boldsymbol{x}} \\ \boldsymbol{0} \end{bmatrix} = \boldsymbol{J} \begin{bmatrix} \boldsymbol{\Delta x} \\ \boldsymbol{\Delta y} \end{bmatrix}, \quad \text{where} \quad \boldsymbol{J} = \begin{bmatrix} \boldsymbol{f_x} & \boldsymbol{f_y} \\ \boldsymbol{g_x} & \boldsymbol{g_y} \end{bmatrix} \tag{5.4}$$

is the Jacobian matrix with sub-matrices $\boldsymbol{f}_x$, $\boldsymbol{f}_y$, $\boldsymbol{g}_x$ and $\boldsymbol{g}_y$ that consist of partial derivatives. This means that, for instance, $\boldsymbol{f}_x$ are the derivatives of the differential equations $\boldsymbol{f}$ with respect to state variables $\boldsymbol{x}$, $\boldsymbol{f}_y$ is the Jacobian matrix of $\boldsymbol{f}$ with respect to $\boldsymbol{y}$, etc. By assuming that $\boldsymbol{g}_y$ is non-singular, the linearized system from Eq. (5.4) can be reformulated into a more compact form as:

$$\boldsymbol{\Delta \dot{x}} = \boldsymbol{F}_x \boldsymbol{\Delta x}, \quad \boldsymbol{F}_x = \boldsymbol{f}_x - \boldsymbol{f}_y \boldsymbol{g}_y^{-1} \boldsymbol{g}_x. \tag{5.5}$$

Since it is the loss of equilibrium that is of interest, the aim of this class of methods is to identify at which loading levels a stable equilibrium undergoes an SNB and disappears. This observation is equivalent to finding where in the parameter-space $\boldsymbol{F}_x$ becomes singular (has a zero eigenvalue), which further implies the singularity of the "original" Jacobian matrix $\boldsymbol{J}$. Various approaches have emerged from the bifurcation concept during the previous decades in order to detect singularity conditions, monitor the distance to a voltage collapse and also to construct the strategies that "move a system away" from a voltage instability [149–156]. Different mathematical tools have been used to detect the singularity of $\boldsymbol{F}_x$ in these methods. Some examples of the tool-indices that have been employed are the eigenvalue closest to the origin, the minimum singular value and the determinant of matrix $\boldsymbol{F}_x$.

Nowadays, the voltage collapse is a well-investigated topic from the static point of view. The two established aspects regarding the existence of a stable equilibrium solution resulted in various classes of methods such are, for instance, the analysis of VQ curves [157], continuation [158–162] and optimization methods [163–166].

5.2 Stability of DAE model from dynamic point of view

The existing static methods are mostly based on power-flow and small-signal stability analysis. These approaches are not applicable if a power-system happens to be "pushed-away" further from an equilibrium point, which is the case after large disturbances. The reason is that static methods ignore the non-linearity of the differential part of DAE model. It has been already stated that it is not of interest to make static stability study more complicated (without necessity) by incorporating differential non-linearities. The static approach is therefore suitable when voltage solutions are assessed in long-term sense (at the times when large excursions of state and algebraic variables have damped out) after a contingency. However, this approach is no longer reliable in the case of short-term stability studies of large disturbances where non-linear dynamics play a significant role.

A large majority of research on voltage collapse are static studies [167]. The analysis of voltage stability in short-term scale needs to include fast-acting load components and HVDC converters [55]. Dynamic modeling of loads (induction motors and electronically controlled loads) [92, 168] and short circuits near load centers have been shown to be of particular importance. Recent short-term voltage stability studies have been mainly focused on cascade stalling of the induction motors and delayed voltage recovery after an occurrence of a large disturbance [84, 169]. The proposals for the problem solution often involve a temporary disconnection of motor loads [170] or an implementation of a properly placed dynamic VAR support in the system [171–173].

Nevertheless, the "standard" topics regarding short-term voltage stability do not look into the possibility of loosing a voltage solution along a dynamic trajectory. The existing methods focus on the values of the voltages, instead (i.e. voltages drop to unacceptably low values based on a solution obtained from DAE model). Now, the following questions are raised by this thesis: *Is it true that voltage solutions can indeed always be identified along a dynamic trajectory based on the DAE model?* In other words, could it happen that voltage solutions cease to exist along a trajectory in the similar manner as it happened in the case of static stability analysis (due to reaching loadability limits)? If this is a possibility, it is important to understand the underlaying mechanisms that induce the singularity of DAE along a transient trajectory since these types of events would affect any type of short-term stability assessment. If the global existence of coupled DAE solutions is not ensured, it means that voltage may collapse on a power swing in a phenomenon that is not triggered by any of the typical (previously mentioned) voltage instability contributors.

For the case of self-restoring loads, a usual standpoint is that voltage stability after large disturbance may be easily judged by the existence of a small-signal stable post-fault equilibrium (assuming that short-term RAS is satisfied). This is based on the fact that, in short-term time scale, the majority of self-restoring loads behave as static loads (constant impedance or constant current loads) which are considered as unable to induce voltage instability [174]. The induction motors react to large disturbances by restoring to almost constant power characteristic in the time frame of a second [168]. Nevertheless, very few works have actually inspected the stability of DAE model in the state-space that surrounds a stable post-fault equilibrium x_s^{post}. In these works researchers made efforts to connect a voltage collapse with the singularity of the algebraic part of DAE model [175]. The loss of DAE solution is possible if a dynamic trajectory faces a manifold that has been referred to as "impasse surface" [85] or "singularity surface" [86]. An impasse surface can be defined as a subset of state-space in which voltage causality is lost. The knowledge

about impasse surfaces has been used to justify well-known problems with the convergence of TDS in the presence of static, non-linear loads [112]. However, a structured study that explores the relationships between a voltage collapse, impasse surfaces and non-impedance loads has not been carried out so far [176].

The thesis will analyze the mechanisms that lead to a voltage collapse in seconds after some large disturbance due to the nonlinearity of loads. The aim is to derive an exact analytical description of an impasse surface with respect to different load models. A general idea is to observe an impasse surface as a set of points where some sort of bifurcation happens with rotor angles as bifurcation parameters. The term bifurcation will be avoided further on when describing this state-space phenomenon (in order to be in line with the standard terminology and not to make a confusion with the parameter-space bifurcation from the static analysis). When some large disturbance excites the dynamics of state-variables, algebraic variables change accordingly along a trajectory. Assuming that (i) a hyperbolic post-fault equilibrium is small-signal stable, (ii) a fault is cleared on time ($t_{cl} < t_{cc}$) and (iii) a trajectory does not intersect with an impasse surface, a power system will eventually settle at a post-fault stable equilibrium x_s^{post}. An alternative scenario corresponds to a stable post-fault equilibrium that has an impasse surface in its neighborhood, as shown in Fig. 5.2.

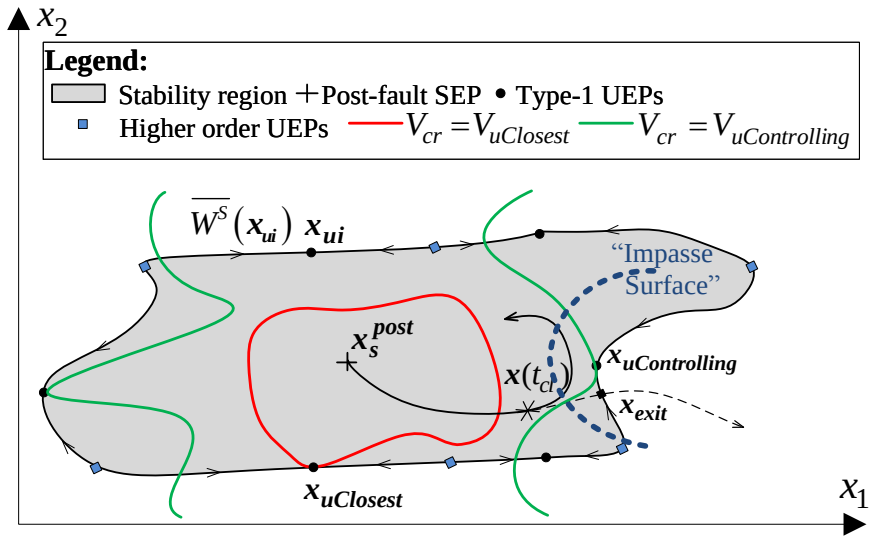

Figure 5.2: Impasse surface coinciding with RAS region

If a fault is cleared at such time that a post-fault trajectory encounters an impasse surface, voltage causality will be lost (state and algebraic variables will not behave according to the DAE model). The “destiny" of such system cannot be predicted which means that the only option is to avoid “risky" operating points that are surrounded by impasse surfaces. This is why it is important both to understand the fundamental nature of impasse surfaces and to precisely define under which circumstances an impasse surface will appear in the proximity of a stable x_s^{post}.

5.3 Impasse surface for DAE model

Once a large disturbance is cleared, the system of DAE equations will behave according to the initial state at the time of fault clearing t_{cl} and the configuration of the post-fault system. The existence of an impasse surface will hence be examined with respect to parameters $\boldsymbol{p}$ of a post-fault system, i.e. the post-fault dynamics are of interest:

$$\dot{\boldsymbol{x}} = \boldsymbol{f_{post}}(\boldsymbol{x}, \boldsymbol{y}, \boldsymbol{p}); \quad \boldsymbol{0} = \boldsymbol{g_{post}}(\boldsymbol{x}, \boldsymbol{y}, \boldsymbol{p}); \quad t_{cl} \leq t < \infty. \tag{5.6}$$

Here it is assumed that a post-fault equilibrium x_s^{post} is small-signal stable which means that it is possible to find a non-zero t_{cl} that guarantees short-term RAS. For such case, it is always possible to identify a critical clearing time t_{cc} if an impasse surface is not located inside a short-term RAS region. To ensure that a singularity is not going to be encountered along a post-fault trajectory, a location of an impasse surface should be analytically defined as a function of state-space variables. This concept is further clarified with the help of the Implicit Function Theorem that is applied to the general DAE model of a power system.

5.3.1 Implicit Function Theorem

The Implicit Function Theorem has been used in the framework of power systems to derive sufficient conditions for a local transformation of the DAE model (5.6) into the system of Ordinary Differential Equations (ODE) [141]:

$$\dot{\boldsymbol{x}} = \boldsymbol{F_{post}}(\boldsymbol{x}, \boldsymbol{p}), \quad t_{cl} \leq t < \infty. \tag{5.7}$$

Algebraic equations and variables are eliminated from the set of ODE. This is exactly what was done when the Structure Preserving Model (SPM) was transformed into the Reduced Network Model (RNM) of a power system in Subsection 2.3.2 of Chapter 2. This example has demonstrated that the reduction of the SPM to an ODE set is

always possible when all the loads are of the static, constant impedance type. Based on the Implicit Function Theorem, a locally unique and smooth function $\boldsymbol{F_{post}}$ can be identified for all the cases when the algebraic Jacobian $\boldsymbol{g_{post_y}} = \partial \boldsymbol{g_{post}}/\partial \boldsymbol{y}$ is non-singular. A possible singularity of $\boldsymbol{g_{post_y}}$ at some state-space locations $\hat{x}$ implies that the algebraic (voltage) solutions do not exist based on the DAE model. At these points, voltage causality is lost and DAE model cannot be used to describe system dynamics [177, 178]. From the simulation point of view, this situation is expected to be manifested in the form of numerical instability (non-convergence). It is risky to operate in the states where a dynamical behavior after a contingency is unpredictable. It is important to understand the basic mechanisms that introduce impasse surfaces in order to minimize the risk of a singularity-induced voltage collapse along a post-fault trajectory.

5.3.2 Impasse surface as a state-space area- "Voltage Impasse Region (VIR)"

The following study attempts to take a step forward by deriving the mathematical characterization for the set of points where the voltage causality is lost due to the presence of non-linear loads. This subset of state-space (illustrated in Fig. 5.3) will be as now on denoted as Voltage Impasse Region(s) (VIR) for the DAE model.

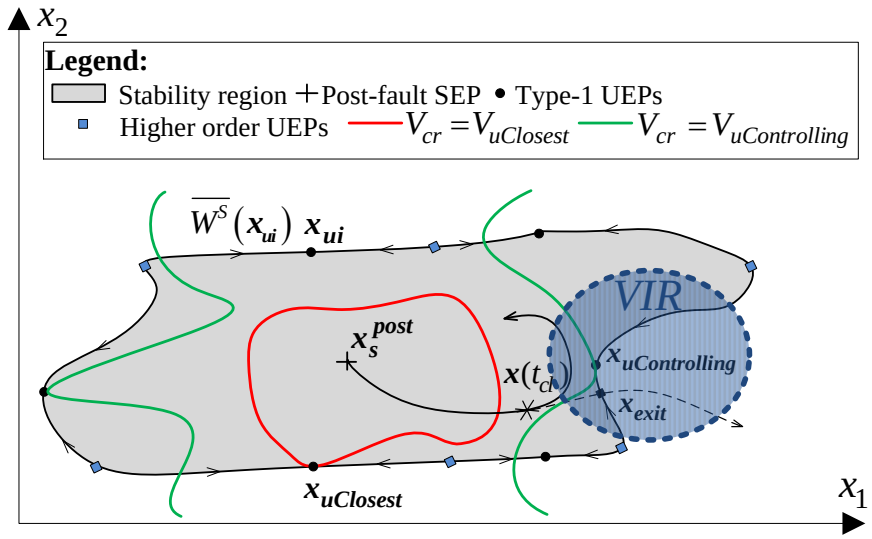

Figure 5.3: Intersection of a Voltage Impasse Region with short-term RAS region

The investigation will focus on finding the conditions that need to hold such that a VIR appears as an area of the state-space that can interfere with short-term stability assessment. The idea is to be able to "map" a short-term RAS region of any operating point by distinguishing between "safe" areas and VIR. The simplified flowchart of the study is depicted in Fig. 5.4.

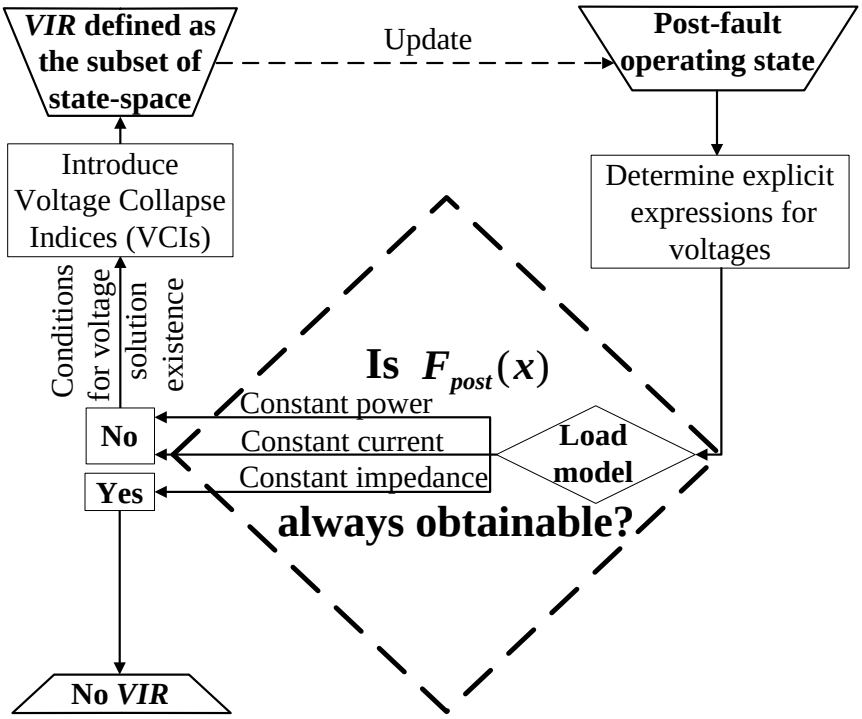

Figure 5.4: Flowchart of the study/derivation process

The conceptual description of the steps for finding VIR is given in the sequel:

1. Initially, a small signal stable post-fault operating state x_s^{post} is calculated based on the known, corresponding parameters $\boldsymbol{p}$;

2. Mathematical transformations are then carried out in order to determine the solutions for voltages as the explicit functions of state-variables (and other constant parameters);

3. The type of static load will be varied between constant power, constant current and constant impedance characteristics. The nature of voltage solutions is

carefully analyzed for each load model to investigate if $\boldsymbol{F}_{post}$ is always possible to construct without limitations;

4. If the previous points conclude that the existence of voltage solution is constrained (state-space singularity areas of $\boldsymbol{g}_{post_y}$ are non-zero sets), appropriate Voltage Collapse Indicators (VCIs) will be defined based on the fundamental requirement for the magnitude of a phasor;

5. By the virtue of VCIs, VIR is introduced as the union of points in state-space at which voltage causality is lost.

The proposed algorithm would provide an easy access to VIR size and location by using only the information about steady-state of the post-fault system. In other words, one does not need to carry out a dynamic simulation to determine whether a VIR exists in the state-space neighborhood of x_s^{post}. The on-line knowledge about the proximity to a VIR could be a powerful tool against short-term voltage collapse. To get familiar with the concept of VIR, the thesis first provides a simple example for which it is straightforward to derive and present the conditions for the existence of voltage solution in an intuitive manner.

5.4 Analytical example for an SMIB system with constant power load

Let the SMIB system have the set up that is shown in Fig. 5.5. The purpose of the example is to find the relationship between the state-space location and the existence of a solution for load voltage $\bar{U}_l = U_l \angle \theta_l$ when the load is of static, non-linear type. An example of such load is the constant power load that will be employed in this analytical study.

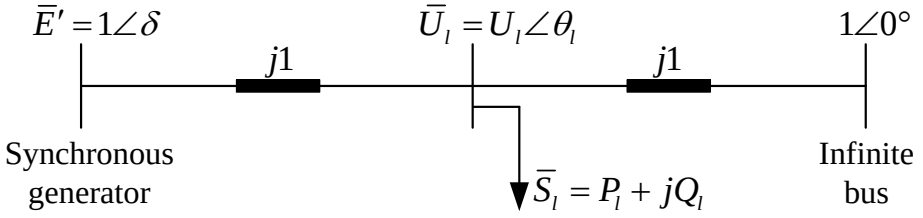

Figure 5.5: A version of SMIB system for the analysis of load voltage solution

The unity parameters ($\bar{Z}_L = jX_L = j1$ [p.u.]) are used for the two identical, purely reactive line impedances where shunt admittances are neglected. The load is of static, constant power type, i.e. the power $\bar{S}_l$ remains constant regardless of the changes in the load voltage $\bar{U}_l$. For simplicity purposes, the internal bus of the machine is connected directly to the network. The machine is represented by the classical model. It is assumed that the solution of the power flow results in the magnitude of the generator voltage being equal to 1 [p.u.]. When the phasor of the generator voltage $\bar{E}' = 1\angle\delta$ is shown, the rotor angle of the generator is purposely denoted as a variable δ due to the fact that its value would change once dynamics are triggered. On the other hand, the magnitude of the internal generator voltage remains constant for the case of classical model. The angle of the infinite bus with fixed voltage $\bar{U}_N = 1\angle 0^\circ$ is used as the reference for δ.

From the Kirchhoff's current law [179] for the load bus it follows that:

$$\frac{1-\bar{U}_l}{j} + \frac{1\angle\delta - \bar{U}_l}{j} = \left(\frac{\bar{S}_l}{\bar{U}_l}\right)^* \Rightarrow 2j\bar{U}_l - j(1+1\angle\delta) = \frac{\bar{S}_l^*}{\bar{U}_l^*}. \tag{5.8}$$

The multiplication of both sides of Eq. (5.8) by $\bar{U}_l^*/j$ (for $\bar{U}_l \neq 0$) results in the phasor of the load voltage being expressed as:

$$2U_l^2 - \bar{U}_l^*(1+1\angle\delta) = -j\bar{S}_l^* \Rightarrow \bar{U}_l^* = \frac{2U_l^2 + j\bar{S}_l^*}{1+1\angle\delta} \ \wedge \ \bar{U}_l = \frac{2U_l^2 - j\bar{S}_l}{1+1\angle-\delta}. \tag{5.9}$$

A simple way to solve Eq. (5.9) for the magnitude of the voltage is to multiply the load voltage with its conjugate:

$$\begin{aligned} U_l^2 = \bar{U}_l\bar{U}_l^* &= \frac{(2U_l^2 + j\bar{S}_l^*)(2U_l^2 - j\bar{S}_l)}{(1+1\angle\delta)(1+1\angle-\delta)} \\ &= \frac{4U_l^4 + S_l^2 + j2U_l^2(\bar{S}_l^* - \bar{S}_l)}{2+1\angle\delta+1\angle-\delta} \\ &= \frac{4U_l^4 + S_l^2 + 4U_l^2Q_l}{2+2\cos\delta}, \ \text{ since } \ \bar{S}_l^* - \bar{S}_l = -2jQ_l. \end{aligned} \tag{5.10}$$

By reorganizing Eq. (5.10), a resulting biquadratic equation with respect to the voltage magnitude is obtained as:

$$U_l^4 + \left(Q_l - \frac{1}{2} - \frac{\cos\delta}{2}\right)U_l^2 + \frac{S_l^2}{4} = 0. \tag{5.11}$$

In the context of VIR, it is of interest to analyze the voltage magnitude solution when δ is changed. The basic requirement for the magnitude of any phasor is that

it has a positive, real value. Biquadratic equation (5.11) is at the same time the quadratic equation where U_l^2 is the independent variable. Hence, the sufficient condition for having at least one feasible solution for the magnitude is that the discriminant D of Eq. (5.11) is larger or equal to zero. The opposite case (in which the discriminant D is less than zero) yields the pair of complex-conjugated solutions for U_l^2. The set of angles δ that corresponds to the case of negative discriminant D is actually the VIR. The condition for the non-existence of the voltage solution is then written in the following form:

$$\begin{aligned} D = (Q_l - \phi)^2 - S_l^2 < 0 \Rightarrow \\ \Rightarrow Q_l^2 - 2\phi Q_l + \phi^2 - P_l^2 - Q_l^2 < 0, \text{ where } \phi = \frac{1+\cos\delta}{2}. \end{aligned} \tag{5.12}$$

In order to simplify the condition for the non-existence of load voltage solution, Eq. (5.12) is divided by ϕ. The variable ϕ is always positive except for the case $\delta = \pi$ [rad.] when $\phi = 0$. At the point when the rotor angle reaches 180° or π [rad.] synchronism has already been lost. Hence, it is safe to divide Eq. (5.12) by ϕ such that the condition for the voltage solution non-existence is written as:

$$-2\phi Q_l + \phi^2 - P_l^2 < 0 \Rightarrow -2Q_l + \phi - \frac{P_l^2}{\phi} < 0 \Rightarrow \boxed{Q_l > \frac{\phi}{2} - \frac{P_l^2}{2\phi}}. \tag{5.13}$$

The condition from Eq. (5.13) can also be rewritten in the terms of rotor angle δ:

$$Q_l > \frac{1+\cos\delta}{4} - \frac{P_l^2}{1+\cos\delta}. \tag{5.14}$$

Figure 5.6 illustrates the condition (5.13) for the voltage solution existence by marking the areas without voltage causality in gray color. The figure obviously relates to some general P_l, Q_l and $\phi = (1+\cos\delta)/2$. The area of quadrant I that has been coloured in blue is important due to the presumed direction of load power (i.e. load typically consumes active and reactive power which means $P_l, Q_l > 0$). The blue parabola $Q_l = \phi/2 - P_l^2/2\phi$ in Fig. 5.6 is the boundary for voltage solution existence that is shown in a general form for some set of system parameters. It is clear that the operation inside the gray area beyond blue parabola (impasse surface) is not possible since it does not correspond to any static, physical state of the system. Any steady-state operating point that lies on the blue parabola yields that the two feasible voltage solutions of Eq. (5.11) merge as:

$$U_{l_{1,2}} = \sqrt{\frac{-(Q_l-\phi) \pm \sqrt{(Q_l-\phi)^2 - S_l^2}}{2}} \xrightarrow{(Q_l-\phi)^2 - S_l^2 = 0} U_l^{lim} = \sqrt{\frac{\phi - Q_l}{2}}. \tag{5.15}$$

Such an operating state that corresponds to U_l^{lim} in a fact represent a static loadability limit. Once the limit is crossed (after a load increase, for instance), the upper and the lower voltage solutions cease to exist due to becoming complex numbers.

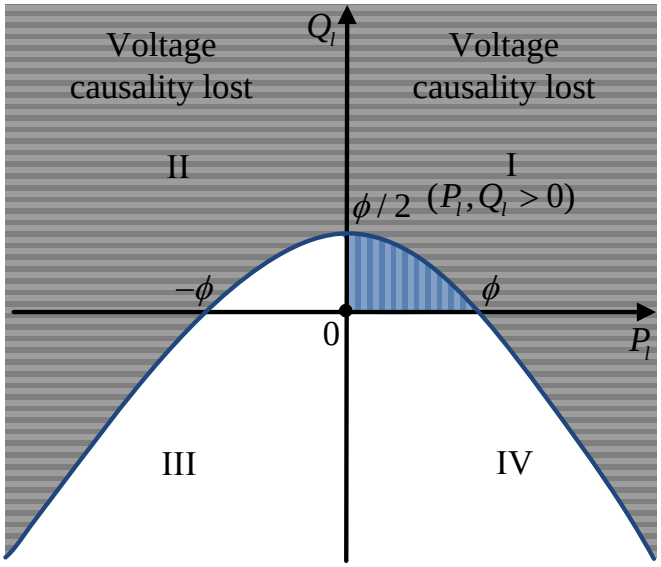

Figure 5.6: The areas where $\bar{U}_l$ solutions do not exist

Now, let an operating point OP (given by $\bar{S}_l^{OP} = P_l^{OP} + jQ_l^{OP}, \delta^{OP}$) belong to the safe, white area under the parabola, as shown in Fig. 5.7.

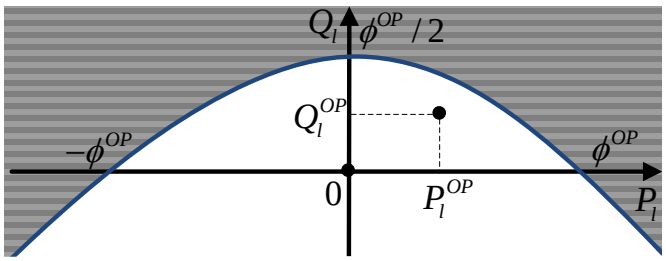

Figure 5.7: A stable operating point from the static analysis point of view

Angle δ^{OP} is assumed to be identified as an output of the power flow where $\bar{S}_l^{OP}$ is specified. For stable steady-states, the rotor angle is usually very close to zero, i.e. $\delta^{OP} \sim 0°$. The specific value of ϕ that corresponds to δ^{OP} is given by

$\phi^{OP} = (1 + \cos\delta^{OP})/2$ which further determines the intersections of the blue parabola with P_l and Q_l axes in Fig. 5.7. By looking into Table 5.1 that maps several values of δ into ϕ, it may be observed that by changing δ in the range $(-\pi, \pi)$ [rad.] $\Leftrightarrow (-180°, 180°)$ ϕ decreases as δ moves away from $0°$ (and $\delta^{OP} \sim 0°$).

Table 5.1: The mapping of values between δ and ϕ

δ	$-180°$	$-90°$	$-60°$	$0°$	$60°$	$90°$	$180°$
ϕ	0	$\frac{1}{2}$	$\frac{3}{4}$	1	$\frac{3}{4}$	$\frac{1}{2}$	0

The changes of δ may as well be interpreted as the oscillations of the rotor angle that occur along a dynamic trajectory. So, what are the physical implications of this example in the terms of dynamics? Inspection of the curves from Fig. 5.8 helps in answering this question. When the rotor angle δ starts oscillating due to some large disturbance, the blue curve will move correspondingly. Let the "movable" ϕ that comes from the post-fault dynamics of δ be denoted as ϕ^{dyn}.

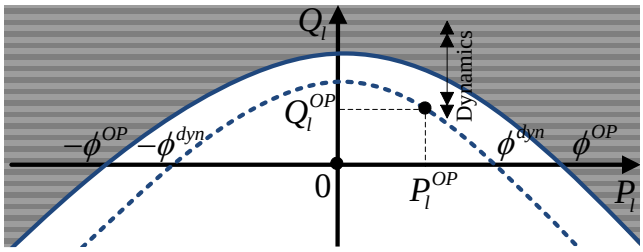

Figure 5.8: The loss of voltage causality due to dynamics

Assuming that a large disturbance has been cleared without changes in configuration, an appropriate fault clearing time would lead to the settling at the stable OP (if the dynamical system is damped). This statement would hold if the loss of synchronism was the only active instability mechanism here. If the rotor angle moves far enough from the initial state, it may as well happen that parabola $(Q_l - \phi^{dyn})^2 - S_l^2 = 0$ (blue, dashed curve in Fig. 5.8) "meets" the point (P_l^{OP}, Q_l^{OP}). This means that two distinct voltage load solutions have merged as the dynamical state evolved. Further increase in δ results in the loss of voltage causality due to entering an area that has been introduced in this thesis as a Voltage Impasse Region (VIR).

It is undefined what happens next once a system reaches a VIR. Nevertheless, this simple example yielded several interesting observations:

- VIR is a “dynamic equivalent" to static loadability. Both phenomena originate from the loss of possibility to express load voltage $\bar{U}_l$ as a function of rotor angle δ. In both cases, the magnitude of the upper voltage solution decreases until the point U_l^{lim} where it merges with the lower voltage solution. The difference is that the static loadability occurs due to some variation in system parameters (e.g. load powers) while a VIR is encountered during dynamics as rotor angle δ changes;

- For the constant power load model, a loss of voltage causality along a trajectory is related to the power characteristic that cannot “adjust" to the changes of parabola $(Q_l - \phi^{dyn})^2 - S_l^2 = 0$ during dynamics. It is also important to outline that even before the voltage solution is completely lost, the drop in voltage profiles could be significant;

- Short-term RAS assessment should consider VIR as a threat to the existence of voltage solutions along a dynamical trajectory.

The intention of this example was to provide an insight into the basic mechanisms that lead to the load-modeling-related loss of voltage causality during dynamics. The constant power load is one type of non-linear static load. A similar analytical example based on SMIB system could have been established for the constant current load. However, this will be done in a more general way. The concept of VIR will now be expanded to a multi-machine power system model such that the effect of different types of static load can be investigated.

5.5 System model for the study of VIR

The idea of VIR will now be generalized by using an n-machine ($i = 1, ..., n$) power system model that is similar to the one from Section 2.2. The generators are given by the classical model. Out of total N number of loads ($k = 1, ..., N$), $(N - 1)$ loads are considered as constant impedances $\bar{Z}_{l_m}$ ($m = 1, ..., N \wedge m \neq L$). One load that is connected at some bus L will be represented by different static load models (namely, constant power, constant current or constant impedance load models). Such a system is sketched in Fig. 5.9. The intention here is to understand the mechanism of VIR appearance by outlining the influence of one load that has

non-impedance characteristic. It is important to carry out this step before any further analysis about cumulative effect of multiple non-linear loads.

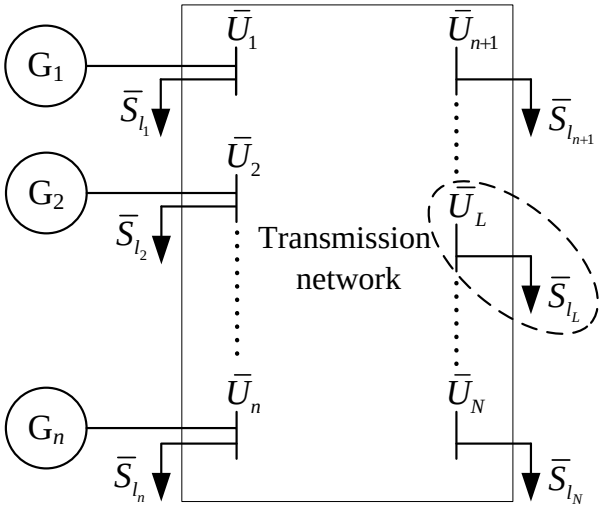

Figure 5.9: Power system model for the study of load modeling effects on VIR

The set of DAE that describes the dynamic behavior of this system has been previously defined in Chapter 2 by Eqs. (2.13) and (2.14). Following the Implicit Function Theorem, the transformation of DAE into the form of reduced ODE system (2.25) is possible if voltage causality is maintained in the whole state-space:

$$\text{DAE}\begin{cases}\dot{\boldsymbol{\delta}} = \boldsymbol{f}_{post_\delta}(\boldsymbol{\omega});\\ \dot{\boldsymbol{\omega}} = \boldsymbol{f}_{post_\omega}(\boldsymbol{\delta},\boldsymbol{\omega},\boldsymbol{U},\boldsymbol{\theta});\\ \boldsymbol{0} = \boldsymbol{g}_{post}(\boldsymbol{\delta},\boldsymbol{U},\boldsymbol{\theta});\end{cases} \quad \xrightarrow[\boldsymbol{\theta}(\boldsymbol{\delta})]{\boldsymbol{U}(\boldsymbol{\delta})} \quad \left.\begin{array}{l}\dot{\boldsymbol{\delta}} = \boldsymbol{F}_{post_\delta}(\boldsymbol{\omega});\\ \dot{\boldsymbol{\omega}} = \boldsymbol{F}_{post_\omega}(\boldsymbol{\delta},\boldsymbol{\omega}).\end{array}\right\}\text{ODE} \tag{5.16}$$

i.e. if the functions $\boldsymbol{U}(\boldsymbol{\delta})$ and $\boldsymbol{\theta}(\boldsymbol{\delta})$ are well defined for each $\boldsymbol{\delta}$ since the algebraic equations do not depend on $\boldsymbol{\omega}$ (directly). If the exponents that correspond to the active and reactive powers from Eq. (2.6) are set to be equal ($mp = mq = ms$), the complex power of the load at bus L can be written as:

$$\begin{aligned}\bar{S}_{l_L} = P_{l_L} + jQ_{l_L} &= P_{l_{L0}}\left(\frac{U_L}{U_{L_0}}\right)^{mp} + jQ_{l_{L0}}\left(\frac{U_L}{U_{L_0}}\right)^{mq}\\ &= (P_{l_{L0}} + jQ_{l_{L0}})\left(\frac{U_L}{U_{L_0}}\right)^{ms} = \bar{S}_{l_{L0}}\left(\frac{U_L}{U_{L_0}}\right)^{ms},\end{aligned} \tag{5.17}$$

where $ms = 0$, $ms = 1$ and $ms = 2$ represent the constant power, constant current and constant impedance load characteristics, respectively. Equation (5.17) describes how the load complex power $\bar{S}_{l_L}$ changes from its initial value $\bar{S}_{l_{L0}}$ as the load voltage magnitude U_L evolves from U_{L_0}, as it happens in the case of dynamics. The transformation from Eq. (5.16) says that it is necessary to determine the closed form expressions for voltages of the generator terminal and load buses as the functions of generator rotor angles.

Now, let a slightly modified admittance matrix $\mathbf{Y'}$ represent the original admittance matrix of the network $\mathbf{Y_{BUS}}$ whose diagonal entries are expanded for the load admittances and the associated admittances of the generators as:

$$\mathbf{Y'}=\mathbf{Y_{BUS}}+\begin{bmatrix} \frac{1}{jX'_{d1}}+\frac{1}{\bar{Z}_{l_1}} & 0 & \dots & 0 & \dots & 0 & 0 \\ 0 & \frac{1}{jX'_{d2}}+\frac{1}{\bar{Z}_{l_2}} & \dots & 0 & \dots & 0 & 0 \\ \vdots & \vdots & \ddots & \vdots & \ddots & \vdots & \vdots \\ 0 & 0 & \dots & \frac{1}{\bar{Z}_{l_{(n+1)}}} & \dots & 0 & 0 \\ \vdots & \vdots & \ddots & \vdots & \ddots & \vdots & \vdots \\ 0 & 0 & \dots & 0 & \dots & \frac{1}{\bar{Z}_{l_{(N-1)}}} & 0 \\ 0 & 0 & \dots & 0 & \dots & 0 & \frac{1}{\bar{Z}_{l_N}} \end{bmatrix}. \quad (5.18)$$

It can equally be said that in the matrix (5.18), $(i,i)^{th}$ and $(m,m)^{th}$ entries of $\mathbf{Y_{BUS}}$ are expanded for the admittances $1/jX'_{di}$ and $1/\bar{Z}_{l_m}$ that are directly connected to those buses. For instance, the first element along $\mathbf{Y'}$ diagonal is $\mathbf{Y'}(1,1) = \mathbf{Y_{BUS}}(1,1) + 1/jX'_{d1} + 1/\bar{Z}_{l_1}$ and another element of the new admittance matrix that corresponds to a purely load bus N is $\mathbf{Y'}(N,N) = \mathbf{Y_{BUS}}(N,N) + 1/\bar{Z}_{l_N}$. The transformation of the admittance matrix is carried out in order to establish a direct connection between the internal generator voltages, voltages at the terminals of the generators and the load bus voltages in a compact form. The inverse of the new admittance matrix $\mathbf{Y'}$ is introduced as the impedance matrix $\mathbf{Z}$:

$$\mathbf{Z} = \mathbf{Y'}^{-1}, \quad (5.19)$$

where the element at the $(u,v)^{th}$ position of matrix $\mathbf{Z}$ will be denoted as $\bar{Z}_{uv}$.

In the similar fashion as in the analytical example from Section 5.4, the system voltages can be expressed by simply following the Kirchhoff's current law. The idea

is to "keep" the load at bus L outside of the matrix $\mathbf{Y}'$ by modeling its influence via current $(\bar{S}_{l_L}/\bar{U}_L)^*$ that is drawn by the load. After a few simple algebraic manipulations, it can easily be shown that the following matrix equation holds:

$$\begin{bmatrix} \bar{E}'_1/(jX'_{d1}) \\ \bar{E}'_2/(jX'_{d2}) \\ \vdots \\ \bar{E}'_n/(jX'_{dn}) \\ 0 \\ \vdots \\ -(\bar{S}_{l_L}/\bar{U}_L)^* \\ \vdots \\ 0 \end{bmatrix} = \mathbf{Y}' \begin{bmatrix} \bar{U}_1 \\ \bar{U}_2 \\ \vdots \\ \bar{U}_n \\ \bar{U}_{n+1} \\ \vdots \\ \bar{U}_L \\ \vdots \\ \bar{U}_N \end{bmatrix} \Rightarrow \begin{bmatrix} \bar{U}_1 \\ \bar{U}_2 \\ \vdots \\ \bar{U}_n \\ \bar{U}_{n+1} \\ \vdots \\ \bar{U}_L \\ \vdots \\ \bar{U}_N \end{bmatrix} = \mathbf{Z} \begin{bmatrix} \bar{E}'_1/(jX'_{d1}) \\ \bar{E}'_2/(jX'_{d2}) \\ \vdots \\ \bar{E}'_n/(jX'_{dn}) \\ 0 \\ \vdots \\ -(\bar{S}_{l_L}/\bar{U}_L)^* \\ \vdots \\ 0 \end{bmatrix}. \quad (5.20)$$

Equation (5.20) relates the voltages at load buses and generator terminals with the internal voltages of the generators and the voltage of the "extracted" load at bus L. Any k^{th} row of the resulting Eq. (5.20) represents the equation for the voltage at k^{th} bus:

$$\bar{U}_k = -\bar{Z}_{kL}\left(\frac{\bar{S}_{l_L}}{\bar{U}_L}\right)^* + \sum_{i=1}^{n} \bar{Z}_{ki}\frac{\bar{E}'_i}{jX'_{di}} = -\bar{Z}_{kL}\left(\frac{\bar{S}_{l_L}}{\bar{U}_L}\right)^* + \bar{\varepsilon}_k, \text{ for } k = 1, ..., N. \quad (5.21)$$

In $\bar{\varepsilon}_k = \sum_{i=1}^{n} \bar{Z}_{ki}\bar{E}'_i/jX'_{di}$ everything stays constant during dynamics except for the rotor angles (i.e. $\bar{\varepsilon}_k = f(\boldsymbol{\delta})$). This means that each of N system voltages is a function of the constant post-fault parameters, variable rotor angles and variable load voltage $\bar{U}_L$. It is, therefore, apparent that the existence of closed form expressions $\boldsymbol{U}(\boldsymbol{\delta})$ and $\boldsymbol{\theta}(\boldsymbol{\delta})$ depends on whether or not the load voltage $\bar{U}_L$:

$$\bar{U}_L = -\bar{Z}_{LL}\left(\frac{\bar{S}_{l_L}}{\bar{U}_L}\right)^* + \sum_{i=1}^{n} \bar{Z}_{Li}\frac{\bar{E}'_i}{jX'_{di}} = -\bar{Z}_{LL}\left(\frac{\bar{S}_{l_L}}{\bar{U}_L}\right)^* + \bar{\varepsilon}_L(\boldsymbol{\delta}) \quad (5.22)$$

can always be solved with respect to $\boldsymbol{\delta}$. The task of the following chapter is to answer this question by investigating potential limitations for voltage solution existence when different types of static load models are employed.

Chapter 6

VIR and Their Role in RAS Region Assessment

The previous chapter has introduced a Voltage Impasse Region (VIR) as a state-space area at which voltage causality is lost. The following pages further extend the analysis by providing the mathematical description of these "forbidden" areas. The aim of Chapter 6 is to carry out a comprehensive study that explains the relationship between VIR and the non-linear static loads in power system dynamics.

The final part of this thesis will focus on the analytical description of the state-space areas at which DAE model of a power system fails. The VIR area has first been explained on a conceptual level with the help of "impasse surface" terminology. Then the analytical example from Section 5.4 determined the relationship between voltage solution existence and the value of one state-space variable (δ) for the single machine case. The static, voltage independent constant power load model was to blame for the loss of voltage solution. This observation is particularly interesting knowing that the fast restoration of the pre-fault active consumption (as in the case of induction motors) is one of the driving mechanisms for short-term voltage instability in dynamics of large disturbances [55, 168]. The simple example also concluded that the VIR is a dynamical "twin" of the static loadability.

However, what would happen when more machines are involved or when the load is of e.g. constant current type? The last section of Chapter 5 expands the study from Section 5.4 by simply applying Kirchhoff's current law to a multi-machine power system. The transformation of DAE to ODE is shown to be always possible when there are no constraints imposed on the existence of $\boldsymbol{U}(\boldsymbol{\delta})$ and $\boldsymbol{\theta}(\boldsymbol{\delta})$. As a final result, Chapter 5 sets up the voltage load solution in a convenient form such

that more detailed analysis can be carried out:

$$\bar{U}_L = -\bar{Z}_{LL}\left(\frac{\bar{S}_{l_L}}{\bar{U}_L}\right)^* + \sum_{i=1}^{n} \bar{Z}_{Li}\frac{\bar{E}'_i}{jX'_{di}} = -\bar{Z}_{LL}\left(\frac{\bar{S}_{l_L}}{\bar{U}_L}\right)^* + \bar{\varepsilon}_L(\boldsymbol{\delta}). \tag{6.1}$$

The unlimited existence of load voltage solution implies that it is possible to obtain the closed form expressions $\boldsymbol{U}(\boldsymbol{\delta})$ and $\boldsymbol{\theta}(\boldsymbol{\delta})$. In other words, **wherever in the state-space the load voltage solution can be found based on DAE model, voltage causality is locally maintained and ODE formulation holds.**

Instead of finding where the reduction from DAE to ODE is possible, the target here is to find out for which cases this transformation cannot be carried out. Chapter 6 will, generally speaking, have the three main tasks that correspond to the Steps 3-5 of the algorithm from Fig. 5.4:

1. The voltage solution $\bar{U}_L$ should be analyzed with respect to the three types of the static load models, namely: (i) constant power, (ii) constant current and (iii) constant impedance load models. By using the same approach, the problem will also be formulated for a more general, ZIP load model.

2. Voltage Collapse Indicators (VCIs) are developed to associate a certain value to each state-space point that surrounds a post-fault equilibrium.

3. With the help of VCIs being subject to a singularity condition, VIR will be defined via trigonometric functions in the relative rotor-angle space.

The expression (6.1) is the starting point for this chapter. By employing different static load models, Eq. (6.1) is carefully analyzed in order to define VIR for a specific set of post-fault parameters that correspond to a small-signal stable x_s^{post}. The constant impedance load can be used to verify the approach since this type of load should never introduce VIR (as it was shown in Subsection 2.3.2 where the SPM was transformed into the RNM). Several Voltage Collapse Indicators (VCIs) will also be developed to quantify state-space locations and derive VIR for the constant power and constant current load models.

The theoretical prediction about VIR will be tested by using a 3-machine system where a dynamical trajectory is calculated based on the partitioned solution approach. The case study explores the observable consequences of entering a VIR when the type and the size of the load are varied. The aim is to possibly make a link between the loss of voltage causality and non-convergence issues in TDS. The matching between VIR and a failure of a simulation program to converge would indicate that the numerical issues are only “symptoms" of a larger, underlaying problem that concerns the consistency of the DAE model.

6.1 VIR as a result of constant power load modeling

The first interesting case is dealing with the constant power model of the load at bus L for which the exponent $ms = 0$:

$$\bar{S}_{l_L} = P_{l_L} + jQ_{l_L} = (P_{l_{L0}} + jQ_{l_{L0}}) \left(\frac{U_L}{U_{L_0}} \right)^{ms} = \bar{S}_{l_{L0}}. \tag{6.2}$$

When the constant power $\bar{S}_{l_{L0}}$ is replaced into Eq. (6.1), the expression for the voltage of the load at bus L becomes:

$$\bar{U}_L = -\bar{Z}_{LL} \left(\frac{\bar{S}_{l_{L0}}}{\bar{U}_L} \right)^* + \sum_{i=1}^{n} \bar{Z}_{Li} \frac{\bar{E}'_i}{jX'_{di}} = \frac{\bar{a}}{\bar{U}_L^*} + \bar{\varepsilon}_L, \text{ where } \bar{a} = -\bar{Z}_{LL} \bar{S}^*_{l_{L0}}. \tag{6.3}$$

The value of $\bar{a}$ is a constant that reflects the parameters of the post-fault system. Let this constant be given in the form $\bar{a} = a_{_R} + ja_{_X} = const$. By looking into Eq. (6.3) it is clear that as the dynamic states evolve, $\bar{\varepsilon}_L = f(\boldsymbol{\delta})$ varies which further causes that both the magnitude and the rotor angle of $\bar{U}_L = U_L(\boldsymbol{\delta}) e^{j\theta_L(\boldsymbol{\delta})}$ change. The focus of the study is the existence of a feasible load voltage magnitude solution (as in the example from Section 5.4). The dependency $\theta_L(\boldsymbol{\delta})$ can always be obtained (there are no rigorous mathematical constraints that are imposed on the voltage angle). However, this is not the case for the magnitude U_L. To find an explicit expression for U_L, Eq. (6.3) is first multiplied by $\bar{U}_L^* \neq 0$ and then transformed as:

$$\begin{aligned} &U_L^2 = \bar{a} + \bar{U}_L^* \bar{\varepsilon}_L \Rightarrow \bar{U}_L^* = \frac{U_L^2 - \bar{a}}{\bar{\varepsilon}_L} \wedge \bar{U}_L = \left(\frac{U_L^2 - \bar{a}}{\bar{\varepsilon}_L} \right)^* \Rightarrow \\ &\Rightarrow U_L^2 = \bar{U}_L^* \bar{U}_L = \left(\frac{U_L^2 - \bar{a}}{\bar{\varepsilon}_L} \right) \left(\frac{U_L^2 - \bar{a}}{\bar{\varepsilon}_L} \right)^* = \frac{U_L^4 - (\bar{a} + \bar{a}^*) U_L^2 + a^2}{\varepsilon_L^2}. \end{aligned} \tag{6.4}$$

The multiplication of the resulting expression from Eq. (6.4) by $\varepsilon_L^2 \neq 0$ results in a biquadratic equation with respect to U_L as:

$$0 = U_L^4 + (-\varepsilon_L^2 - 2a_{_R}) U_L^2 + a^2, \tag{6.5}$$

where the four solutions for the magnitude of the voltage at bus L are given by:

$$U_{L_{1,2,3,4}} = \pm \sqrt{\frac{(\varepsilon_L^2 + 2a_{_R}) \pm \sqrt{(\varepsilon_L^2 + 2a_{_R})^2 - 4a^2}}{2}}. \tag{6.6}$$

Two of the solutions of Eq. (6.6), namely U_{L_3} and U_{L_4}, are obviously not the feasible ones since they correspond to the minus sign in front of the first square root. The more detailed discussion about the other two solutions (U_{L_1} and U_{L_2}) follows.

6.1.1 Voltage solutions discussion

The mathematical requirement for the magnitude of a phasor is that it needs to have a real ($\mathbb{R}$), positive value. The inspection of Eq. (6.6) eliminated the two negative solutions U_{L_3} and U_{L_4}. The following proposition states the conditions for the existence of the remaining two (U_{L_1} and U_{L_2}) voltage magnitude solutions.

Proposition 1. *Let the discriminant of Eq.* (6.6) *be denoted as the Voltage Collapse Indicator for the Constant Power load model (VCI_{CP}), i.e.:*

$$VCI_{CP} = (\varepsilon_L^2 + 2a_{_R})^2 - 4a^2 = \varepsilon_L^4 + 4\varepsilon_L^2 a_{_R} - 4a_{_X}^2. \tag{6.7}$$

In order to have at least one feasible solution for the load voltage magnitude:

$$U_{L_{1,2}} = +\sqrt{\frac{(\varepsilon_L^2 + 2a_{_R}) \pm \sqrt{(\varepsilon_L^2 + 2a_{_R})^2 - 4a^2}}{2}}, \tag{6.8}$$

the indicator VCI_{CP} needs to satisfy the necessary and sufficient Condition (C.I):

$$C.I : VCI_{CP} = (\varepsilon_L^2 + 2a_{_R})^2 - 4a^2 \geq 0. \tag{6.9}$$

Proof. The acceptable solution for magnitude U_L will exist if the expression under the square root of Eq. (6.8) is positive and real:

$$\left((\varepsilon_L^2 + 2a_{_R}) \pm \sqrt{(\varepsilon_L^2 + 2a_{_R})^2 - 4a^2}\right)/2 > 0. \tag{6.10}$$

The fulfillment of Condition (C.I) (non-negativity of VCI_{CP}) implies that:

$$\varepsilon_L^2 + 2a_{_R} + \sqrt{(\varepsilon_L^2 + 2a_{_R})^2 - 4a^2} > 0 \quad \text{and}$$
$$\varepsilon_L^2 + 2a_{_R} - \sqrt{(\varepsilon_L^2 + 2a_{_R})^2 - 4a^2} > \varepsilon_L^2 + 2a_{_R} - \sqrt{(\varepsilon_L^2 + 2a_{_R})^2} = 0.$$

It may be noted that, if C.I is satisfied, there are always two real and positive ($\mathbb{R}$) voltage magnitude solutions:

$$U_{L_{1,2}} = \sqrt{\left((\varepsilon_L^2 + 2a_{_R}) \pm \sqrt{(\varepsilon_L^2 + 2a_{_R})^2 - 4a^2}\right)/2} > 0, \tag{6.11}$$

i.e. a high and a low voltage solution. In Fig. 6.1, Condition (C.I) represents the union of the white area ($VCI_{CP} > 0$) and parabola $VCI_{CP} = (\varepsilon_L^2 + 2a_{_R})^2 - 4a^2 = 0$. The two solutions cease to exist after the merging point $VCI_{CP} = 0$, at which:

$$U_{L_1} = U_{L_2} = U_L^{lim} = \sqrt{\frac{(\varepsilon_L^2 + 2a_{_R})}{2}}. \tag{6.12}$$

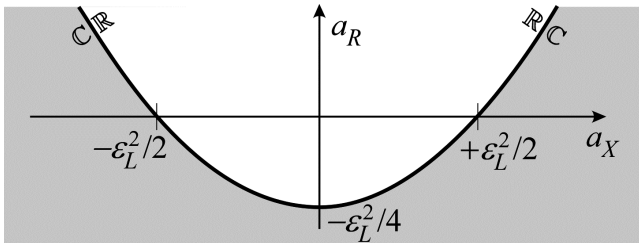

Figure 6.1: The nature of the solution for the magnitude of load voltage $\bar{U}_L$

After this point, for $VCI_{CP} < 0$, the two solutions will have non-zero imaginary components. Simply put, $U_{L_{1,2}}$ will become complex numbers ($\mathbb{C}$) in the gray area of Fig. 6.1, which is not a feasible solution for the magnitude of a phasor. □

The condition $VCI_{CP} = (\varepsilon_L^2 + 2a_{_R})^2 - 4a^2 < 0$ is equivalent to the loss of voltage causality. Since the boundary of the gray area from Fig. 6.1 depends on $\varepsilon_L = f(\boldsymbol{\delta})$, the idea is to use VCI_{CP} and introduce the Voltage Impasse Region (VIR) as the subset of state-space that fails to fulfill Condition (C.I).

6.1.2 VIR definition

The next step is to define the Voltage Impasse Region (VIR) based on the criterion that is opposite to the condition for the existence of load voltage solution (6.9). That is to say, the location of the gray area from Fig. 6.1 (at which $VCI_{CP} < 0$) needs to be defined for a stable x_s^{post}. If a q^{th} machine is taken as the reference, the VIR is introduced as an area in the space of relative rotor angles that satisfies:

$$VIR = \{(\delta_{1q}, \delta_{2q}, ..., \delta_{nq}) : (\varepsilon_L^2(\boldsymbol{\delta}) + 2a_{_R})^2 - 4a^2 < 0\}. \tag{6.13}$$

Since $\bar{a}$ and its active component $a_{_R}$ are constant parameters that are coming from a post-fault configuration of the power system, the single entity that varies in Eq. (6.13) due to dynamics is ε_L^2. Now, let ε_L^2 be written as:

$$\varepsilon_L^2(\boldsymbol{\delta}) = \bar{\varepsilon}_L \bar{\varepsilon}_L^* = \sum_{i=1}^{n}\sum_{\ell=1}^{n} \frac{\bar{Z}_{Li}\bar{Z}_{L\ell}^* \bar{E}_i' \bar{E}_\ell'^*}{X_{di}' X_{d\ell}'} = \sum_{i=1}^{n}\sum_{\ell=1}^{n} \bar{K}_{i\ell} E_i' E_\ell' e^{j\delta_{i\ell}}, \text{ where} \tag{6.14}$$

- $\bar{K}_{i\ell} = \dfrac{\bar{Z}_{Li}\bar{Z}_{L\ell}^*}{X_{di}' X_{d\ell}'} = \alpha_{i\ell} + j\beta_{i\ell} = const.$ are constant parameters and
- $\delta_{i\ell} = \delta_{iq} - \delta_{\ell q}$ is the difference of rotor angles that are given in the relative form $(\delta_{iq}, \delta_{\ell q})$ with respect to the rotor angle of the q^{th} generator.

Since it may also be shown that for different values of indices i and ℓ:

$$i = \ell \overset{yields}{\Rightarrow} \qquad \bar{K}_{ii} = \alpha_{ii} = \left(\frac{Z_{Li}}{X'_{di}}\right)^2, \qquad \delta_{ii} = 0 \quad \text{and for} \tag{6.15}$$

$$i \neq \ell \overset{yields}{\Rightarrow} \qquad \bar{K}_{i\ell} = \alpha_{i\ell} + j\beta_{i\ell} = \bar{K}^*_{\ell i}, \qquad e^{j\delta_{i\ell}} = (e^{j\delta_{\ell i}})^*, \tag{6.16}$$

the summation of $(i,\ell)^{th}$ and $(\ell,i)^{th}$ terms from Eq. (6.14) results in:

$$\begin{aligned} \bar{K}_{i\ell}E'_iE'_\ell e^{j\delta_{i\ell}} + \bar{K}_{\ell i}E'_\ell E'_i e^{j\delta_{\ell i}} &= 2\,\mathrm{Re}(\bar{K}_{i\ell}E'_iE'_\ell e^{j\delta_{i\ell}}) \\ &= 2\,\mathrm{Re}\left((\alpha_{i\ell}+j\beta_{i\ell})E'_iE'_\ell e^{j\delta_{i\ell}}\right) \\ &= 2E'_iE'_\ell(\alpha_{i\ell}\cos(\delta_{i\ell}) - \beta_{i\ell}\sin(\delta_{i\ell})). \end{aligned} \tag{6.17}$$

By the virtue of Eqs. (6.13)-(6.17), the VIR can now be fully defined as the set:

$$\boxed{\begin{aligned} &VIR = \{(\delta_{1q},\delta_{2q},...,\delta_{nq}) : (\varepsilon_L^2(\boldsymbol{\delta}) + 2a_{_R})^2 - 4a^2 < 0\},\ \text{where} \\ &\varepsilon_L^2(\boldsymbol{\delta}) = \sum_{i=1}^{n}\left(\alpha_{ii}E_i'^2 + 2\sum_{\ell=i+1}^{n} E'_iE'_\ell(\alpha_{i\ell}\cos(\delta_{i\ell}) - \beta_{i\ell}\sin(\delta_{i\ell}))\right). \end{aligned}} \tag{6.18}$$

The VIR, in a fact, represents the union of all those combinations of $(n-1)$ relative rotor angles that do not fulfill Condition (C.I). The boundary of a VIR is apparently a trigonometric function that is defined in the relative rotor angle space with respect to the parameters of a post-fault system. It is not necessary to perform TDS to know the location of a VIR. The existence of a VIR can be simply assessed by applying the expression from Eq. (6.18). In the sequel, the same approach will investigate if VIR may also appear due to the constant current load model.

6.2 VIR as a result of constant current load modeling

It is known that fast recovering loads that operate close to the constant power characteristics may lead to significant drops of voltages in the seconds following a large disturbance [168]. However, the existing studies did not discuss the constant current load characteristic in the same context, i.e. this type of load model has typically been considered as a “safe" one when it comes to short-term voltage instability. This is why it is important to investigate if VIR can be introduced when the load power follows the constant current characteristic ($ms = 1$):

$$\bar{S}_{l_L} = P_{l_L} + jQ_{l_L} = (P_{l_{L0}} + jQ_{l_{L0}})\left(\frac{U_L}{U_{L_0}}\right)^{ms} = \bar{S}_{l_{L0}}\left(\frac{U_L}{U_{L_0}}\right). \tag{6.19}$$

Once again, by replacing the power from Eq. (6.19) into Eq. (6.1), it follows that:

$$\bar{U}_L = -\bar{Z}_{LL}\left(\frac{\bar{S}^*_{l_{L0}}U_L}{U_{L_0}\bar{U}^*_L}\right)+\sum_{i=1}^{n}\bar{Z}_{Li}\frac{\bar{E}'_i}{jX'_{di}} = \frac{\bar{b}U_L}{\bar{U}^*_L}+\bar{\varepsilon}_L, \text{ where } \bar{b} = \frac{-\bar{Z}_{LL}\bar{S}^*_{l_{L0}}}{U_{L_0}} \quad (6.20)$$

is a constant that can be written in a general form as $\bar{b} = b_{_R} + jb_{_X} = const$. Since the solution for the magnitude U_L needs to be analyzed, Eq. (6.20) is multiplied by $\bar{U}^*_L \neq 0$ to eliminate the angle of the load voltage as:

$$\begin{aligned} &{U_L}^2 = \bar{U}_L\bar{U}^*_L = \bar{b}U_L + \bar{\varepsilon}_L\bar{U}^*_L \Rightarrow \bar{U}^*_L = \frac{U_L(U_L-\bar{b})}{\bar{\varepsilon}_L} \wedge \bar{U}_L = (\bar{U}^*_L)^* \Rightarrow \\ &\Rightarrow {U_L}^2 = \bar{U}_L\bar{U}^*_L = \frac{{U_L}^2(U_L-\bar{b})(U_L-\bar{b}^*)}{\varepsilon_L^2} = \frac{{U_L}^2(U_L^2-2b_{_R}U_L+b^2)}{\varepsilon_L^2}. \end{aligned} \quad (6.21)$$

For $\varepsilon_L^2 \neq 0$, the voltage magnitude appears to be the only variable in the equation:

$$U_L^2 - 2b_{_R}U_L + (b^2-\varepsilon_L^2) = 0, \quad (6.22)$$

that is quadratic in nature and has two possible roots for magnitude U_L:

$$U_{L_{1,2}} = b_{_R} \pm \sqrt{b_{_R}^2-(b^2-\varepsilon_L^2)} = b_{_R} \pm \sqrt{\varepsilon_L^2-b_{_X}^2}. \quad (6.23)$$

More discussion is needed to determine the conditions for the existence of feasible roots (i.e. solutions) of Eq. (6.22).

6.2.1 Voltage solutions discussion and VIR

The case of constant current load model is more complicated when it comes to the number of solutions for U_L. It has already been stated that feasible roots (i.e. solutions) need to be real and positive. This time, the solution also depends on the constant $b_{_R}$ that reflects the parameters of the system. There are several options when it comes to the value of roots in Eq. (6.23). Beside “impossible", complex roots ($\mathbb{C}$) that appear by following the same mechanism as in the case of constant power load model, it can also occur that the the roots are physically “infeasible", i.e. that they have real ($\mathbb{R}$) and negative values. Let all the possible combinations of the roots be marked as $(++)$, $(+-)$, $(--)$ and ($\mathbb{C}$) such that they denote the cases of (i) two real and positive roots $(++)$; (ii) two real roots out of which one has a positive and the other one has a negative value $(+-)$; (iii) two real and negative roots $(--)$

and (iv) two complex roots ($\mathbb{C}$). Then, depending on the system characteristics (b_R), the types of U_{L_1} and U_{L_2} roots and the number of solutions are given as follows:

$$\text{if } b_R \leq 0 \Rightarrow \left\{ \begin{array}{ll} \text{no solutions } (\mathbb{C}), & \varepsilon_L^2 < b_X^2 \\ \text{no solutions (- -)}, \quad \text{for} & b_X^2 \leq \varepsilon_L^2 < b^2 \\ \text{1 solution (+ -)}, & \varepsilon_L^2 \geq b^2 \end{array} \right\} \text{ or}$$

$$\text{if } b_R > 0 \Rightarrow \left\{ \begin{array}{ll} \text{no solutions } (\mathbb{C}), & \varepsilon_L^2 < b_X^2 \\ \text{2 solutions (+ +)}, \quad \text{for} & b_X^2 \leq \varepsilon_L^2 < b^2 \\ \text{1 solution (+ -)}, & \varepsilon_L^2 \geq b^2 \end{array} \right\}.$$

Apparently, there exists a possibility for the constant current load to introduce a VIR. The given classification may also be visually represented as in Fig. 6.2.

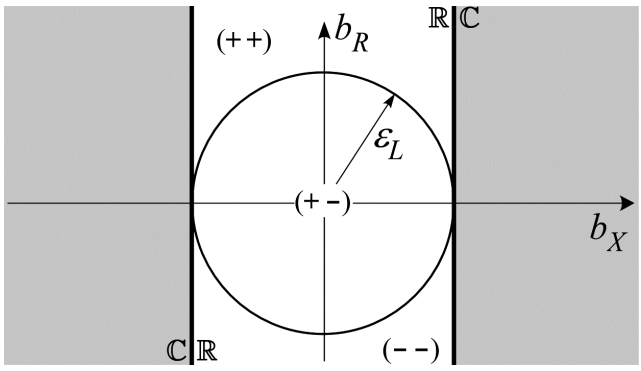

Figure 6.2: The nature of the solution for the magnitude of $\bar{U}_L$

To simplify the analysis, two Voltage Collapse Indicators for the Constant Current load model ($VCIs_{CC} = \{VCI_{CC1}, VCI_{CC2}\}$) are next proposed in order to judge about the number and existence of voltage solutions. These indicators will also be used to define VIR.

Proposition 2. *Let the Voltage Collapse Indicators for the Constant Current ($VCIs_{CC}$) load model be distinguished with respect to the system characteristics (b_R) as:*

$$\textit{if } b_R \leq 0 \quad \Rightarrow \textit{I:} \quad VCI_{CC1} = \varepsilon_L^2 - b^2 \textit{ or} \tag{6.24}$$

$$\textit{if } b_R > 0 \quad \Rightarrow \textit{II:} \quad VCI_{CC1} = \varepsilon_L^2 - b^2 \wedge \textit{III:} VCI_{CC2} = \varepsilon_L^2 - b_X^2. \tag{6.25}$$

Then, necessary and sufficient conditions that need to be fulfilled such that there exists minimum one solution for the load voltage magnitude from Eq. (6.23) *are:*

$$\text{if } b_R \leq 0 \qquad \text{C.I} : VCI_{CC1} = \varepsilon_L^2 - b^2 > 0 \tag{6.26}$$

$$\text{if } b_R > 0 \qquad \text{C.II} : VCI_{CC2} = b_R^2 - (b^2 - \varepsilon_L^2) = \varepsilon_L^2 - b_X^2 \geq 0. \tag{6.27}$$

Proof. In the first case ($b_R \leq 0$), the fulfillment of Condition (C.I) results in one voltage magnitude solution:

$$U_{L_1} = b_R + \sqrt{b_R^2 - (b^2 - \varepsilon_L^2)} > b_R + \sqrt{b_R^2} = 0. \tag{6.28}$$

At $VCI_{CC1} = 0$, the value of this root would become zero (which is not allowed due to assumption $\bar{U}_L^* \neq 0$). The other root U_{L_2} is also real for $VCI_{CC1} > 0$, however, it has a negative value. For $b_R > 0$, Condition (C.II) always ensures the existence of at least one solution:

$$U_{L_1} = b_R + \sqrt{b_R^2 - (b^2 - \varepsilon_L^2)} = b_R + \sqrt{\varepsilon_L^2 - b_X^2} > 0. \tag{6.29}$$

If additionally, $VCI_{CC1} = \varepsilon_L^2 - b^2 < 0$, another U_L solution occurs as:

$$U_{L_2} = b_R - \sqrt{b_R^2 - (b^2 - \varepsilon_L^2)} > b_R - \sqrt{b_R^2} = 0. \tag{6.30}$$

Thus, in this case, two positive voltage magnitude solutions exist. The borderline of the solution existence is reached at $VCI_{CC2} = 0$, where the two solutions merge. On the other hand, at $VCI_{CC1} = 0$ the low solution (U_{L_2}) would become zero. □

The Conditions (C.I) and (C.II) and associated Voltage Collapse Indicators ($VCIs_{CC}$) will be employed in VIR definition for the constant current load model. The regions with different numbers of solutions are sketched in Fig. 6.3.

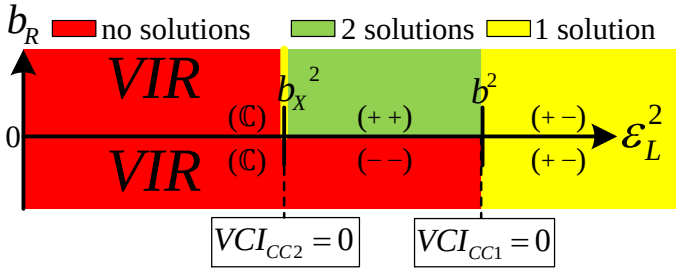

Figure 6.3: The relationship between U_L solutions, $VCIs_{CC}$ and VIR

In this figure, the system characteristic $b_{_R}$ is a parameter and ε_L^2 is the function of $\boldsymbol{\delta}$ ($\varepsilon_L^2(\boldsymbol{\delta})$ is identical to the one from Eq. (6.18) that has been derived for the constant power load model). As explained in Proposition 2, the voltage magnitude solution can be lost due to either (i) the upper voltage solution becoming negative after $VCI_{CC1} = 0$ (for $b_{_R} \leq 0$) or (ii) due to the roots of Eq. (6.23) turning complex after merging at $VCI_{CC2} = 0$ (for $b_{_R} > 0$). The red zone where there is no feasible voltage solution is actually the VIR. At the point $VCI_{CC1} = 0$ ($b_{_R} > 0$), Eq. (6.23) yields zero for the lower voltage solution (which is not in line with the assumption $\bar{U}_L^* \neq 0$). This point represents the transit between the two "stable" regions where the loss of voltage causality is not expected to happen due to DAE model following the desirable, upper voltage solution. Finally, by taking into account the Conditions (C.I) and (C.II), the VIR is defined in the space of relative rotor angles as:

$$\boxed{\begin{aligned} VIR &= \left\{ \begin{matrix} (\delta_{1q}, \delta_{2q}, ..., \delta_{nq}) : \varepsilon_L^2(\boldsymbol{\delta}) - b^2 \leq 0 & \text{for} & b_{_R} \leq 0 \\ (\delta_{1q}, \delta_{2q}, ..., \delta_{nq}) : \varepsilon_L^2(\boldsymbol{\delta}) - b_{_X}^2 < 0 & & b_{_R} > 0 \end{matrix} \right\}, \text{ where} \\ \varepsilon_L^2(\boldsymbol{\delta}) &= \sum_{i=1}^{n} \left(\alpha_{ii} E_i'^2 + 2 \sum_{\ell=i+1}^{n} E_i' E_\ell' (\alpha_{i\ell} \cos(\delta_{i\ell}) - \beta_{i\ell} \sin(\delta_{i\ell})) \right). \end{aligned}} \tag{6.31}$$

Hence, the Conditions (C.I)-(C.II) may be used as valid $VCIs_{CC}$ to indicate a voltage collapse and define the VIR for the constant current load model.

The general theoretical conclusion is that both non-linear static load models may introduce VIR areas at which voltages cannot be identified based on the DAE model of a power system. For a known post-fault configuration, the exact analytical description of the VIR is given by Eqs. (6.18) and (6.31).

6.3 VIR in the case of constant impedance load model and ZIP load model

It is well-known that the constant impedance load model enables the transformation of DAE into an ODE form. Subsection 2.3.2 has demonstrated this for the n-machine power system model where all the loads were given by constant impedances and the generators were presented by classical models. It is convenient to confirm this feature from another perspective, i.e. by applying the same approach from the previous sections. This means that the constant impedance load at bus L is still

"kept outside" of the admittance matrix $\mathbf{Y}'$ in order to discuss the solution for voltage magnitude U_L.

6.3.1 Voltage solution for constant impedance load

Proposition 3. *Assuming that the load at bus L in the model from Fig. 5.9 is of constant impedance type, a solution for the voltage at bus L (and consequently, the solutions for the other voltages) is always obtainable regardless of the state-space location. In other words, constant impedance loads do not introduce VIR.*

Proof. The power of the static, constant impedance load at bus L is given by replacing $ms = 2$ into Eq. (5.17):

$$\bar{S}_{l_L} = P_{l_L} + jQ_{l_L} = (P_{l_{L0}} + jQ_{l_{L0}}) \left(\frac{U_L}{U_{L_0}}\right)^{ms} = \bar{S}_{l_{L0}} \left(\frac{U_L}{U_{L_0}}\right)^2. \quad (6.32)$$

By using this power, the voltage of the load at bus L can be rewritten as:

$$\begin{aligned} \bar{U}_L &= -\bar{Z}_{LL} \left(\frac{\bar{S}^*_{l_{L0}} U_L^2}{U_{L_0}^2 \bar{U}^*_L}\right) + \sum_{i=1}^{n} \bar{Z}_{Li} \frac{\bar{E}'_i}{jX'_{di}} = \frac{\bar{c} U_L^2}{\bar{U}^*_L} + \bar{\varepsilon}_L \text{ where} \\ \bar{c} &= -\frac{\bar{Z}_{LL} \bar{S}^*_{l_{L0}}}{U_{L_0}^2} = -\frac{\bar{Z}_{LL}}{\bar{Z}_{l_L}} = c_R + jc_X = const. \end{aligned} \quad (6.33)$$

As before, the angle of the voltage can be eliminated from the problem for $\bar{U}^*_L \neq 0$:

$$\begin{aligned} {U_L}^2 =& \bar{U}_L \bar{U}^*_L = \bar{c} U_L^2 + \bar{\varepsilon}_L \bar{U}^*_L \Rightarrow \bar{U}^*_L = \frac{U_L^2(1-\bar{c})}{\bar{\varepsilon}_L} \wedge \bar{U}_L = \frac{U_L^2(1-\bar{c}^*)}{\bar{\varepsilon}^*_L} \Rightarrow \\ \Rightarrow & \bar{U}_L \bar{U}^*_L = U_L^2 = \frac{{U_L}^4 (1-\bar{c})(1-\bar{c}^*)}{\varepsilon_L^2} = \frac{{U_L}^4 \mid 1-\bar{c} \mid^2}{\varepsilon_L^2}. \end{aligned} \quad (6.34)$$

The division of Eq. (6.34) by ${U_L}^2$ results in a quadratic equation that always has one positive voltage magnitude solution:

$$U_L^2 \mid 1-\bar{c} \mid^2 - \varepsilon_L^2 = 0 \overset{U_L>0}{\Longrightarrow} U_L = \frac{\varepsilon_L}{\mid 1-\bar{c} \mid}, \quad (6.35)$$

except for the special case $\bar{c} = 1$, which corresponds to some sort of resonance $\bar{Z}_{LL} = -\bar{Z}_{l_L}$. However, this case does not correspond to any small-signal stable post-fault operating point since $\bar{c} = 1$ would imply that $U_L \to \infty$ at steady-state. Hence, the voltage causality is always maintained when all the loads are of constant impedance type, which further confirms that the constant impedance load cannot introduce VIR. □

6.3.2 Problem formulation for ZIP load model

Now all the three basic types of static load models have been analyzed with respect to the existence of voltage solution. It has been shown that voltage causality can be lost due to both constant power and constant current loads, which does not apply to the constant impedance load model.

Nevertheless, it is more common that the aforementioned static load components constitute ZIP load model that can provide a more realistic insight into a dynamic response of a power system. In that sense, the ZIP model can, for instance, cover the effect of motors when they are represented by constant impedances or it can take into account power electronic based devices in both P (constant power) and I (constant current) control modes etc. So, what happens if all the three types of static loads are combined into a more general ZIP load at bus L? The active and reactive powers of such load can be expressed as in Eq. (2.7):

$$\begin{aligned} P_{l_L} &= P_{l_{L0}}\Big[k_{Pz}(\frac{U_L}{U_{L_0}})^2 + k_{Pi}(\frac{U_L}{U_{L_0}}) + k_{Pp}\Big] \text{ and} \\ Q_{l_L} &= Q_{l_{L0}}\Big[k_{Qz}(\frac{U_L}{U_{L_0}})^2 + k_{Qi}(\frac{U_L}{U_{L_0}}) + k_{Qp}\Big]. \end{aligned} \tag{6.36}$$

The aim of this subsection is to formulate the problem $p(U_L) = 0$ such that the voltage solution existence can be examined for the ZIP load model (6.36). If, for simplification purposes, it is assumed that $k_{Pz} = k_{Qz} = k_z$, $k_{Pi} = k_{Qi} = k_i$ and $k_{Pp} = k_{Qp} = k_p$, then the load complex power is expressed as:

$$\bar{S}_{l_L} = \bar{S}_{l_{L0}}\Big[k_z(\frac{U_L}{U_{L_0}})^2 + k_i(\frac{U_L}{U_{L_0}}) + k_p\Big]. \tag{6.37}$$

When the power $\bar{S}_{l_L}$ of the ZIP load at bus L is replaced into (6.1), the multiplication of (6.1) by $\bar{U}_L^* \neq 0$ provides:

$$U_L^2 = \bar{U}_L\bar{U}_L^* = -\bar{Z}_{LL}\bar{S}_{l_L}^* + \bar{U}_L^*\bar{\varepsilon}_L \Rightarrow \bar{U}_L^* = \frac{(1+\bar{c}_{ZIP})U_L^2 + \bar{b}_{ZIP}U_L + \bar{a}_{ZIP}}{\bar{\varepsilon}_L}, \tag{6.38}$$

where $\bar{c}_{ZIP} = k_z\dfrac{\bar{Z}_{LL}\bar{S}_{l_{L0}}^*}{U_{L_0}^2}$, $\bar{b}_{ZIP} = k_i\dfrac{\bar{Z}_{LL}\bar{S}_{l_{L0}}^*}{U_{L_0}}$ and $\bar{a}_{ZIP} = k_p\bar{Z}_{LL}\bar{S}_{l_{L0}}^*$ are the constants that originate from the corresponding ZIP components and $\bar{\varepsilon}_L$ is the function of $\boldsymbol{\delta}$. Following the same procedure as in (6.4), (6.21) and (6.34), the resulting equation from (6.38) is further multiplied with its conjugate to obtain the

expression of the form $p(U_L) = 0$ as:

$$\begin{aligned}
&p_{ZIP4}U_L^4 + p_{ZIP3}U_L^3 + p_{ZIP2}U_L^2 + p_{ZIP1}U_L + p_{ZIP0} = 0,\\
&p_{ZIP4} = \mid 1 + \bar{c}_{ZIP} \mid^2;\\
&p_{ZIP3} = 2\,\mathrm{Re}\left[(1 + \bar{c}_{ZIP})\bar{b}^*_{ZIP}\right];\\
&p_{ZIP2} = 2\,\mathrm{Re}\left[(1 + \bar{c}_{ZIP})\bar{a}^*_{ZIP}\right] + b^2_{ZIP} - \varepsilon^2_L(\boldsymbol{\delta});\\
&p_{ZIP1} = 2\,\mathrm{Re}(\bar{a}_{ZIP}\bar{b}^*_{ZIP});\\
&p_{ZIP0} = a^2_{ZIP},
\end{aligned} \tag{6.39}$$

which is a quartic equation with respect to U_L. The equation (6.39) has four roots and it is a function of rotor angles via its coefficient p_{ZIP2}. Hence, the roots are affected when rotor angles start to move. It would be of importance for dynamic studies to describe this relation further. Some of the options for finding the regions without voltage causality (VIR) are (i) to analyze the discriminant of Eq. (6.39); (ii) to carry out a numerical procedure [99] for finding U_L solution or (iii) to explicitly solve quartic Eq. (6.39) by employing the Ferrari's algebraic approach [180]. A more detailed analysis of the ZIP load model is planned as a part of the future work.

6.4 Test system

In order to verify the theoretical characterization of VIR from Eqs. (6.18) and (6.31), the small test system from Fig. 6.4 will be considered. The reason behind using this type of system is that the two-dimensional relative rotor angle space enables the visualization of the VIR concept. The angle of the third generator ($q = 3$) will be used as the reference.

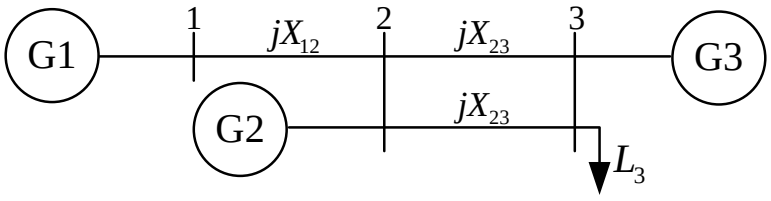

Figure 6.4: Three-machine one-load test system

The three generators are represented by the classical models, the line impedances are purely reactive ($X_{12} = 0.02$ [p.u.], $X_{23} = 0.15$ [p.u.]) and the shunt admittances

are neglected. The load is connected directly to the terminal bus of the third generator (i.e. $L = 3$). Figure 6.5 represents the equivalent of the model from Fig. 6.4. In Fig. 6.5, the generators are represented by their internal voltages ($\bar{E}'_i$, $i = 1, 2, 3$) behind the transient reactances $X'_{di} = 0.45$ [p.u.] that here also include the transformers reactances. The ratings of the generators are $S_{n1} = 100$ [MVA], $S_{n2} = 100$ [MVA] and $S_{n3} = 800$ [MVA]. The generators also have the same inertias ($H_i = 3$ [s]) and the damping constants ($D_i = 2$ [p.u.]).

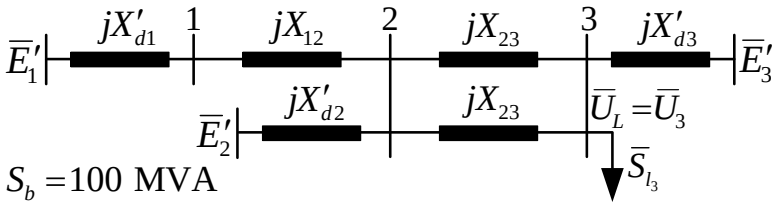

Figure 6.5: The equivalent model of the test system for the study of VIR

The primary idea of the study is to verify the theoretical expressions that describe VIR for the constant power and constant current load models. It is also interesting to establish the relationship between the type/size of the static load and the appearance of VIR. For that purpose, the static power of the load $\bar{S}_{l30} = P_{l30} + j2.6$ [p.u.] will be varied by changing the active consumption P_{l30}. Beside predicting VIR location, the case study should also investigate how a dynamical simulation is affected by VIR. The three-phase short-circuit that occurs very close to bus 2 (on one of the two lines between the buses 2 and 3) will be used in Time Domain Simulation (TDS). The fault will be cleared by tripping the faulted line. The post-fault operating point is chosen such that it is small-signal stable. As the active power of the load at bus 3 is varied, the pre-fault (x_s^{pre}) and the post-fault (x_s^{post}) operating points will change accordingly. The simulation employs the partitioned solution approach where the integration of the differential part of the DAE model is carried out by the means of Modified Euler Method [181] that has been explained in Subsection 2.4.2. This predictor-corrector based method is set up in a way that it continues attempting to solve the set of DAE even for those time steps where the numerical procedure does not converge. The case study results are structured as follows:

- The constant power load is investigated first. VIR are predicted for a certain post-fault operating point. TDS should provide the answers to the following questions: What happens with the simulation when a dynamical trajectory encounters a VIR? Are there some consequences when it comes to short-term RAS assessment?

- The constant current load characteristic will be changed such that the both cases of system parameters ($b_R \leq 0$ and $b_R > 0$) are covered.
- The three static load models are compared and discussed.

6.5 Results

The upcoming results are based on the test system from Fig. 6.5. The angles of a stable, post-fault operating state ($\delta_{13s}^{post}, \delta_{23s}^{post}$) are altered by the active power of the load $P_{l_{30}}$. It is beneficial to have a picture about RAS region when a VIR is to be assessed. As mentioned in Subsection 3.1.2, the approximated type-1 UEPs:

$$\begin{array}{lll} (\pi - \delta_{13s}^{post}, \delta_{23s}^{post}), & (\delta_{13s}^{post}, \pi - \delta_{23s}^{post}), & (-\pi - \delta_{13s}^{post}, \delta_{23s}^{post}), \\ (\delta_{13s}^{post}, -\pi - \delta_{23s}^{post}), & (\pi - \delta_{13s}^{post}, \pi - \delta_{23s}^{post}), & (-\pi - \delta_{13s}^{post}, -\pi - \delta_{23s}^{post}). \end{array} \tag{6.40}$$

may provide an insight into the boundary of RAS region and the modes of machine separation. These approximated UEPs will be recalculated for each operating point.

6.5.1 Constant power load

Case 1: A case of lightly loaded system is to be considered first. The load active power $P_{l_{30}} = 4$ [p.u.] will be compensated mostly by the largest generator $P_{g_3} = 3.2$ [p.u.] while the rest of the power is distributed equally among the other two generators ($P_{g_1} = P_{g_2} = 0.4$ [p.u.]). Figure 6.6 depicts the indicator VCI_{CP} in the space of relative rotor angles. When the post-fault parameters of such an operating point were replaced into the expression for Voltage Collapse Indicator VCI_{CP} from Eq. (6.7), the result was positive for any combination of relative rotor angles. Based on Eq. (6.13), always positive VCI_{CP} implies that the VIR is an empty set, i.e. VIR do not exist at this loading level. The approximations of six type-1 unstable equilibria from Eq. (6.40) are shown as yellow circles while the stable post-fault operating point ($\delta_{13s}^{post}, \delta_{23s}^{post}$) is marked in magenta. The black, dashed curve is a sketch of the short-term RAS region.

There are two trajectories that have been plotted along VCI_{CP} surface. The yellow trajectory corresponds to a critically stable case where $t_{cl} = 0.34$ [s]. A further increase of clearing time led to rotor angle instability for $t_{cl} = 0.35$ [s]. This means that the clearing time along the yellow trajectory is at the same time the critical clearing time in the terms of loss of synchronism (i.e. $t_{cc} = 0.34$ [s]). The unstable trajectory is given by blue line. It may be observed that the yellow

trajectory settles at $(\delta_{13s}^{post}, \delta_{23s}^{post})$ while the stability is lost along the blue trajectory due to the separation of generators 1 and 2 from the 3^{rd} generator. And indeed, the trajectory passes exactly through the type-1 UEP approximation $(\pi - \delta_{13s}^{post}, \pi - \delta_{23s}^{post})$ that corresponds to the actual mode of machine separation.

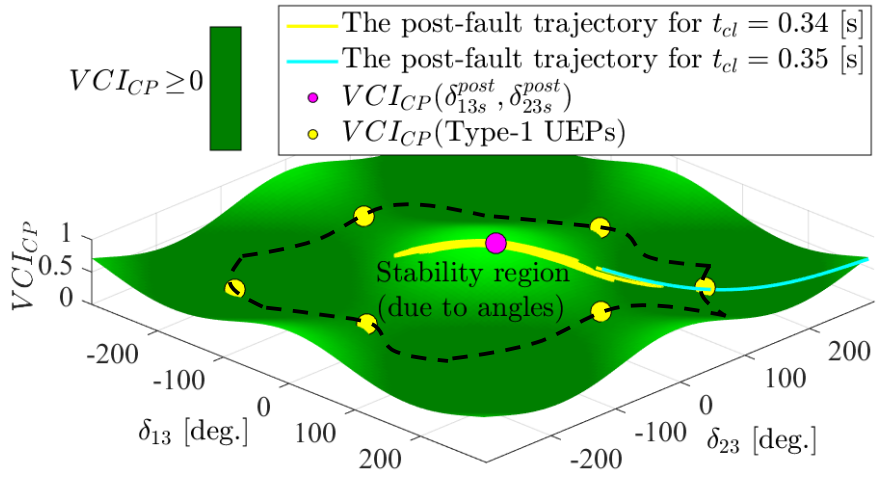

Figure 6.6: VCI_{CP} and post-fault trajectories for the case of lightly loaded system

Case 2: However, what happens if the system is more loaded? Does VCI_{CP} still remain always positive? Consider the case where the active power of the load is doubled ($P_{l_{30}} = 8$ [p.u.]) and where each of the generators doubles its active injection (compared to the initial, lightly loaded case) to compensate for the load increase. Also, the same fault and protective action from **Case 1** are investigated.

The application of the new post-fault parameters resulted in Voltage Collapse Indicator VCI_{CP} from Eq. (6.7) becoming negative for certain combinations of relative rotor angles. The theoretically predicted VCI_{CP} surface, the post-fault SEP $(\delta_{13s}^{post}, \delta_{23s}^{post})$ and the approximations of type-1 UEPs from Eq. (6.40) are all plotted in Fig. 6.7. The areas where $VCI_{CP} < 0$ holds are given in red color. Based on the definition from Eq. (6.18), these areas correspond to the VIR. The sketch of the RAS region is presented by dashed curve. The yellow and light blue trajectories once again relate to the critically stable and unstable cases, respectively. The surfaces for the upper and the lower voltage solutions will also be plotted in Figs. 6.8 (stable case) and 6.9 (unstable case) based on the resulting expression for the magnitude U_L from Eq. (6.8). The red plane in Figs. 6.8-6.9 corresponds to the point where the two voltage solutions merge as $U_3 = U_3^{lim}$. The locations of the

red areas (as seen from above) correspond to the VIR where $VCI_{CP} < 0$.

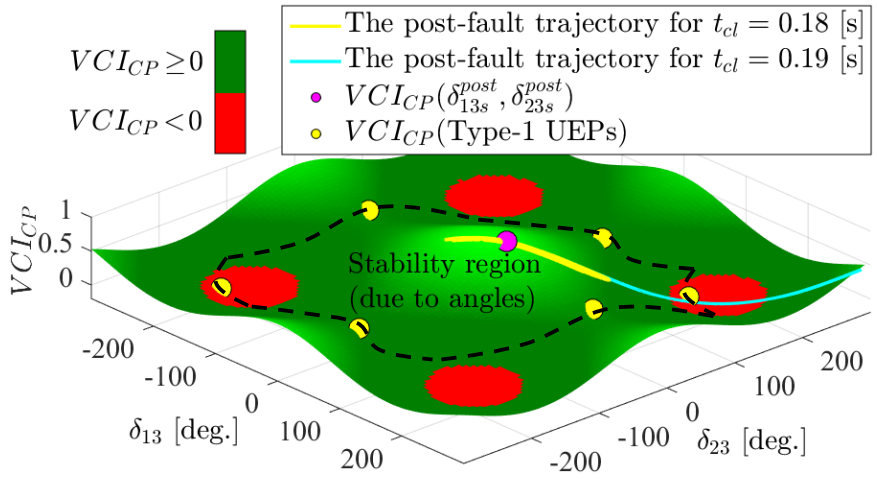

Figure 6.7: VCI_{CP} surface and post-fault trajectories in **Case 2**

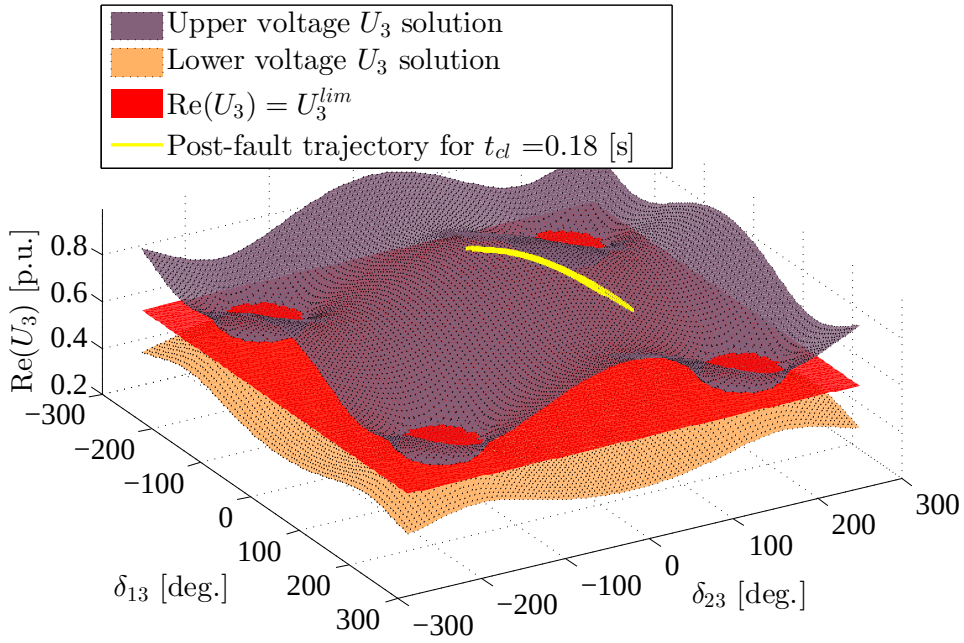

Figure 6.8: Voltage solutions and the post-fault trajectory for the case $t_{cl} = 0.18$ [s]

The critical clearing time of the fault $t_{cc} = t_{cl} = 0.18$ [s] is significantly lower compared to **Case 1**, which is an expected result. The slight increase of clearing time to $t_{cl} = 0.19$ [s] led to another, unstable trajectory along which TDS reported non-convergence issues. The problems with convergence started occurring exactly when the unstable trajectory intersected with $VCI_{CP} < 0$ area, i.e. when the blue trajectory entered the VIR.

So, what does this mean in the terms of voltage solution U_3? Figure 6.8 shows the critically stable case ($t_{cl} = 0.18$ [s]) where the yellow trajectory (obtained by TDS) moves along the surface that corresponds to the upper voltage solution U_3. In this stable case, the fault was cleared fast enough to avoid contact with the VIR. The system eventually settled at the post-fault stable operating point. On the other hand, Fig. 6.9 shows what happens in the unstable case ($t_{cl} = 0.19$ [s]).

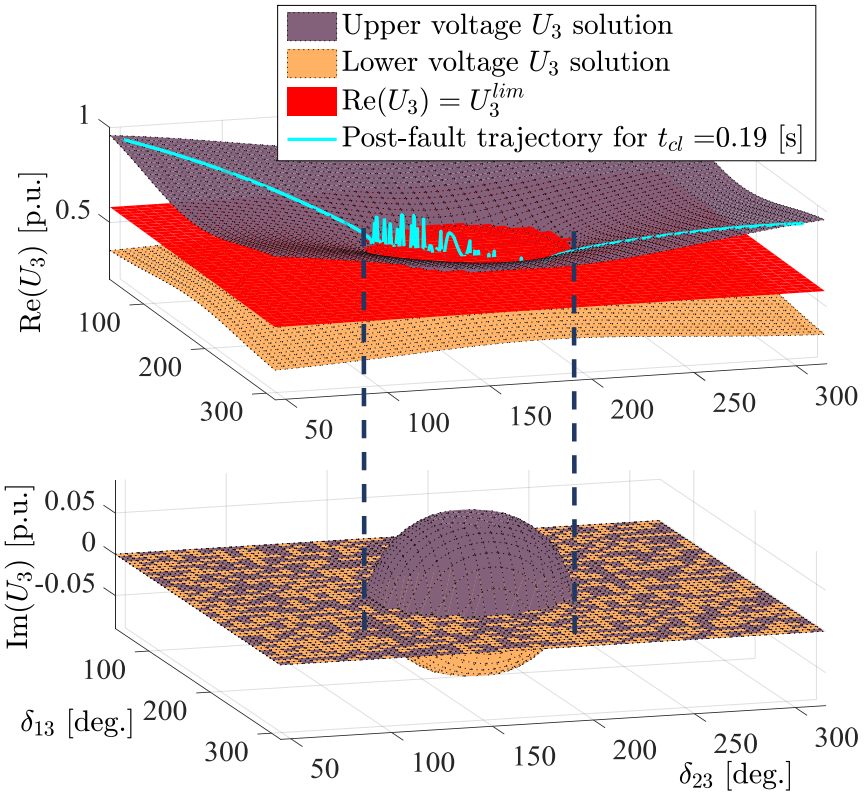

Figure 6.9: Voltage solutions and the post-fault trajectory for the case $t_{cl} = 0.19$ [s]

The clearing time $t_{cl} = 0.19$ [s] was too large to avoid entering the VIR for the given fault and set of system parameters. The TDS result shows that the magnitude of load voltage U_3 is moving along the upper voltage solution as the rotor angles swing out. After voltage U_3 drops down to the value U_3^{lim} (the point where the upper and the lower voltage solutions merge), TDS program starts complaining on non-convergence and any further result is unreliable. As it can be seen in Fig. 6.9, once the limit U_3^{lim} is crossed, both voltage solutions get non-zero imaginary components, which is not feasible when it comes to the magnitude of a phasor. The partitioned solution approach artificially continues to integrate the differential part of DAE model after U_3^{lim} is reached. This was done solely to confirm that once the dynamic trajectory exits the VIR, TDS will no longer face numerical problems. There is another way to confirm that the VIR is to blame for the convergence issues in TDS. The singularity of the algebraic Jacobian $\boldsymbol{g_y}$ can be checked directly along an unstable, dynamic trajectory by, for instance, performing the Singular Value Decomposition [182]. Figure 6.10 plots the minimum singular value min(SVD) of the algebraic Jacobian, both as a general surface and as the specific unstable post-fault trajectory (that corresponds to $t_{cl} = 0.19$ [s]).

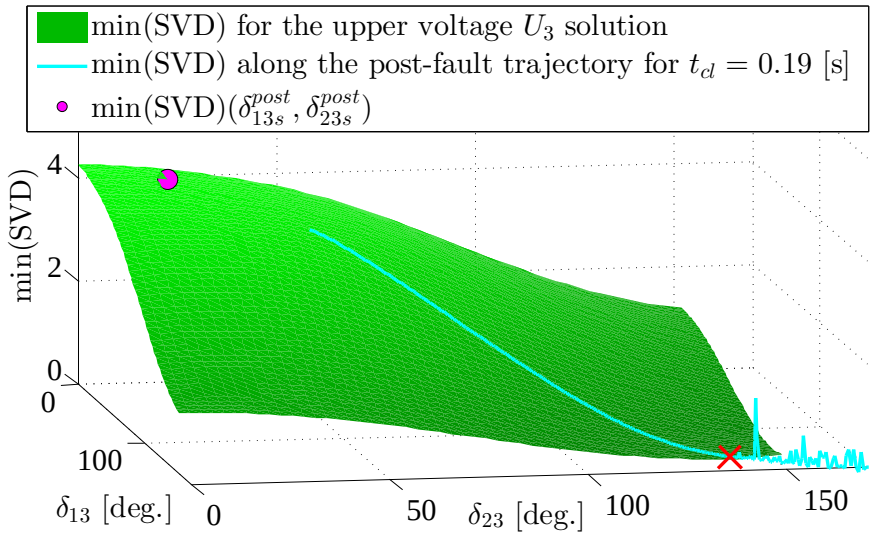

Figure 6.10: min(SVD) of the algebraic Jacobian along a post-fault trajectory

Figure 6.10 confirms that the the non-convergence issues correspond to the point (marked in red) where min(SVD)=0 along the post-fault trajectory. This is also the

point where the trajectory enters the VIR.

It has been determined that it is impossible to obtain a U_3 solution for the values of relative rotor angles that belong to a VIR. Equation (5.21) then implies that the remaining voltages cannot be obtained either (since every voltage in the system depends on U_3). Figure 6.11 represents the TDS case where the fault has been cleared too late ($t_{cl} = 0.19$ [s]) to avoid one of the VIR.

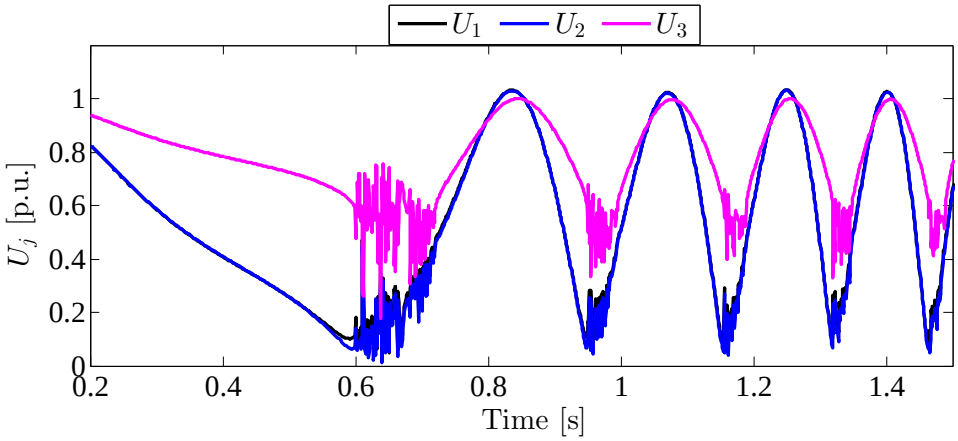

Figure 6.11: Voltages obtained by TDS (non-convergence case for $P_{l_{30}} = 8$ [p.u.])

It may be noticed that non-convergence issues emerged during simulation. When plotted in relative rotor angle space, the test system voltages behave as in Fig. 6.12.

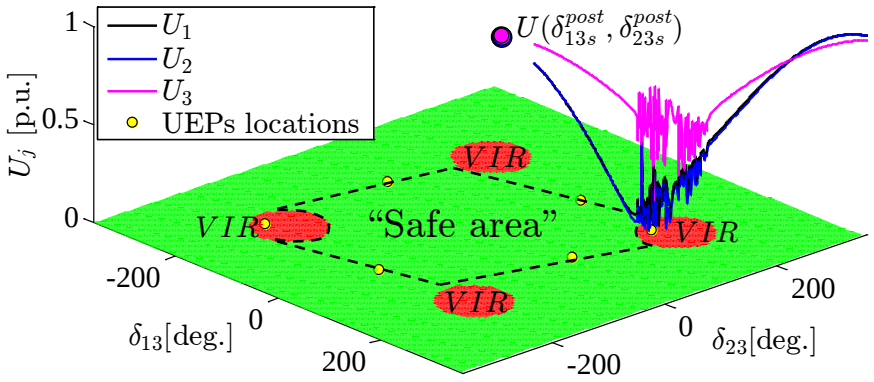

Figure 6.12: TDS-obtained voltages in relative rotor angle space ($P_{l_{30}} = 8$ [p.u.])

The unstable trajectory goes “downhill" the VCI_{CP} surface and then “meets" the VIR. Once the trajectory enters the VIR, TDS fails to solve the algebraic part of DAE. This is why all the VIR need to be removed from the “safe area" (in the terms of the existence of a DAE solution), as indicated in Fig. 6.12. The VIR of interest apparently surrounds the location $(\pi - \delta_{13s}^{post}, \pi - \delta_{23s}^{post})$. For sure, an equilibrium of the DAE system cannot belong to a VIR due to DAE being unsolvable at these singular areas. Nevertheless, this indicates that a VIR may also provide an information about the mode of machine separation. Due to the strong coupling between RAS region and VIR, it becomes more complicated to understand what is exactly the mechanism that triggers instability.

Case 3: Let the system be further loaded. The active power of the load is successively increased for 25% and 50% compared to **Case 2**. All three generators have increased their active power injections proportionally. The approximations of type-1 UEPs from (6.40) (yellow circles) and the VIR have been plotted in relative rotor angle space for each set of the post-fault parameters, as shown in Fig. 6.13. The post-fault SEP is given in magenta. It is sufficient to observe one of the VIR to get an idea about what happens when the system is stressed. This is why Fig. 6.13 shows only the first quadrant of the relative rotor angle space.

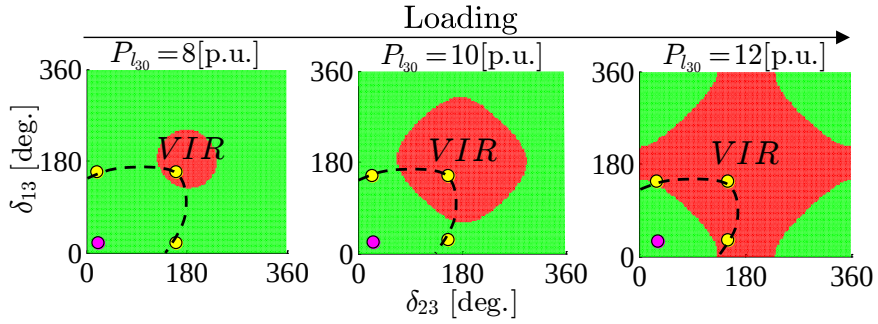

Figure 6.13: The effect of the load size on VIR

The VIR apparently expands as the system becomes more loaded. In that way, the VIR “approaches" the post-fault SEP by reducing the size of the “safe area". The reduction of the “safe area" also increases the risk that the voltage causality will be lost along a dynamic trajectory. The large VIR corresponds to the situation where the operating point OP from Fig. 5.8 (Section 5.4) is located in the proximity of the blue parabola. The loading level at which a post-fault SEP would encounter a VIR border actually represents the point of static loadability.

6.5.2 Constant current load

Another type of static load will be considered in this subsection. Typically, the constant current load has not been related with short-term voltage instability. The analytical study from Section 6.2 has demonstrated that, theoretically speaking, the constant current load model has the power to induce VIR. The study will consider the two interesting cases of system parameters ($b_R \leq 0$ and $b_R > 0$). The sign of b_R depends on the characteristic of load at bus 3. The same system model and fault as before are used. However, for the constant current load model, the VIR appears at significantly higher loading levels.

Case 4: The inductive characteristic of the load ($b_R \leq 0$) is considered first. In order for a VIR to appear, it was necessary to set up an unrealistic scenario. The complex power of the load was increased to $\bar{S}_{l_{30}} = 50 + j2.6$ [p.u.], where the two "small" generators were forced to compensate with 2 [p.u.] each ($P_{g1} = P_{g2} = 2$ [p.u.]. The third generator covers for the rest of the required power. For the inductive load, the existence of voltage solution depends on the value of the collapse indicator VCI_{CC1} along state-space, as proven in Proposition 2. The voltages obtained by TDS for an unstable case are shown in Fig. 6.14 along with VCI_{CC1}.

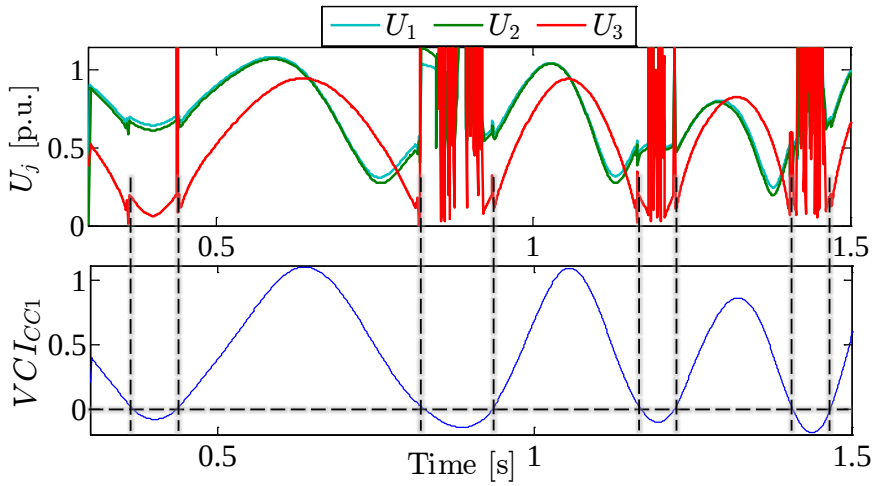

Figure 6.14: VCI_{CC1} and voltage magnitudes as obtained from TDS ($b_R \leq 0$)

The non-convergence of TDS was reported at those time instances for which voltage collapse indicator VCI_{CC1} had a negative value. This result is in line with the theoretical definition of VIR from Eq. (6.31) that is based on the value

of VCI_{CC1}. In order to confirm this analytical result, the TDS result for voltage magnitude U_3 is plotted along the relative rotor angle space in Fig. 6.15.

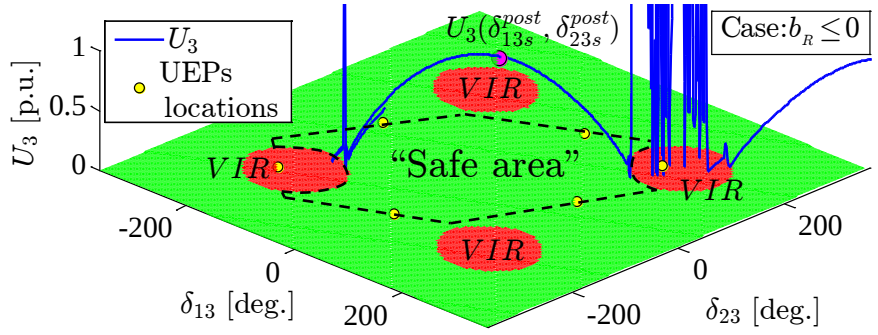

Figure 6.15: TDS-obtained voltage U_3 in relative rotor angle space ($b_R \leq 0$)

The simulation program failed to converge once the relative rotor angle positions matched with the theoretically predicted VIR.

Case 5: Changing the sign of the reactive power to $Q_{l_{30}} = -2.6$ [p.u.] resulted in the capacitive characteristic of the load at bus 3 ($b_R > 0$). Once again, the TDS was unable to converge when the trajectory intersected with the prediction of the VIR from Eq. (6.31), as shown in Fig. 6.16.

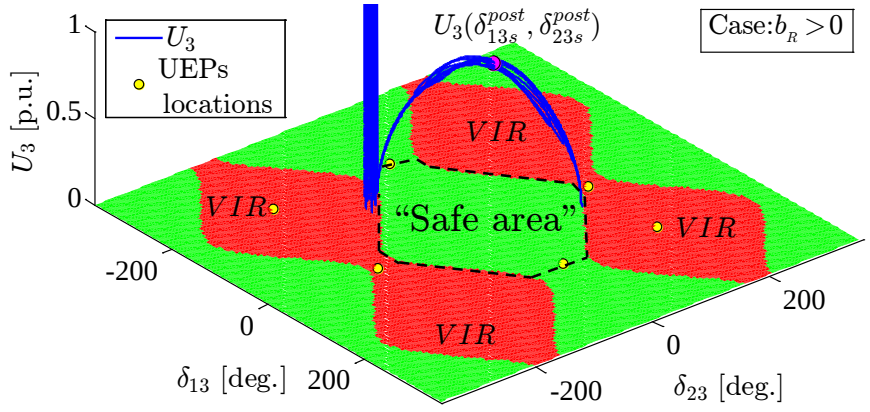

Figure 6.16: TDS-obtained voltage U_3 in relative rotor angle space ($b_R > 0$)

Based on the definition from Eq. (6.31), the loss of voltage solution occurs for different reasons in **Cases 4 and 5**. The discussion from Subsection 6.2.1 concluded

that different numbers of feasible solutions are possible depending on the values of indices VCI_{CC1} and VCI_{CC2} for $b_R > 0$. Figure 6.17 shows the mechanism of losing the voltage solution when the load at bus 3 has the capacitive, constant current characteristic. The Voltage Collapse Indicators for the Constant Current load model ($VCIs_{CC}$) are plotted along the dynamic trajectory from Fig. 6.16. The portion of the time axis where $VCIs_{CC}$ cross zero is enlarged. Three areas can be distinguished with respect to the number of feasible voltage solutions in Fig. 6.17.

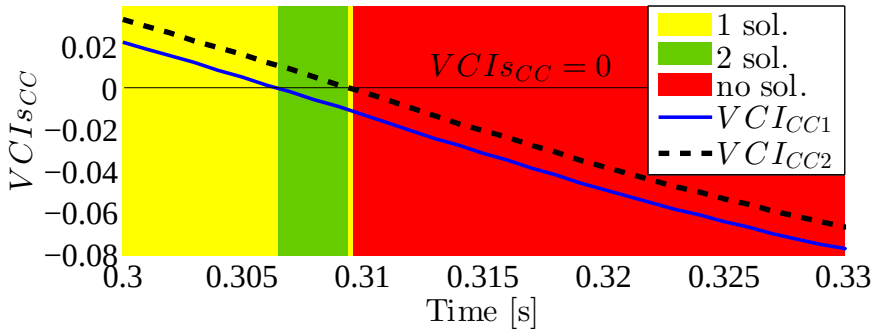

Figure 6.17: The value of $VCIs_{CC}$ along the post-fault trajectory for $b_R > 0$

Indicator VCI_{CC1} crosses zero first. Two solutions (an upper and a lower solution) exist during the short time between $VCI_{CC1} = 0$ and $VCI_{CC2} = 0$. The two solutions merge at $VCI_{CC2} = 0$, i.e. on the boundary of the VIR. There is no real and positive solution for U_3 after VCI_{CC2} becomes negative. From the practical point of view, the existence of the low solution is not important considering that the trajectory will always “move along" an upper voltage solution.

It is also important to note that once the TDS fails to converge for the first time, there is no point to continue the simulation. If TDS is not stopped, it will continue to integrate at each time step based on the values of the algebraic variables that were obtained in the last performed iteration. The ordinal number of this last iteration usually corresponds to the maximum allowed number of iterations per time step. In the case study, the TDS has been continued even after failing to converge in order to test the theoretical characterization of VIR. Surely, the differential equations are solved based on unreliable information once a VIR is encountered. One of the consequences of such approach can be seen in Figs. 6.15-6.16. In these figures it appears that the post-fault trajectory manages to “escape" from the VIR. This optimistic behavior is not to be counted on due to the fact that the existing DAE model cannot predict any dynamical behavior after a VIR is reached.

6.5.3 Constant impedance load model and its comparison with the non-linear loads

Before concluding Chapter 6, the voltage expression (6.35) for the case of constant impedance load is to be verified. This expression also proves that, when all the loads are represented by constant impedances, voltage solutions are always possible to obtain regardless of the location in state-space. This is a well-known result in the theory of power system stability. Yet, the thesis approached the problem from a different perspective.

Case 6: Let the same fault as before be repeated when the load at bus 3 in Fig. 6.5 is given as the constant impedance/admittance. Regardless of the size of the load, TDS did not exhibit any non-convergence issues. In any case, it is interesting to check if the theoretical expression from Eq. (6.35) matches the actual value of the voltage magnitude U_3 that has been calculated by TDS. The moderately loaded system (please see **Case 2**) is considered. Figure 6.18 shows the unstable post-fault trajectory (given by the blue line) for a clearing time ($t_{cl} = 0.3$ [s]) that is slightly higher than the critical clearing one ($t_{cc} = 0.29$ [s]).

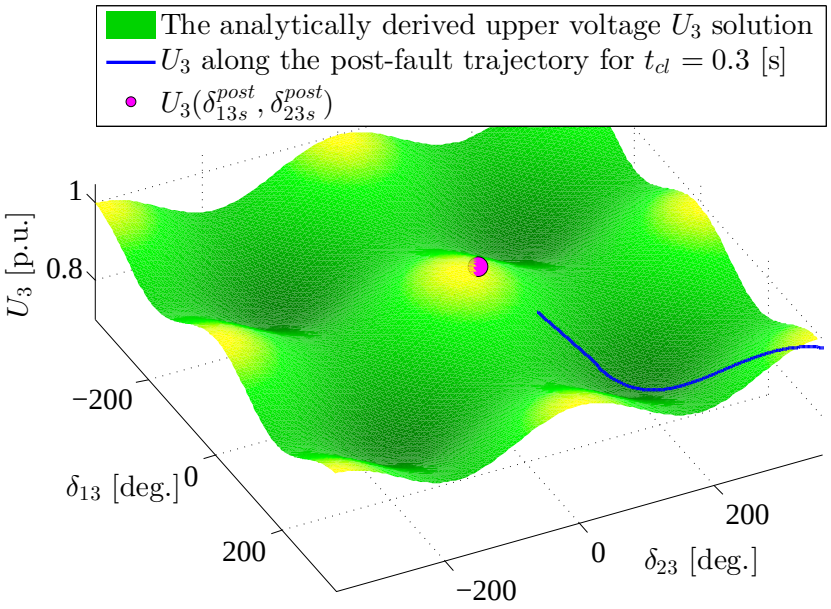

Figure 6.18: The voltage solution for the case of constant impedance load model

As it can bee seen from Fig. 6.18, the trajectory moves along the theoretically

predicted U_3 that is shown as a “green surface". The time plot of the minimum singular value of the algebraic Jacobian (min(SVD)) is also depicted for the given trajectory in Fig. 6.19. Beside this (blue-colored) trajectory, the black and red lines describe the changes of min(SVD) along unstable trajectories for the other two static, non-linear models. The three cases consider the same operating conditions.

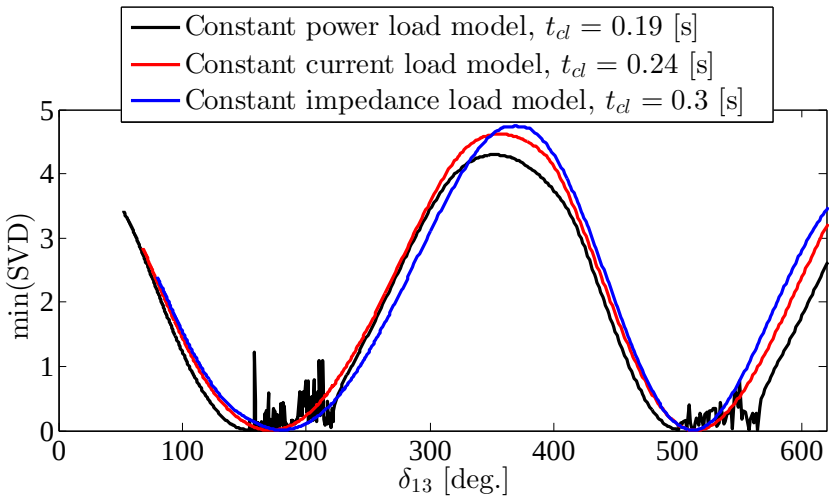

Figure 6.19: The minimum singular value along post-fault trajectories

As expected, the constant power load model led to the smallest critical clearing time. The constant power load is also the first to experience the minimum of min(SVD) along the trajectory. Additionally, the short-term instability was accompanied by the lack of convergence in TDS for the constant power load. The value of the minimum singular value dropped to zero at the border of the VIR, at the same time when non-convergence issues emerged. When the load power was switched to the constant current or constant impedance characteristics, the instability occurred due to the loss of synchronism. For these two load models, min(SVD) became very small as the rotor angles were swinging out, however, it remained positive.

In total, the constant power load appears to result in the most undesirable short-term dynamical behavior (out of the three basic static load types). Both transient instability and the loss of voltage solution along the trajectory are more likely to happen when the constant power load is employed. The constant current load carries smaller risk for both instability mechanisms and the constant impedance load cannot induce VIR at all. More general conclusions regarding VIR follow in the sequel.

6.5.4 Discussions and remarks

In order to distinguish between important and irrelevant factors that can cause the loss of voltage causality, an n-machine power system model was set up as in Section 5.5. Simple mathematical manipulations led to the voltage formulation (5.21) based on which the effect of one specific load was possible to examine. The 3-machine test system made it possible to additionally visualize the theoretically derived concepts. There are several main observations that stand out in the presented case study:

- The theoretical predictions of VIR from Eqs. (6.18)/(6.31) match with the lack of convergence of TDS along a post-fault trajectory. This indicates that the numerical issues are solely a visible consequence of the lack of voltage causality.
- VIR can be induced by both constant power and constant current load models. More load resulted in larger VIR. However, in order for a VIR to appear for the constant current load model, the system needs to be significantly more stressed than in the constant power case. Constant impedance loads never cause VIR.
- The developed collapse indicators-VCI_{CP} and $VCIs_{CC}$ performed well. The indicators are capable both to (i) detect the intersection of a trajectory with a VIR and also (ii) to assess the number of voltage solutions.

Coming back to the list from Section 1.4, it may be concluded that Chapters 5 and 6 made the following contributions (that have been reported and published in [176]):

1. (2.1S): The system voltages have been expressed in a convenient form. Wherever these voltages can not be defined as the closed form expressions of state-variables, the loss of voltage causality can be expected.
2. (2.2S): The analysis of the load voltage solution resulted in the theoretical definition of Voltage Impasse Regions (VIR) for the constant power and constant current loads. VIR are identified as the regions of the state-space that satisfy specific trigonometric criteria. Voltage Collapse Indicators (VCIs) have also been developed to simplify the analysis and provide some kind of measure of distance to a “voltage collapse" along a dynamic trajectory.

The basic mechanism of VIR appearance in relation to static load models is now understood. The VIR represents a structural problem of the DAE model and the further generalization of the VIR concept in the terms of modeling is relevant. To incorporate the concept of VIR into short-term stability analysis is an important step to be taken on the way towards more advanced DSA tools.

Chapter 7

Conclusions and Future Work

The final chapter of the thesis will draw the main conclusions based on the presented work by placing the thesis contributions in the framework of DSA. The advantages and possibilities for the improvement of developed approaches are discussed, as well. As the closure of the thesis, the plan for the future work is proposed.

The scientific topic of Dynamic Security Assessment (DSA) is wide and grasps multiple issues. This thesis has addressed some of the basic requirements that are imposed on DSA—the maintenance of the machine synchronism and the existence of voltage solution along a transient trajectory. In that sense, the presented work is a combination of transient stability and short-term voltage stability assessment. The work is mostly academically oriented, i.e. it provides a theoretical insight into the characteristics and topology of the short-term stability region that is associated to large disturbances.

Nevertheless, the application of the developed concepts on large-scale multi-machine systems is not to be excluded. The idea of security boundaries in parameter-space has a potential to provide an instant, on-line answer about the degree of system security. Additionally, it has been shown that it is necessary to account for the instability mechanism that originates from the structural properties of the set of DAE. There is no commercial software that can correctly carry out short-term stability assessment for the non-linear models that are mathematically “unsolvable".

The two main segments are distinguished in the thesis. Chapters 3 and 4 proposed the idea of the parametrization of RAS region, while Chapters 5 and 6 introduced Voltage Impasse Region (VIR) as a topological structure that is inherent to power systems that employ non-linear static load models. The corresponding conclusions and the possibilities for the further development of the ideas follow.

7.1 Conclusions

The existing DSA methods (TDS, direct methods) evaluate short-term RAS at each operating point with respect to the list of critical contingencies. The extensive process requires time and therefore, it is usually carried out in the system planning phase. The idea to parametrize RAS boundary originated from the need to enable a direct assessment of transient stability when an operating state is perturbed. The goal of the proposed approach was to speed up RAS assessment by providing a sufficiently accurate security boundaries in analytical form. The short summary of the contributions and conclusions from Chapters 3 and 4 is provided in the sequel.

- Chapter 3 proposes an algorithm and a procedure to construct the parametrized security boundaries as polynomial functions of powers of interest. The polynomials had satisfactory performance—it is shown that the number of data points does not have to be large such that the high level of estimation accuracy is maintained. This property makes it convenient to use TDS as a data acquisition tool due to its superiority in the terms of accuracy and modeling possibilities (compared to e.g. direct methods).

- Chapter 3 also proves that the estimation accuracy of the proposed method increases with the introduction of a more appropriate parameter-space basin. “More appropriate" basin here refers to the choice of parameter-space axis that has some physical meaning. Since the outputs of the method are the estimates of the critical clearing time (t_{cc}), the expression for finding t_{cc} is a logical choice. The improved parametrization from Chapter 4 involves an additional step since the analytical expression for finding t_{cc} is available for SMIB system. This step includes the identification of SIME-equivalent of the power system. The new, SIME-based parametrization, selects the data points in a pattern that better reflects the physical properties of a machine separation after a disturbance. Such approach results in an increased accuracy of the estimation.

- In Chapter 4, the SIME-parametrization is also subject to “conservativeness constraint" in order to acquire this advantageous characteristic of direct methods. The impact of the imposed constraint on the accuracy of estimation is not large, while the number of overestimates decreases significantly.

The accuracy of the proposed constrained SIME-parametrization increases with the number of parameter-space dimensions (which corresponds to the number of generators whose powers are included in the definition of parameter-space basin).

Alongside the fact that any type of component modeling is allowed in the proposed method, the outcomes of SIME-based parametrization are encouraging.

The developed parametrization methodology assumes that there are no limitations when it comes to solving DAE by TDS program. Chapters 5 and 6 have proven that this is not necessarily the case. The two chapters have addressed the loss of voltage causality that is load-modeling-related. This problem is not recognized by the scientific community as one of the widely known short-term voltage instability phenomena that are considered to be mainly driven by load dynamics. And indeed, the voltage stability is not investigated here from the point of acceptable/unacceptable values of voltage profiles. The focus is a short-term phenomenon for which voltage solutions do not exist at all based on DAE model. A comprehensive analysis is carried out in Chapters 5 and 6 in order to extend the concept of “impasse/singularity surfaces" and understand the relationship between the non-linear static load models and the loss of voltage solution. The efforts were not in vain. There are indeed state-space areas, introduced here as Voltage Impasse Regions (VIR), where voltage solutions are lost due to the inflexible, non-linear static load characteristic. Moreover, with static load models being widely used in simulation programs (and some TSOs certainly employ these models), the short-term stability assessment can become unreliable or even worse, impossible. There are several conclusions that stand out in relation to the work presented in Chapters 5 and 6:

- The idea of VIR is first presented in Chapter 5 where also an illustrative example of SMIB system explains the mechanism of VIR appearance when a load is of constant power type. An interesting conclusion is that the VIR is similar in nature to the problem of static loadability. However, a VIR is located in the neighborhood of a post-fault SEP that belongs to a “safe zone" in the terms of loadability. In such case, a VIR can only be encountered along a transient trajectory as the rotor angles move in state-space. Chapter 5 also formulates the problem in a more general way such that VIR can be defined for the multi-machine case.

- The careful analysis of the voltage solutions from Chapter 5 shows that voltage causality can be lost at certain state-space positions due to (i) voltage magnitude solutions merging and becoming complex numbers (for the constant power and capacitive constant current load) or (ii) due to both voltage magnitudes becoming negative (the case of inductive constant current load). The voltage stability is certainly challenged once the voltage levels drop drastically shortly before the voltage solution is completely lost. The VIR is the set of all those combinations

of relative rotor angles for which it does not exist any feasible (positive and real) solution for the load voltage magnitude. In a sense, the VIR is a “black hole" for the DAE model—it is an area of the state-space where the set of algebraic equations is unsolvable.

- VIR appear on the border of the stability region and grow with respect to the amount of load. Hence, larger disturbances and non-linear loads increase the risk of encountering a VIR. As a consequence of the intersection of a post-fault trajectory with a VIR, every TDS program would fail.

Currently, there is no mathematical or numerical tool that can describe the dynamics of a power system inside a VIR. Since there is no guarantee that a dynamic trajectory will not “end up" in the vicinity of a VIR, the only recommendation is to completely avoid operating points that have VIR in their neighborhood. Due to its strong interaction with both loss of synchronism and voltage instability, the concept of VIR should be further developed.

7.2 Future work

This thesis raises many interesting questions related to short-term dynamics of large disturbances. The novel SIME-parametrization and the theoretical foundation of VIR are presented. The initial development of ideas usually involves simple models that enable clear understanding of the underlaying mechanisms leading to interesting phenomena. Hence, there is large space for improvement, in particular in the sense of application of proposed concepts to larger systems. Regarding the short-term RAS study and SIME-parametrization, there are several research directions to be addressed in future:

- The boundaries that are constructed based on the constrained SIME-parametrization from Chapter 4 should in future be used in the “opposite" direction. TSOs are usually interested in the maximum amount of power that can be transmitted via some weak link or they want to know about the critical amount of load that is possible to supply in one area. By reversing the polynomial function, a certain, expected range of the times at which the protective system reacts may be mapped into corresponding areas of the parameter-space. By doing that, parameter-space can be partitioned into e.g. safe, critical and loss of synchronism modes of operation with respect to the list of critical faults.

- Such “reversed" boundaries could be tested by using larger power system models with more sophisticated representation of components. There are no modeling limitations in SIME-parametrization as long as a TDS can be carried out.

So what happens when a TDS cannot be carried out? If some of the loads are of the static, non-linear type, it should be checked if a VIR is to blame for the failure of the TDS. The following research lines can improve the understanding of VIR and lead to the application of the VIR concept to more realistic power system models:

- The cumulative effect of several non-linear static loads is the first to be investigated. This study will aim to understand the effect of the non-linear load (especially the ZIP load) interaction on VIR. ZIP model is interesting since it contains all three static load components. Also, when it comes to loads, the classical short-term voltage stability studies have always included load dynamics. It would be beneficial to test how the different voltage-connected instability mechanisms overlap and which of the two mechanisms is more critical.

- More detailed generator modeling should be taken into account. It is more challenging to obtain closed form expressions when additional state-space variables are in the game. However, rotor angles experience larger changes compared to some other state-space variables (e.g. E_i' in one-axis model). The VIR is, therefore, a phenomenon that is considered to be mainly rotor-angle-driven.

- There are three voltage collapse indicators (VCIs) that have been developed to detect the singularity of the algebraic Jacobian along a trajectory. An option to construct similar indicators should definitely be considered for the case of multiple non-linear loads. VCIs are convenient tool when it comes to “measuring the distance" from a voltage instability such that a voltage collapse can potentially be avoided. Besides, the computation of these indicators is computationally less demanding than, for instance, a matrix factorization which results in min(SVD).

In the broad scope of Dynamic Security Assessment (DSA), this thesis attempts to contribute by evaluating some fundamental properties of non-linear power systems. The application of academic research work as a tool for an actual power system is a process that consists of many intermediate steps. In this thesis, the initial steps are taken to fuse two different (however, strongly coupled) short-term instability mechanisms. This strong coupling originates from the generic problem that lies in the very structure of DAE model. Such phenomena that can jeopardize the standard power system model to the extent of structural inconsistency are certainly worth of further research such that appropriate countermeasures can be proposed.

Bibliography

[1] T. P. Hughes, *Networks of Power: Electrification in Western Society, 1880-1930*. Baltimore, MD: The John Hopkins University Press, 1983.

[2] B. Bowers, *A History of Electric Light & Power*. Stevenage, UK: Peter Peregrinus Ltd., 1982.

[3] D. Morton, *Power: A Survey History of Electric Power Technology Since 1945*. New Brunswick, NJ: IEEE History Center, 2000.

[4] D. Morton, “Reviewing the history of electric power and electrification," *Endeavour*, vol. 26, no. 2, pp. 60-63, June 2002.

[5] P. Pourbeik, P. S. Kundur and C. W. Taylor, “The anatomy of a power grid blackout - Root causes and dynamics of recent major blackouts," *IEEE Power Energy Mag.*, vol. 4, no. 5, pp. 22-29, Sep.-Oct. 2006.

[6] G. Andersson *et al.*, “Causes of the 2003 major grid blackouts in North America and Europe, and recommended means to improve system dynamic performance," *IEEE Trans. Power Syst.*, vol. 20, no. 4, pp. 1922-1928, Oct. 2005.

[7] J. P. Conti, “The day the samba stopped," *IET Eng. Technol.*, vol. 5, no. 4, pp. 46-47, Apr. 2010.

[8] S. Sarkar *et al.*, “Indian experience on smart grid application in blackout control," *2015 39th National Systems Conference (NSC)*, Noida, 2015, pp. 1-6.

[9] G. C. Loehr, “The “good” blackout: The Northeast power failure of 9 November 1965 [History]," *IEEE Power Energy Mag.*, vol. 15, no. 3, pp. 84-96, May-June 2017.

[10] Q. Chen *et al.*, “Review on blackout process in China southern area main power grid in 2008 snow disaster," *2009 IEEE Power & Energy Society General Meeting*, Calgary, AB, 2009, pp. 1-8.

[11] J. A. Laghari *et al.*, “Application of computational intelligence techniques for load shedding in power systems: A review," *Energy Convers. Manag.*, vol. 75, pp. 130-140, Nov. 2013.

[12] S. Guillon *et al.*, “A colorful blackout: The havoc caused by auroral electrojet generated magnetic field variations in 1989," *IEEE Power Energy Mag.*, vol. 14, no. 6, pp. 59-71, Nov.-Dec. 2016.

[13] C. Li, Y. Sun and X. Chen,“Analysis of the blackout in Europe on November 4, 2006," *2007 International Power Engineering Conference (IPEC 2007)*, Singapore, 2007, pp. 939-944.

[14] B. Backwell, *Wind Power: The Struggle for Control of a New Global Industry*. Abingdon, UK: Routledge, 2018.

[15] V. Madani *et al.*, “Challenging changing landscapes: Implementing synchrophasor technology in grid operations in the WECC region," *IEEE Power Energy Mag.*, vol. 13, no. 5, pp. 18-28, Sep.-Oct. 2015.

[16] J. J. Romero, “Blackouts illuminate India’s power problems," *IEEE Spectr.*, vol. 49, no. 10, pp. 11-12, Sep. 2012.

[17] U. Häger, C. Rehtanz and N. Voropai, *Monitoring, Control and Protection of Interconnected Power Systems*. Berlin Heidelberg, Germany: Springer-Verlag, 2014.

[18] J. Lin and F. H. Magnago, *Electricity Markets: Theories and Applications*. Hoboken, NJ: Wiley, 2017.

[19] L. Freris and D. Infield, *Renewable Energy in Power Systems*. Chichester, UK: Wiley, 2008.

[20] M. Eremia, C. C. Liu and A. A. Edris, *Advanced Solutions in Power Systems: HVDC, FACTS, and Artificial Intelligence*. Hoboken, NJ: Wiley, 2016.

[21] N. Nguyen and J. Mitra, “An analysis of the effects and dependency of wind power penetration on system frequency regulation," *IEEE Trans. Sustain. Energy*, vol. 7, no. 1, pp. 354-363, Jan. 2016.

[22] L. L. Grigsby, *Power Systems*. Boca Raton, FL: CRC Press, Taylor and Francis Group, 2007.

[23] P. M. Anderson and A. Bose, “A probabilistic approach to power system stability analysis," *IEEE Trans. Power App. Syst.*, vol. PAS-102, no. 8, pp. 2430-2439, Aug. 1983.

[24] S. C. Savulescu, *Real-Time Stability Assessment in Modern Power System Control Centers*. Hoboken, NJ: Wiley, 2009.

[25] R. Sunitha, R. S. Kumar and A. T. Mathew, “Online static security assessment module using artificial neural networks," *IEEE Trans. Power Syst.*, vol. 28, no. 4, pp. 4328-4335, Nov. 2013.

[26] K. Morison, L. Wang and P. Kundur, “Power system security assessment," *IEEE Power Energy Mag.*, vol. 2, no. 5, pp. 30-39, Sep.-Oct. 2004.

[27] T. E. Dy Liacco, “The adaptive reliability control system," *IEEE Trans. Power App. Syst.*, vol. PAS-86, no. 5, pp. 517-531, May 1967.

[28] C. T. Leondes, *Control and Dynamic Systems, Volume 41: Analysis and Control System Techniques for Electric Power Systems*. San Diego, CA: Academic Press, 1991.

[29] L. H. Fink and K. Carlsen, “Operating under stress and strain (electrical power systems control under emergency conditions)," *IEEE Spectr.*, vol. 15, no. 3, pp. 48-53, Mar. 1978.

[30] J. Condren, T. W. Gedra and P. Damrongkulkamjorn, “Optimal power flow with expected security costs," *IEEE Trans. Power Syst.*, vol. 21, no. 2, pp. 541-547, May 2006.

[31] S. Sastry and P. Varaiya, “Hierarchical stability and alert state steering control of interconnected power systems," *IEEE Trans. Circuits Syst.*, vol. 27, no. 11, pp. 1102-1112, Nov. 1980.

[32] M. Begovic *et al.*, “Wide-area protection and emergency control," *Proc. IEEE*, vol. 93, no. 5, pp. 876-891, May 2005.

[33] T. Sakaguchi and K. Matsumoto, “Development of a knowledge based system for power system restoration," *IEEE Trans. Power App. Syst.*, vol. PAS-102, no. 2, pp. 320-329, Feb. 1983.

[34] L. L. Grigsby, *Power Systems Stability and Control*. Boca Raton, FL: CRC Press, Taylor and Francis Group, 2007.

[35] J. Machowski, J. W. Bialek and J. R. Bumby, *Power System Dynamics and Stability*. Chichester, UK: Wiley, 1997.

[36] Commission Regulation (EU) 2017/1485, "Establishing a guideline on electricity transmission system operation," *Official Journal of the European Union*, Document 32017R1485, Aug. 2, 2007. [Online]. Available: https://eur-lex.europa.eu. [Accessed: 25.8.2017].

[37] S. C. Savulescu, *Real-Time Stability Assessment in Power Systems: Techniques for Early Detection of the Risk of Blackout*. New York, NY: Springer, 2014.

[38] A. A. Fouad *et al.*, "Dynamic security assessment practices in North America," *IEEE Trans. Power Syst.*, vol. 3, no. 3, pp. 1310-1321, Aug. 1988.

[39] G. C. Ejebe *et al.*, "Online dynamic security assessment in an EMS," *IEEE Comput. Appl. Power*, vol. 11, no. 1, pp. 43-47, Jan. 1998.

[40] K. Demaree *et al.*, "An on-line dynamic security analysis system implementation," *IEEE Trans. Power Syst.*, vol. 9, no. 4, pp. 1716-1722, Nov. 1994.

[41] R. Schainker *et al.*, "Real-time dynamic security assessment: fast simulation and modeling applied to emergency outage security of the electric grid," *IEEE Power Energy Mag.*, vol. 4, no. 2, pp. 51-58, Mar.-Apr. 2006.

[42] Y. Mansour *et al.*, "Large scale dynamic security screening and ranking using neural networks," *IEEE Trans. Power Syst.*, vol. 12, no. 2, pp. 954-960, May 1997.

[43] K. Tomsovic *et al.*, "An expert system as a dispatchers' aid for the isolation of line section faults," *IEEE Trans. Power Syst.*, vol. 2, no. 3, pp. 736-743, July 1987.

[44] M. A. El-Kady *et al.*, "Dynamic security assessment utilizing the transient energy function method," *IEEE Trans. Power Syst.*, vol. 1, no. 3, pp. 284-291, Aug. 1986.

[45] M. Pavella, D. Ernst and D. Ruiz-Vega, *Transient Stability of Power Systems: A Unified Approach to Assessment and Control.* Norwell, MA: Kluwer Academic Publishers, 2000.

[46] M. J. Laufenberg and M. A. Pai, “A new approach to dynamic security assessment using trajectory sensitivities," *IEEE Trans. Power Syst.*, vol. 13, no. 3, pp. 953-958, Aug. 1988.

[47] L. Wehenkel, T. V. Cutsem and M. Ribbens-Pavella, “An artificial intelligence framework for online transient stability assessment of power systems," *IEEE Trans. Power Syst.*, vol. 4, no. 2, pp. 789-800, May 1989.

[48] L. Wehenkel, T. V. Cutsem and M. Ribbens-Pavella, “Inductive inference applied to on-line transient stability assessment of electric power systems," *Automatica*, vol. 25, no. 3, pp. 445-451, May 1989.

[49] L. Wehenkel and M. Pavella, “Decision trees and transient stability of electric power systems," *Automatica*, vol. 27, no. 1, pp. 115-134, Jan. 1991.

[50] A. Kaci *et al.*, “Synchrophasor data baselining and mining for online monitoring of dynamic security limits," *IEEE Trans. Power Syst.*, vol. 29, no. 6, pp. 2681-2695, Nov. 2014.

[51] K. Sun *et al.*, “An online dynamic security assessment scheme using phasor measurements and decision trees," *IEEE Trans. Power Syst.*, vol. 22, no. 4, pp. 1935-1943, Nov. 2007.

[52] A. A. Fouad, S. Vekataraman and J. A. Davis, “An expert system for security trend analysis of a stability-limited power system," *IEEE Trans. Power Syst.*, vol. 6, no. 3, pp. 1077-1084, Aug. 1991.

[53] V. Chadalavada *et al.*, “An on-line contingency filtering scheme for dynamic security assessment," *IEEE Trans. Power Syst.*, vol. 12, no. 1, pp. 153-161, Feb. 1997.

[54] P. Kundur, *Power System Stability and Control*. New York, NY: McGraw-Hill, 1994.

[55] IEEE/CIGRE joint task force on stability terms and definitions, “Definition and classification of power system stability," *IEEE Trans. Power Syst.*, vol. 19, no. 3, pp. 1387-1401, Aug. 2004.

[56] P. W. Sauer and M. A. Pai, *Power System Dynamics and Stability*. Upper Saddle River, NJ: Prentice Hall, 1998.

[57] I. Tyuryukanov *et al.*, “Discovering clusters in power networks from orthogonal structure of spectral embedding," *IEEE Trans. Power Syst.*, vol. 33, no. 6, pp. 6441-6451, Nov. 2018.

[58] CIGRE Task Force 38.02.14 Rep., “Analysis and Modeling Needs of Power Systems Under Major Frequency Disturbances," Jan. 1999.

[59] M. Klein *et al.*, “Analytical investigation of factors influencing power system stabilizers performance," *IEEE Trans. Energy Convers.*, vol. 7, no. 3, pp. 382-390, Sep. 1992.

[60] K. Kawabe and K. Tanaka, “Analytical method for short-term voltage stability using the stability boundary in the P-V plane," *IEEE Trans. Power Syst.*, vol. 29, no. 6, pp. 3041-3047, Nov. 2014.

[61] C. W. Taylor, *Power System Voltage Stability*. New York, NY: McGrawHill, 1994.

[62] IEEE/PES Power System Stability Subcommittee Special Publication, “Voltage stability assessment, procedures, and guides," IEEE PES Tech. Rep. PES-TR9, Aug. 2002.

[63] Y. Dong and H. R. Pota, “Fast transient stability assessment using large step-size numerical integration (power systems)," *IEE Proc. Inst. Generat. Transm. Distrib.*, vol. 138, no. 4, pp. 377-383, July 1991.

[64] G. A. Maria, C. Tang and J. Kim, “Hybrid transient stability analysis (power systems)," *IEEE Trans. Power Syst.*, vol. 5, no. 2, pp. 384-393, May 1990.

[65] P. C. Magnusson, “The transient-energy method of calculating stability," *AIEE Trans.*, vol. 66, no. 1, pp. 747-755, Jan. 1947.

[66] P. D. Aylett, “The energy-integral criterion of transient stability limits of power systems," *IEE Proc. C*, vol. 105, no. 8, pp. 527-536, Sep. 1958.

[67] G. E. Gless, “Direct method of Liapunov applied to transient power system stability," *IEEE Trans. Power App. Syst.*, vol. PAS-85, no. 2, pp. 159-168, Feb. 1966.

[68] A. H. El-Abiad and K. Nagappan, “Transient stability regions of multimachine power systems," *IEEE Trans. Power App. Syst.*, vol. PAS-85, no. 2, pp. 169-179, Feb. 1966.

[69] H. D. Chiang, *Direct Methods for Stability Analysis of Electric Power Systems: Theoretical Foundation, BCU Methodologies, and Applications*. Hoboken, NJ: Wiley, 2010.

[70] A. A. Fouad and V. Vittal, *Power System Transient Stability Analysis Using the Transient Energy Function Method*. Upper Saddle River, NJ: Prentice Hall, 1992.

[71] H. D. Chiang, F. F. Wu and P. P. Varaiya, “A BCU method for direct analysis of power system transient stability," *IEEE Trans. Power Syst.*, vol. 9, no. 3, pp. 1194-1208, Aug. 1994.

[72] F. S. Prabhakara and A. H. El-Abiad, “A simplified determination of transient stability regions for Lyapunov methods," *IEEE Trans. Power App. Syst.*, vol. 94, no. 2, pp. 672-689, Mar. 1975.

[73] B. Berggren and G. Andersson, “On the nature of unstable equilibrium points in power systems", *IEEE Trans. Power Syst.*, vol. 8, no. 2, pp. 738-745, May 1993.

[74] M. Anghel, F. Milano and A. Papachristodoulou, “Algorithmic construction of Lyapunov functions for power system stability analysis," *IEEE Trans. Power Syst.*, vol. 60, no. 9, pp. 2533-2546, Feb. 2013.

[75] H. R. Pota and P. J. Moylan, “A new Lyapunov function for interconnected power systems," *IEEE Trans. Autom. Control*, vol. 37, no. 8, pp. 1192-1196, Aug. 1992.

[76] N. G. Bretas and L. F. C. Alberto, “Lyapunov function for power systems with transfer conductances: extension of the Invariance principle," *IEEE Trans. Power Syst.*, vol. 18, no. 2, pp. 769-777, May 2003.

[77] D. Ruiz-Vega and M. Pavella, “A comprehensive approach to transient stability control: Part I-Near optimal preventive control," *IEEE Trans. Power Syst.*, vol. 18, no. 4, pp. 1446-1453, Nov. 2003.

[78] D. Ruiz-Vega and M. Pavella, “A comprehensive approach to transient stability control: Part II-Open loop emergency control," *IEEE Trans. Power Syst.*, vol. 18, no. 4, pp. 1454-1460, Nov. 2003.

[79] D. Chatterjee and A. Ghosh, “Transient stability assessment of power systems containing series and shunt compensators," *IEEE Trans. Power Syst.*, vol. 22, no. 3, pp. 1210-1220, Aug. 2007.

[80] A. D. Patton, “Assessment of the security of operating electric power systems using probability methods," *Proc. IEEE*, vol. 62, no. 7, pp. 892-901, July 1974.

[81] Y. H. Pao and D. J. Sobajic, “Combined use of unsupervised and supervised learning for dynamic security assessment," *IEEE Trans. Power Syst.*, vol. 7, no. 2, pp. 878-884, May 1992.

[82] D. J. Sobajic and Y. H. Pao, “An artificial intelligence system for power system contingency screening," *IEEE Trans. Power Syst.*, vol. 3, no. 2, pp. 647-653, May 1988.

[83] E. Hobson and G. N. Allen, “Effectiveness of artificial neural networks for first swing stability determination of practical systems", *IEEE Trans. Power Syst.*, vol. 9, no. 2, pp. 1062-1068, May 1994.

[84] H. Wu and I. Dobson, “Cascading stall of many induction motors in a simple system," *IEEE Trans. Power Syst.*, vol. 27, no. 4, pp. 2116-2126, Nov. 2012.

[85] I. A. Hiskens and D. J. Hill, “Energy functions, transient stability and voltage behaviour in power systems with nonlinear loads," *IEEE Trans. Power Syst.*, vol. 4, no. 4, pp. 1525-1533, Nov. 1989.

[86] V. Venkatasubramanian, H. Schattler and J. Zaborszky, “Voltage dynamics: Study of a generator with voltage control, transmission, and matched MW load," *IEEE Trans. Autom. Control*, vol. 37, no. 11, pp. 1717-1733, Nov. 1992.

[87] K. C. A. Smith and R. E. Alley, *Electrical Circuits: An Introduction*. Cambridge, UK: Cambridge University Press, 1992.

[88] M. Klein, G. J. Rogers and P. Kundur, “A fundamental study of inter-area oscillations in power systems," *IEEE Trans. Power Syst.*, vol. 6, no. 3, pp. 914-921, Aug. 1991.

[89] P. Kundur *et al.*, “Application of power system stabilizers for enhancement of overall system stability," *IEEE Trans. Power Syst.*, vol. 4, no. 2, pp. 614-626, May 1989.

[90] M. H. J. Bollen and F. Hassan, *Integration of Distributed Generation in the Power System*. Hoboken, NJ: Wiley, 2011.

[91] M. Pavella and P. G. Murthy, *Transient Stability of Power Systems: Theory and Practice*. Hoboken, NJ: Wiley, 1994.

[92] IEEE Task Force on Load Representation for Dynamic Performance, "Load Representation For Dynamic Performance Analysis," *IEEE Trans. Power Syst.*, vol. 8, no. 2, pp. 472-482, May 1993.

[93] A. R. Bergen, *Power System Analysis*. Upper Saddle River, NJ: Prentice-Hall, 1986.

[94] A. R. Bergen and D. J. Hill, "A structure preserving model for power system stability analysis," *IEEE Trans. Power App. Syst.*, vol. PAS-100, no. 1, pp. 25-35, Jan. 1981.

[95] M. A. Pai, *Energy Function Analysis for Power System Stability*. Boston, MA: Kluwer Academic Publishers, 1989.

[96] B. Stott, "Power system dynamic response calculations," *Proc. IEEE*, vol. 67, no. 2, pp. 219-241, Feb. 1979.

[97] G. W. Stagg and A. H. El-Abiad, *Computer Methods in Power System Analysis*. New York, NY: McGraw-Hill, 1968.

[98] F. Milano, *Power System Modelling and Scripting*. London, UK: Springer-Verlag, 2010.

[99] C. T. Kelley, *Iterative Methods for Linear and Nonlinear Equations*. Philadelphia, PA: SIAM, 1995.

[100] E. Hairer, C. Lubich and M. Roche, *The Numerical Solution of Differential-Algebraic Systems by Runge-Kutta Methods*. Berlin Heidelberg, Germany: Springer-Verlag, 1989.

[101] J. R. Dormand, *Numerical Methods for Differential Equations: A Computational Approach*. Boca Raton, FL: CRC Press LLC, 1996.

[102] K. E. Atkinson, W. Han and D. E. Stewart, *Numerical Solution of Ordinary Differential Equations*. Hoboken, NJ: Wiley, 2009.

[103] J. R. Dormand and P. J. Prince, “A family of embedded Runge-Kutta formulae," *J. Comput. Appl. Math.*, vol. 6, no. 1, pp. 19-26, Mar. 1980.

[104] W. Sun and Y. X. Yuan, *Optimization Theory and Methods: Nonlinear Programming*. New York, NY: Springer, 2006.

[105] D. G. Luenberger and Y. Ye, *Linear and Nonlinear Programming*. New York, NY: Springer, 2008.

[106] P. Wriggers, *Nonlinear Finite Element Methods*. Berlin Heidelberg, Germany: Springer-Verlag, 2008.

[107] J. Noye, *Computational Techniques for Differential Equations*. Amsterdam, NL: Elsevier Science Publishers, 1984.

[108] H. D. Chiang, M. W. Hirsch and F. F. Wu, “Stability regions of non-linear autonomous dynamical systems," *IEEE Trans. Autom. Control*, vol. 33, no. 1, pp. 16-27, Jan. 1988.

[109] C. W. Liu and J. S. Thorp, “A novel method to compute the closest unstable equilibrium point for transient stability region estimate in power systems," *IEEE Trans. Circuits Syst. I, Fundam. Theory Appl.*, vol. 44, no. 7, pp. 630-635, July 1997.

[110] H. D. Chiang, F. F. Wu and P. P. Varaiya, “Foundations of direct methods for power system transient stability analysis," *IEEE Trans. Circuits Syst.*, vol. 34, no. 2, pp. 160-173, Feb. 1987.

[111] H. K. Khalil, *Nonlinear Systems*. Upper Saddle River, NJ: Prentice-Hall, 2002.

[112] K. R. Padiyar, *Structure Preserving Energy Functions in Power Systems: Theory and Applications*. Boca Raton, FL: CRC Press, Taylor and Francis Group, 2013.

[113] H. Yee and B. D. Spalding, “Transient stability analysis of multimachine power systems by the method of hyperplanes," *IEEE Trans. Power App. Syst.*, vol. 96, no. 1, pp. 276-284, Jan. 1977.

[114] H. D. Chiang, F. F. Wu and P. P. Varaiya, “Foundations of the potential energy boundary surface method for power system transient stability analysis," *IEEE Trans. Circuits Syst.*, vol. 35, no. 6, pp. 712-728, June 1988.

[115] N. Kakimoto, Y. Ohsawa and M. Hayashi, “Transient stability analysis of electric power system via Lure’ type Lyapunov functions, Part I and II," *Trans. IEE of Japan*, vol. 98, pp. 516, May-June 1978.

[116] M. Ribbens-Pavella and B. Lemal, “Fast determination of stability regions for online transient power-system studies,” *Proc. IEEE*, vol. 123, no. 7, pp. 689-696, July 1976.

[117] M. Oluic, M. Ghandhari and B. Berggren, “On the parametrization of rotor angle transient stability region”, *2015 North American Power Symposium (NAPS)*, Charlotte, 2015, pp. 1-6.

[118] J. Groß, *Linear Regression*. Berlin Heidelberg, Germany: Springer-Verlag, 2003.

[119] A. Bjork, *Numerical Methods for Least Squares Procedure*. Philadelphia, PA: Society for Industrial and Applied Mathematics, 1996.

[120] D. C. Montgomery, E. A. Peck and G. G. Vining, *Introduction to Linear Regression Analysis, 5th Edition*. Hoboken, NJ: Wiley, 2012.

[121] M. Oluic, M. Ghandhari and B. Berggren, “Methodology for rotor angle transient stability assessment in parameter space", *IEEE Trans. Power Syst.*, vol. 32, no. 2, pp. 1202-1211, Mar. 2017.

[122] E. W. Kimbark, *Power System Stability, Volume I: Elements of Stability Calculations*. New York, NY: IEEE Press, 1995.

[123] Y. Wang *et al.*, “Transient stability enhancement and voltage regulation of power systems", *IEEE Trans. Power Syst.*, vol. 8, no. 2, pp. 620-627, May 1993.

[124] Z. Dostal, *Optimal Quadratic Programming Algorithms: With Applications to Variational Inequalities*. New York City, NY: Springer, 2009.

[125] P. E. Gill, W. Murray and M. H. Wright, *Numerical Linear Algebra and Optimization, Vol. 1*. Redwood City, CA: Addison Wesley, 1991.

[126] T. Van Cutsem, “Voltage instability: phenomena, countermeasures, and analysis methods," *Proc. IEEE*, vol. 88, no. 2, pp. 208-227, Feb. 2000.

[127] T. Van Cutsem and R. Mailhot, “Validation of a fast voltage stability analysis method on the Hydro-Quebec system", *IEEE Trans. Power Syst.*, vol. 12, no. 1, pp. 282-292, Feb. 1997.

[128] D. J. Hill, “Nonlinear dynamic load models with recovery for voltage stability studies", *IEEE Trans. Power Syst.*, vol. 8, no. 1, pp. 166-176, Feb. 1993.

[129] J. D. Ainsworth, A. Gavrilovic and H. L. Thanawala, “Static and synchrounous compensators for HVDC transmission convertors connected to weak AC systems," *CIGRE conference*, Paris, 1980, paper 31-01.

[130] B. Franken and G. Andersson, “Analysis of HVDC converters connected to weak AC systems", *IEEE Trans. Power Syst.*, vol. 5, no. 1, pp. 235-242, Feb. 1990.

[131] A. E. Hammad and M. Z. El-Sadek, “Prevention of transient voltage instabilities due to induction motor loads by static VAr compensators", *IEEE Trans. Power Syst.*, vol. 4, no. 3, pp. 1182-1190, Aug. 1989.

[132] C. D. Vournas and G. A. Manos, “Modelling of stalling motors during voltage stability studies", *IEEE Trans. Power Syst.*, vol. 13, no. 3, pp. 775-781, Aug. 1998.

[133] M. S. Calovic, “Modeling and analysis of under-load tap-changing transformer control systems," *IEEE Trans. Power App. Syst.*, vol. PAS-103, no. 7, pp. 1909-1915, July 1984.

[134] H. Ohtsuki, A. Yokoyama and Y. Sekine, “Reverse action of on-load tap changer in association with voltage collapse", *IEEE Trans. Power Syst.*, vol. 6, no. 1, pp. 300-306, Feb. 1991.

[135] C. C. Liu and K. T. Vu, “Analysis of tap-changer dynamics and construction of voltage stability regions," *IEEE Trans. Circuits Syst.*, vol. 36, no. 4, pp. 575-590, Apr. 1989.

[136] K. T. Vu and C. C. Liu, “Shrinking stability regions and voltage collapse in power systems," *IEEE Trans. Circuits Syst. I, Fundam. Theory Appl.*, vol. 39, no. 4, pp. 271-289, Apr. 1992.

[137] IEEE Task Force on Excitation Limiters, “Recommended models for overexcitation limiting devices," *IEEE Trans. Energy Convers.*, vol. 10, no. 4, pp. 706-713, Dec. 1995.

[138] T. J. Overbye, “Effects of load modelling on analysis of power system voltage stability," *Int. J. Elec. Power*, vol. 16, no. 5, pp. 329-338, Oct. 1994.

[139] D. J. Hill and I. M. Y. Mareels, "Stability theory for differential/algebraic systems with application to power systems," *IEEE Trans. Circuits Syst.*, vol. 37, no. 11, pp. 1416-1423, Nov. 1990.

[140] K. L. Praprost and K. A. Loparo, "A stability theory for constrained dynamic systems with applications to electric power systems," *IEEE Trans. Autom. Control*, vol. 41, no. 11, pp. 1605-1617, Nov. 1996.

[141] T. V. Cutsem and C. Vournas, *Voltage Stability of Electric Power Systems*. Norwell, MA: Kluwer Academic Publishers, 1998.

[142] P. Kessel and H. Glavitsch "Estimating the voltage stability of a power system," *IEEE Trans. Power Del.*, vol. 1, no. 3, pp. 346-354, July 1986.

[143] T. J. Overbye, "A power flow measure for unsolvable cases," *IEEE Trans. Power Syst.*, vol. 9, no. 3, pp. 1359-1365, Aug. 1994.

[144] T. J. Overbye, "Computation of a practical method to restore power flow solvability," *IEEE Trans. Power Syst.*, vol. 10, no. 1, pp. 280-287, Feb. 1995.

[145] S. Iwamoto and Y. Tamura, "A load flow calculation method for ill-conditioned power systems," *IEEE Trans. Power App. Syst.*, vol. PAS-100, no. 4, pp. 1736-1743, Apr. 1981.

[146] M. Huneault and F. D. Galiana "A survey of the optimal power flow literature," *IEEE Trans. Power Syst.*, vol. 6, no. 2, pp. 762-770, May 1991.

[147] H. G. Kwatny, A. K. Pasrija and L. Y. Bahar, "Static bifurcations in electric power networks: Loss of steady-state stability and voltage collapse," *IEEE Trans. Circuits Syst.*, vol. 33, no. 10, pp. 981-991, Oct. 1986.

[148] V. A. Venikov *et al.*, "Estimation of electrical power system steady-state stability in load flow calculations," *IEEE Trans. Power App. Syst.*, vol. 94, no. 3, pp. 1034-1041, May 1975.

[149] P. A. Löf, G. Andersson and D. J. Hill, "Voltage stability indices for stressed power systems," *IEEE Trans. Power Syst.*, vol. 8, no. 1, pp. 326-335, Feb. 1993.

[150] C. A. Canizares, A. C. Z. De Souza and V. H. Quintana, "Comparison of performance indices for detection of proximity to voltage collapse," *IEEE Trans. Power Syst.*, vol. 11, no. 3, pp. 1441-1450, Aug. 1996.

[151] F. M. Echavarren *et al.*, “Formulation, computation and improvement of steady state security margins in power systems. Part I: Theoretical framework," *Int. J. Elec. Power*, vol. 33, no. 2, pp. 340-346, Feb. 2011.

[152] F. M. Echavarren *et al.*, “Formulation, computation and improvement of steady state security margins in power systems. Part II: Results," *Int. J. Elec. Power*, vol. 33, no. 2, pp. 347-358, Feb. 2011.

[153] S. Greene, I. Dobson and F. L. Alvarado, “Sensitivity of the loading margin to voltage collapse with respect to arbitrary parameters," *IEEE Trans. Power Syst.*, vol. 12, no. 1, pp. 262-272, Feb. 1997.

[154] C. A. Canizares, “Calculating optimal system parameters to maximize the distance to saddle-node bifurcations," *IEEE Trans. Circuits Syst. I, Fundam. Theory Appl.*, vol. 45, no. 3, pp. 225-237, Mar. 1998.

[155] A. Tiranuchit and R. J. Thomas, “A posturing strategy against voltage instabilities in electric power systems", *IEEE Trans. Power Syst.*, vol. 3, no. 1, pp. 87-93, Feb. 1988.

[156] I. Dobson and L. Lu, “New methods for computing a closest saddle node bifurcation and worst case load power margin for voltage collapse", *IEEE Trans. Power Syst.*, vol. 8, no. 3, pp. 905-913, Aug. 1993.

[157] B. H. Chowdhury and C. W. Taylor, “Voltage stability analysis: V-Q power flow simulation versus dynamic simulation", *IEEE Trans. Power Syst.*, vol. 15, no. 4, pp. 1354-1359, Nov. 2000.

[158] N. Flatabø, R. Ognedal and T. Carlsen, “Voltage stability condition in a power transmission system calculated by sensitivity methods", *IEEE Trans. Power Syst.*, vol. 5, no. 4, pp. 1286-1293, Nov. 1990.

[159] K. Iba *et al.*, “Calculation of critical loading condition with nose curve using homotopy continuation method", *IEEE Trans. Power Syst.*, vol. 6, no. 2, pp. 584-593, May 1991.

[160] H. D. Chiang *et al.*, “CPFLOW: a practical tool for tracing power system steady-state stationary behavior due to load and generation variations", *IEEE Trans. Power Syst.*, vol. 10, no. 2, pp. 623-634, May 1995.

[161] V. Ajjarapu and C. Christy, “The continuation power flow: a tool for steady state voltage stability analysis", *IEEE Trans. Power Syst.*, vol. 7, no. 1, pp. 416-423, Feb. 1992.

[162] C. A. Canizares and F. L. Alvarado, “Point of collapse and continuation methods for large AC/DC systems", *IEEE Trans. Power Syst.*, vol. 8, no. 1, pp. 1-8, Feb. 1993.

[163] T. V. Cutsem, “A method to compute reactive power margins with respect to voltage collapse", *IEEE Trans. Power Syst.*, vol. 6, no. 1, pp. 145-156, Feb. 1991.

[164] O. O. Obadina and G. J. Berg, “Determination of voltage stability limit in multimachine power systems", *IEEE Trans. Power Syst.*, vol. 3, no. 4, pp. 1545-1554, Nov. 1988.

[165] C. J. Parker, I. F. Morrison and D. Sutanto, “Application of an optimisation method for determining the reactive margin from voltage collapse in reactive power planning", *IEEE Trans. Power Syst.*, vol. 11, no. 3, pp. 1473-1481, Aug. 1996.

[166] G. D. Irisarri *et al.*, “Maximum loadability of power systems using interior point nonlinear optimization method", *IEEE Trans. Power Syst.*, vol. 12, no. 1, pp. 162-172, Feb. 1997.

[167] H. D. Chiang *et al.*, “On voltage collapse in electric power systems," *IEEE Trans. Power Syst.*, vol. 5, no. 2, pp. 601-611, May 1990.

[168] E. G. Potamianakis and C. D. Vournas, “Short-term voltage instability: effects on synchronous and induction machines", *IEEE Trans. Power Syst.*, vol. 21, no. 2, pp. 791-798, May 2006.

[169] J. A. Diaz de Leon and C. W. Taylor, “Understanding and solving short term voltage stability problems," in *Proc. IEEE PES Summer Meeting*, Chicago, IL, July 2002, pp. 745-752.

[170] H. Bai and V. Ajjarapu, “A novel online load shedding strategy for mitigating fault-induced delayed voltage recovery," *IEEE Trans. Power Syst.*, vol. 26, no. 1, pp. 294-304, Feb. 2011.

[171] A. Tiwari and V. Ajjarapu, “Optimal allocation of dynamic VAR support using mixed integer dynamic optimization," *IEEE Trans. Power Syst.*, vol. 26, no. 1, pp. 305-314, Feb. 2011.

[172] B. Sapkota and V. Vittal, “Dynamic VAr planning in a large power system using trajectory sensitivities," *IEEE Trans. Power Syst.*, vol. 25, no. 1, pp. 461-469, Feb. 2010.

[173] M. Paramasivam *et al.*, “Dynamic optimization based reactive power planning to mitigate slow voltage recovery and short term voltage instability," *IEEE Trans. Power Syst.*, vol. 28, no. 4, pp. 3865-3873, Nov. 2013.

[174] M. K. Pal, “Voltage stability conditions considering load characteristics," *IEEE Trans. Power Syst.*, vol. 7, no. 1, pp. 243-249, Feb. 1992.

[175] K. L. Praprost and K. A. Loparo, “An energy function method for determining voltage collapse during a power system transient," *IEEE Trans. Circuits Syst. I, Fundam. Theory Appl.*, vol. 41, no. 10, pp. 635-651, Oct. 1994.

[176] M. Oluic *et al.*, “On the nature of voltage impasse regions in power system dynamics studies," *IEEE Trans. Power Syst.*, vol. 33, no. 3, pp. 2660-2670, May 2018.

[177] H. G. Kwatny, R. F. Fischl and C. O. Nwankpa, “Local bifurcation in power systems: theory, computation, and application," *Proc. IEEE*, vol. 83, no. 11, pp. 1456-1483, Nov. 1995.

[178] S. Ayasun, C. O. Nwankpa and H. G. Kwatny, “Computation of singular and singularity induced bifurcation points of differential-algebraic power system model," *IEEE Trans. Circuits Syst. I, Reg. Papers.*, vol. 51, no. 8, pp. 1525-1538, Aug. 2004.

[179] J. W. Nilsson and S. A. Riedel, *Electric Circuits*. Upper Saddle River, NJ: Prentice Hall, 2008.

[180] S. C. Newman, *A Classical Introduction to Galois Theory*. Hoboken, NJ: Wiley, 2012.

[181] D. Hinrichsen and A. J. Pritchard, *Mathematical Systems Theory: Modelling, State Space Analysis, Stability and Robustness*. Berlin-Heidelberg, Germany: Springer-Verlag, 2005.

[182] T. S. Shores, *Applied Linear Algebra and Matrix Analysis*. New York, NY: Springer, 2007.

Curriculum Vitae

Marina Oluić was born in Ruma, Serbia in 1988. She received both B. Sc. (2011) and M. Sc. (2012) degrees in electrical engineering/power systems from Faculty of Technical Sciences (FTN), University of Novi Sad, Serbia. Prior to joining KTH, she was working with small signal stability enhancement using PSSs and Supplementary Wide-Area Controller under supervision of prof. Andrija Sarić.

In September 2012, Marina joined KTH as a PhD candidate of the Erasmus Mundus Joint Doctorate in Sustainable Energy Technologies and Strategies (SETS) programme. This joint PhD programme is run by six institutions in cooperation: Comillas Pontifical University (Spain), Technische Universiteit Delft (The Netherlands), Kungliga Tekniska Högskolan – KTH (Sweden), The Johns Hopkins University (USA), Université Paris Sud XI (France) and Florence School of Regulation (Italy). European Commission's Education, Audiovisual and Culture Executive Agency, EACEA, has supported the funding of this programme. Marina was also awarded an Erasmus Mundus PhD fellowship. Marina's project, "Dynamic Security Region Assessment", has been carried out under prof. Mehrdad Ghandhari's supervision. The co-supervisor in the project was dr. Bertil Berggren, senior principal scientist at ABB Corporate Research. In the period Jan.-Sep. 2016., Marina has also been working as a visiting researcher at "Instituto de Investigación Tecnológica (IIT)", Comillas, Madrid with prof. Luis Rouco as a member of the Modeling, Analysis and Control (MAC) research unit.

Marina's research interests include power system dynamics, stability, and control; FACTS and HVDC systems; and linear and nonlinear control strategies. Beside research, her duties have involved teaching activities related to Power System Analysis and Power System Stability and Control courses at KTH.

List of publications

Papers published in journals with Journal Citation Report (JCR):

[J1] M. Oluic, M. Ghandhari and B. Berggren, “Methodology for rotor angle transient stability assessment in parameter space", *IEEE Trans. Power Syst.*, vol. 32, no. 2, pp. 1202-1211, Mar. 2017.

[J2] M. Oluic, B. Berggren, F. M. Echavarren, M. Ghandhari and L. Rouco, “On the nature of voltage impasse regions in power system dynamics studies”, *IEEE Trans. Power Syst.*, vol. 33, no. 3, pp. 2660-2670, May 2018.

Conference Papers:

[C1] M. Oluic, M. Ghandhari and B. Berggren, “On the parametrization of rotor angle transient stability region”, *2015 North American Power Symposium (NAPS)*, Charlotte, NC, 2015, pp. 1-6.

[C2] M. Oluic, M. Ghandhari and B. Berggren, “Methodology for rotor angle transient stability assessment in parameter space”, *2017 IEEE Power & Energy Society General Meeting*, Chicago, IL, 2017, pp. 1-1.

[C3] M. Oluic, B. Berggren, F. M. Echavarren, M. Ghandhari and L. Rouco, “On the nature of voltage impasse regions in power system dynamics studies”, 2*018 IEEE Power & Energy Society General Meeting*, Portland, OR, 2018, pp. 1-1.

For KTH Royal Institute of Technology:
DOCTORAL THESIS IN ELECTRICAL ENGINEERING
TRITA-EECS-AVL-2019:31
www.kth.se

ISBN 978-91-7873-149-7